

MULTIPLYED SENSITIVITY ENCODING OF MULTI-SHOT  
DIFFUSION-WEIGHTED ECHO PLANAR MRI AT 0.5 TESLA FOR  
CHOLESTEATOMA IMAGING

by

Allyster Klassen

Submitted in partial fulfillment of the requirements  
for the degree of Master of Applied Science

at

Dalhousie University  
Halifax, Nova Scotia  
September 2023

© Copyright by Allyster Klassen, 2023

# Table of Contents

List of Tables .....	v
List of Figures .....	vi
Abstract .....	viii
List of Abbreviations Used .....	ix
Acknowledgements.....	x
1. Introduction and Motivation .....	1
1.1 Cholesteatoma .....	1
1.2 Standard of Care .....	2
1.3 Reassessment imaging.....	3
1.4 Limitations of MRI for Cholesteatoma Reassessment .....	5
1.4.1 Acquisition Sequences .....	5
1.4.2 MRI Field Strength .....	9
1.4.3 Resolution .....	9
1.5 Motivation.....	10
1.6 Hypothesis.....	11
1.7 Objectives.....	11
2. Background .....	13
2.1 MRI Foundations .....	13
2.1.1 T1: Longitudinal Relaxation Time.....	15
2.1.2 T2: Transverse Relaxation Time .....	15
2.2 K-space: Encoding, Sampling, & Reconstruction .....	17
2.2.1 Parallel Imaging.....	19
2.2.2 Sensitivity Encoding (SENSE).....	22
2.3 Diffusion-Weighted Imaging .....	23
2.4 Echo Planar Imaging.....	26
2.5 Multiplexed Sensitivity Encoding (MUSE).....	28
3. Experimental Methods and Pipeline Engineering Design .....	31
3.1 Experimental Methods.....	31
3.1.1 MRI System .....	31
3.1.2 Phantoms .....	33
3.1.3 Human Participants.....	34
3.1.4 Acquisition Parameters.....	34

3.2 Pipeline Engineering and Optimization.....	38
3.2.1 Data Organization .....	38
3.2.2 Sensitivity Maps .....	41
3.2.3 SENSE Estimation of Images.....	53
3.2.4 Phase Error Estimation Due to Motion .....	58
3.2.5 MUSE Correction.....	61
3.3 Data Analysis.....	68
3.3.1 Qualitative Analysis.....	68
3.3.2 Quantitative Analysis .....	68
4. Results and Discussion .....	73
4.1 MUSE Reconstruction .....	73
4.1.1 Phantom Results .....	73
4.1.2 Phantom Discussion .....	75
4.1.3 Healthy Volunteer Results .....	76
4.1.4 Healthy Volunteers Discussion.....	77
4.1.5 Patient and Quality Control Volunteer Results: Qualitative Comparison.....	78
4.1.6 Patient and Quality Control Volunteer Discussion: Qualitative Comparison .....	82
4.1.7 Patient and Quality Control Volunteer Results: GSR .....	83
4.2 Application of ms-DW-EPI at 0.5 T for cholesteatoma imaging.....	86
4.2.1 Distortion Characterization.....	87
4.2.2 Distortion at 0.5T: Results.....	88
4.2.2 Distortion at 0.5T: Discussion .....	89
4.2.3 Distortion at 0.5 T and 3 T: Results .....	90
4.2.4 Distortion at 0.5 T and 3 T: Discussion.....	92
4.2.5 Optimizing b-value and TE for cholesteatoma contrast: Results.....	92
4.2.4 Discussion: Optimizing b-value and TE for cholesteatoma contrast .....	95
5. Conclusions and Future Directions .....	96
References .....	100
Appendix A: Data Transfer.....	110
Appendix II: Additional Images .....	111
Appendix C: MUSE Matlab Code.....	112
Appendix IV: Trends in combined averages.....	120
Appendix V. Switch Frequency Troubleshooting .....	123

Appendix VI. FOV Shift Troubleshooting.....	125
Appendix VII. Acquisition Parameters .....	127
Appendix VIII: Characterizing Coil Coefficients.....	130

## List of Tables

<b>Table 4.1.</b> Paired t-test analysis of ghost-to-signal (GSR) datasets across number of shots and reconstruction methods. ....	84
------------------------------------------------------------------------------------------------------------------------------------	----

## List of Figures

<b>Figure 1.1.</b> High resolution CT scan of auditory canal in a patient with diagnosed cholesteatoma. ....	4
<b>Figure 1.2.</b> Hyperintense signal produced by cholesteatoma and distortion-induced signal pile-up. ....	4
<b>Figure 2.1.</b> The net magnetization vector recovers through T1 and T2 relaxation after an RF pulse. ....	14
<b>Figure 2.2.</b> T2 relaxation describes the reduction in net transverse magnetization due to loss of phase coherence. ....	16
<b>Figure 2.3.</b> The frequency and image space domains are related by the FFT. ....	17
<b>Figure 2.4.</b> Sensitivity maps from a 16-channel array coil. ....	19
<b>Figure 2.5.</b> Schematic of DW pulse sequence. ....	24
<b>Figure 2.6.</b> Schematic of EPI pulse sequence. ....	26
<b>Figure 2.7.</b> Single-shot EPI acquisition. ....	26
<b>Figure 2.8.</b> Signal pile-up due to distortion and motion artifact (ghost) levels change with number of EPI shots. ....	27
<b>Figure 2.9.</b> Schematic of multishot EPI. ....	28
<b>Figure 3.1.</b> Synaptive 0.5 T MRI. ....	32
<b>Figure 3.2.</b> Comparison of coil images across anatomical position and in an ACR phantom. ....	33
<b>Figure 3.3.</b> MRI phantoms were used for quality control imaging. ....	33
<b>Figure 3.4.</b> Optimizing spatial resolution. ....	36
<b>Figure 3.5.</b> Early versions of the offline reconstruction revealed acquisition specificity of the pipeline. ....	39
<b>Figure 3.6.</b> Example of FOV shift. ....	40
<b>Figure 3.7.</b> Visible differences between images from physician data server and MUSE reconstruction. ....	41
<b>Figure 3.8.</b> Comparing image reconstruction with variations of coil sensitivities. ....	43
<b>Figure 3.9.</b> Channel combination coefficient breadcrumbs across diffusion directions. ....	44
<b>Figure 3.10.</b> FOV difference between coil coefficient breadcrumbs and derived sensitivities. ....	46
<b>Figure 3.11.</b> Comparison of 1-shot derived and 2-shot derived sensitivities. ....	47
<b>Figure 3.12.</b> Output images from the MUSE pipeline using 1-shot derived and pseudo 1-shot derived sensitivities. ....	48
<b>Figure 3.13.</b> Investigating optimal threshold and kernel size combinations for sensitivity masking. ....	50
<b>Figure 3.14.</b> Denoising considerations for derived sensitivities. ....	51
<b>Figure 3.15.</b> Noise decorrelation matrix trials to address excess background noise. ....	52
<b>Figure 3.16.</b> K-space representation of 4 individual shots from a 4-shot acquisition. ....	54
<b>Figure 3.17.</b> Image space of each shot from a 4-shot acquisition. ....	55
<b>Figure 3.18.</b> Estimated full FOV image for each shot from a 4-shot acquisition after SENSE reconstruction. ....	55
<b>Figure 3.19.</b> Image quality comparison when averaging before or after the MUSE step. ....	56
<b>Figure 3.20.</b> Comparing averages from a three average acquisition in the z-diffusion direction. ....	57
<b>Figure 3.21.</b> Comparing individual averages in a single slice for a single diffusion direction for quality. ....	57

<b>Figure 3.22.</b> Comparison of individual and combined averages. ....	58
<b>Figure 3.23.</b> Individual averages from a six average acquisition after implementing a modified reconstruction pipeline. ....	58
<b>Figure 3.24.</b> Phase maps for a 4-shot acquisition on a phantom in two slices. ....	60
<b>Figure 3.25.</b> Sensitivity maps corrected for motion with the phase maps. ....	60
<b>Figure 3.26.</b> Modelled k-space phase trajectory shifts for a 4-shot acquisition. ....	63
<b>Figure 3.27.</b> Comparing MUSE on to MUSE off images for ghosting and image quality. ....	64
<b>Figure 3.28.</b> Identifying the source of the MUSE reconstruction issue using a generated phantom model. ....	66
<b>Figure 3.29.</b> ADC maps reconstructed with MUSE and from the vendor reconstruction. ....	67
<b>Figure 3.30.</b> Circular cropping in the vendor reconstruction for participant MUSE_005 hindered accurate ghosting detection. ....	69
<b>Figure 3.31.</b> Representative example of ROIs drawn on a participant dataset with known pathology. ....	70
<b>Figure 3.32.</b> Representative example of ROIs drawn on a healthy volunteer dataset. ....	71
<b>Figure 4.1.</b> Examples of the phantom data being used to find issues with the phase correction. ....	73
<b>Figure 4.2.</b> Phantom data used to develop the MUSE pipeline. ....	73
<b>Figure 4.3.</b> Quality control images produced with the current 3-shot 96x96 protocol with and without MUSE. ....	74
<b>Figure 4.4.</b> Phantom images reconstructed with and without MUSE across diffusion directions. ....	74
<b>Figure 4.5.</b> Proof of concept of reduced ghosting with MUSE. ....	76
<b>Figure 4.6.</b> Four repetitions of consecutive, identical 4-shot acquisition in a single patient. ....	77
<b>Figure 4.7.</b> Volunteer MUSE_005 with a diagnosed cholesteatoma. ....	79
<b>Figure 4.8.</b> Patient diagnosed with a large cholesteatoma (MUSE_006). ....	80
<b>Figure 4.9.</b> Patient with a suspected cholesteatoma and a suspicious fluid mass across acquisitions (MUSE_007). ....	80
<b>Figure 4.10.</b> Healthy volunteer (MUSE_008) acquired with the cholesteatoma protocol. ....	81
<b>Figure 4.11.</b> Healthy volunteer MUSE_009 across acquisition methods. ....	81
<b>Figure 4.12.</b> Box and whisker plot comparing mean GSR across number of shots with and without MUSE. ....	83
<b>Figure 4.13.</b> Examples of distortion. ....	87
<b>Figure 4.14.</b> Misplaced interfering signal removed with MUSE. ....	87
<b>Figure 4.15.</b> Box-and-whisker plot of DSR across number of shots with and without MUSE reconstruction. ....	88
<b>Figure 4.16.</b> Box and whisker plot of paired t-test analysis comparing means between acquisition and reconstruction methods. ....	89
<b>Figure 4.17.</b> Protocolling decisions impact pathology contrast. ....	94

## Abstract

Cholesteatoma is an abnormal skin mass in the middle ear requiring surgical excision, and accurate post-surgical imaging is of interest to avoid repeat surgeries. MRI suffers from susceptibility-induced field gradients at air-bone interfaces in the auditory canal, resulting in geometric distortion and signal pile-up. Multi-shot diffusion-weighted echo-planar imaging (ms-DW-EPI) at 0.5 T may reduce distortion, but requires motion correction. Multiplexed sensitivity encoding (MUSE) estimates intra-shot phase errors from motion, but requires sufficient signal to perform the correction. It is unknown whether ms-DW-EPI at 0.5 T provides sufficient signal to perform MUSE. In this work, a MUSE reconstruction pipeline was designed and optimized. The engineering design process leading to an optimized system for reconstructing patient images is discussed. The resulting images demonstrated qualitatively reduced motion artifact compared to images reconstructed without MUSE and was statistically supported, confirming the hypothesis. This supported further exploration into imaging cholesteatoma with ms-DW-EPI at 0.5 T.



## List of Abbreviations Used

CT	Computed Tomography
DSR	Distortion-to-signal ratio
DWI	Diffusion Weighted Imaging
EPI	Echo Planar Imaging
ETL	Echo Train Length
FOV	Field of View
GNR	Ghost-to-noise ratio
GRAPPA	GeneRalized Autocalibrating Partially Parallel Acquisitions
GSR	Ghost-to-signal ratio
HASTE	Half-Fourier-Acquisition Single-shot Turbo-spin-Echo
MRI	Magnetic Resonance Imaging
ms-EPI	Multi-shot Echo Planar Imaging
MUSE	Multiplexed Sensitivity Encoding
OCT	Optical Coherence Tomography
PROPELLER	Periodically Rotated Overlapping Parallel Lines with Enhanced Reconstruction
PDR	Pathology-to-distortion ratio
PSR	Pathology-to-signal ratio
SENSE	Sensitivity Encoding
SIFG	Susceptibility-induced Field Gradients
SMASH	Simultaneous Acquisition of Spatial Harmonics
SNR	Signal-to-noise ratio
ss-EPI	Single-shot Echo Planar Imaging
T	Tesla
TE	Echo time
TR	Repetition time

## Acknowledgements

First, I would like to express my sincere gratitude to my co-supervisors Dr. Steven Beyea and Dr. James Rioux, and to Dr. Chris Bowen for your guidance and support throughout my masters program. This thesis would not have been half of what it is if it wasn't for you.

This project was made possible by the contributions and collaborations of MANY. Thank you to all of you. To my committee members and defence committee. To my funding sources. To the ENT physicians and neuroradiologists. To the Synaptive Medical researchers. To the BME department. To the BIOTIC team, MR technicians, and the study participants. To my labmates and BME peers. Thank you all.

Lastly, thank you to Keric , Andrea, Kat, Anya, and the rest of my family for your unconditional support, feigned nods of understanding and genuine excitement in all my scientific endeavours.

# 1. Introduction and Motivation

## 1.1 Cholesteatoma

Cholesteatoma is a skin mass or lesion known colloquially as ‘skin in the wrong place’<sup>1</sup>. The pearl-like cyst develops from the eardrum, or tympanic membrane, and proliferates into the middle ear space. It occurs in approximately 9 in 100,000 people<sup>2</sup>, is most common in the adult male population<sup>3</sup>, and is dominant in Caucasian individuals<sup>4</sup>.

Cholesteatoma is predominantly acquired rather than congenital<sup>2</sup>, and while several theories of pathogenic origins exist, the most widely accepted cause is pressure imbalance across the tympanic membrane<sup>4</sup>. The middle ear is secluded from the external environment by the tympanic membrane. In a healthy individual, pressure balance between the internal and external environments is maintained via the eustachian tube. In the event of chronic ear infection, eustachian tube function may be impaired. As a result, the pressure in the middle ear drops and creates a negative internal pressure that draws the tympanic membrane in. This invagination coalesces in a cholesteatoma mass which can further engulf inflammatory cells, granulation tissue, bacteria, elastin, collagenous fibers, and bone fragments due to erosion<sup>4</sup>.

This pathogenic theory is supported by the histologic composition. Cholesteatoma is primarily composed of keratinized stratified squamous epithelium<sup>4</sup>, a skin tissue type that lines the external auditory canal and forms a thin layer over the external face of the tympanic membrane but is not found in the middle ear<sup>5</sup>. The etymology of the pathology suggests a cancerous nature, and standalone studies have shown neoplastic tendencies<sup>6</sup> and progression into squamous cell carcinoma<sup>7</sup>. However,

literature overwhelmingly suggests that this is a historical misnomer and the pathology is non-cancerous<sup>4</sup>.

Cholesteatoma symptoms reflect the progression from chronic ear infection. Primary symptoms are vertigo, fever, and otalgia<sup>8</sup>, and can be accompanied by tympanic membrane perforation, abnormal and pungent fluid leakage, clogging of the ear canal<sup>8</sup>, balance disturbance, and conductive hearing loss<sup>9</sup>. Symptoms worsen the longer the pathology is left untreated. Late-stage symptoms can escalate to intracranial abscesses, purulent labyrinthitis, and facial paralysis<sup>8</sup>. Symptoms can be managed with antibiotics, but ultimately the only course of treatment is surgical removal.

## 1.2 Standard of Care

The standard of care for cholesteatoma treatment following an initial diagnosis is that the patient undergoes a computed tomography (CT) scan to confirm the diagnosis<sup>8,10</sup>. CT is the standard for pre-surgical cholesteatoma imaging because it is sensitive to detecting occlusion in the auditory space and erosion of the surrounding bone and ossicular chain<sup>4,11</sup>. In this case, sensitivity refers to CT having sufficient resolution and contrast for detecting pathology. The initial CT scan may be accompanied by a magnetic resonance imaging (MRI) scan. MRI complements CT with soft tissue contrast<sup>11</sup>.

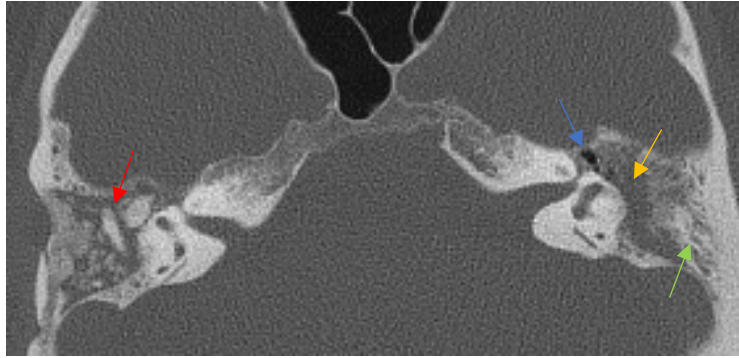
The surgery to remove cholesteatoma ranges from minimally invasive to extensive reconstruction. The surgery may require mastoidectomy that damages the integrity of the bony partitions in 'canal wall up' or 'canal wall down' procedures, or tympanoplasty to restructure the eardrum<sup>12</sup>. Changes in the auditory environment as a result of the

surgery depend on the extensiveness of the surgery, but may include bone restructuring, filling with a surgical reconstruction material and the development of scar granulation tissue.

Cholesteatoma is a persistent and recurrent pathology<sup>13</sup>, meaning that if it is not fully removed the first time around, or conditions persist, it will return. This may occur from missing a small section of pathology during surgery or a new forming mass<sup>12</sup>. Recurrence occurs in approximately 15% of adult cases<sup>12,13</sup>, though higher recurrence rates have been reported<sup>14</sup>. For this reason, patients are called back for a follow-up appointment anywhere between six months<sup>8,15</sup> to several years<sup>16</sup> post-surgery for reassessment.

### 1.3 Reassessment imaging

CT is sensitive for exposing new occlusions in the auditory canal and changes in the surrounding bone, but lacks the specificity to differentiate between granulation tissue, fluid, fibrous scar tissue, reconstruction materials used during the initial surgery<sup>4,17</sup>, and herniated brain tissue<sup>18</sup>(Figure 1.1). Here, specificity refers to the ability to differentiate between tissue types. The sensitivity and specificity of CT for identifying recurrent cholesteatoma are 43% and 48% respectively<sup>11</sup>. For this reason, CT cannot be used to assess for the recurrence of cholesteatoma after surgery. Optical coherence tomography (OCT) provides the necessary specificity, but current technology has limited



**Figure 1.1.** High resolution CT scan of auditory canal in a patient with diagnosed cholesteatoma. The image right side shows a new presenting cholesteatoma (orange arrow) obstructing the auditory canal (blue arrow) and eroding the mastoid bone (green arrow). The patient had undergone previous surgery for contralateral cholesteatoma on the image left side. Bone fragments are identified as white structures (red arrow), but it is unclear whether the surrounding gray tissue is recurrent pathology, scar tissue, or surgical construction material.

resolution and flexibility, particularly without damaging the tympanic membrane or ossicles<sup>19</sup>.

Post-surgical reassessment of cholesteatoma with diffusion weighted (DW) MRI demonstrates a hyperintense pathology compared to surrounding tissue<sup>18,20</sup>. This is thought to occur through a combination of diffusion restriction and T2 shine-through, a hyperintensity from a T2-weighting effect<sup>4,15,17,21</sup>. The dual effect is a result of the keratin having a lengthened T2 compared to other tissue as well as restricted diffusion from the cell mass<sup>11</sup>. From a cost standpoint, the difference between performing a second-look surgery compared to an MRI scan is estimated between \$180.27 and



**Figure 1.2.** Hyperintense signal produced by cholesteatoma and distortion-induced signal pile-up. Cholesteatoma appears slightly hyperintense (blue arrow) compared to cortical tissue. Distortion manifests as hyperintense signal along auditory canal (orange arrow) in a similar anatomical position to the contralateral pathology. Patient was scanned with DW-MRI at 3 Tesla.

\$390.66<sup>22</sup>. However, distortion-induced signal pile-up at air-bone interfaces manifest as hyperintense clusters (Figure 1.2). The similar appearance of the pathology and distortion on DW-MRI images result in false positive diagnoses which reduce physician confidence<sup>15</sup>.

Due to these imaging limitations, the current standard of care for suspicion of recurrent cholesteatoma is a second-look surgery<sup>17,23-25</sup>. One review reported that, on average, 67% of second-look surgeries across multiple studies do not find recurrent pathology<sup>16</sup>. In the event of not finding recurrence, patients are unnecessarily exposed to the associated surgical risks of anaesthesia<sup>26</sup>, balance loss, impairments to hearing and taste, facial nerve paralysis and infection<sup>18</sup>. However, untreated recurrent pathology can progress into the detrimental symptoms of nerve damage and bone erosion mentioned earlier, necessitating a second-look surgery in the absence of reliable reassessment imaging. One recommendation is to perform a second-look surgery only in the case where there is suspicion that a portion of the original pathology was not removed<sup>16</sup>. This may reduce the overall number of surgeries performed, but does not resolve the ambiguity for diagnosing a residual cholesteatoma outside of surgery.

#### 1.4 Limitations of MRI for Cholesteatoma Reassessment

The distortion in MRI images is a multifactor result of susceptibility-induced field gradients causing signal misplacement. Adjustments can be made to the acquisition in order to mitigate distortion.

##### 1.4.1 Acquisition Sequences

MRI acquisition sequences are chosen based on the desired contrast with the feature of interest. For recurrent cholesteatoma, the pathological mass needs to be

differentiated from cortical tissue and distortion. Tissue contrast can be introduced to MR images beyond relaxation properties. This is done on the basis of sensitizing the signal to physical properties of different tissues such as their spin lattice relaxation time (T1), spin-spin relaxation time (T2), and molecular apparent self-diffusion coefficient (ADC). T1- and T2-weighted acquisitions prior to second-look surgery report low true positive and radiosurgical correlation rates of 37% and 70% respectively<sup>27</sup>, and so do not fulfill the contrast requirements. Contrast encoding with DW-MRI has been reported with sensitivity and specificity of up to 92.2% and 91.7%, respectively<sup>28</sup>, making it a suitable candidate.

In MRI, the Fourier components of the image in data-space are commonly referred to collectively as k-space, which is subsequently transformed with the Fourier transform (FT). Differences in pulse sequences, such as EPI and PROPELLER, differ in how the k-space data is acquired, which ultimately influences the images upon FT.

#### *1.4.1.1 Non-EPI Sequences*

A rapid imaging sequence is required to acquire diffusion signal. These can be broken into echo planar imaging (EPI) and non-EPI sequences. EPI is criticized for distortion manifesting as signal pile-up in the auditory canal that confounds cholesteatoma diagnosis. Non-EPI acquisitions attempt to address this shortcoming. The two leading non-EPI sequences for cholesteatoma reassessment are PROPELLER and HASTE. Periodically rotated overlapping parallel lines with enhanced reconstruction (PROPELLER) collects alternating lines of k-space data centered across the middle of k-space<sup>23</sup>. The advantages of this technique is that the repeated collection of the center of k-space makes the acquisition motion robust. However, the acquisition sequence is not



available on all systems, is limited to detecting cholesteatomas between 3<sup>29</sup> to 5mm, has lengthy acquisition times<sup>4</sup>, and in some cases has reported to present persistent susceptibility distortion<sup>24</sup>. Half-Fourier-acquisition single-shot turbo-spin-echo (HASTE) pairs high in-plane resolution with a refocusing pulse following each echo to reduce susceptibility distortion<sup>30</sup>. HASTE has demonstrated utility in cholesteatoma reassessment<sup>11,31</sup>. However, as with PROPELLER, HASTE is a specialized sequence not available on all systems, and is known to lack sensitivity to small cholesteatomas 2-3 mm in size<sup>30</sup>.

#### *1.4.1.2 EPI Sequences*

An alternative to designing specialized non-EPI sequences is to address the issue of distortion in EPI. EPI is a rapid imaging technique that collects an entire k-space in a single repetition time (TR). In single-shot EPI (ss-EPI), lengthy acquisition times lead to phase error accumulation and distortion, and so is not ideal for reassessment imaging<sup>4</sup>. Alternatively, the acquisition can be broken into multiple passes over k-space, or multi-shot EPI (ms-EPI). This acquisition collects every nth line of k-space, where n is the number of shots. This reduces the length of the temporal acquisition window for each shot to reduce the accumulation of phase errors leading to distortion.

#### *1.4.1.3 Motion Correction*

A limitation of ms-DW-EPI is that the strong applied diffusion gradients rely on accurate and reliable location of produced signal, which is corrupted with intra-shot motion. Patient motion may arise from large-scale twitching or fidgeting, but also from bodily functions such as respiration or swallowing. Even on this millimeter scale, motion between shots produces faint repetitions of the original anatomy every 1/n field of view

(FOV). One way to reduce motion artifact is to collect the data even faster, thereby minimizing the window of opportunity for intra-shot motion to occur. Feinberg et. al. proposed a custom pulse sequence for simultaneous acquisition of temporal and spatial data, which saw a 2- to 4-fold decrease in the temporal acquisition window length<sup>32</sup>. However, this technique required a pulse sequence modification, reported reduced SNR and increased distortion in regions of high susceptibility, and reported concerns of persistent aliasing from parallel imaging.

Alternatively, intra-shot patient motion can be corrected during image reconstruction. Multiplexed sensitivity encoding (MUSE) is a motion correction technique that estimates and incorporates intra-shot phase errors in the image reconstruction to remove the motion artifact<sup>33</sup>. This technique has been applied to DW-EPI images with diffusion gradient b-values up to 2000 s/mm<sup>2</sup> at 3 Tesla (T). This was used to support the argument that MUSE i) does not have an signal-to-noise ratio (SNR) penalty on the produced images and ii) is not limited by the SNR of images to be reconstructed. This was used for demonstration purposes. However, cholesteatoma contrast is sufficient at a b-value of 800-1000 s/mm<sup>2</sup><sup>20</sup>, and so b-values up to 2000 s/mm<sup>2</sup>, and the corresponding SNR reduction, is unnecessary.

DWI with MUSE reconstruction has been implemented clinically in breast tumor<sup>34-36</sup>, rectal<sup>37</sup>, Crohn's disease inflammation<sup>38</sup>, head and neck cancer<sup>39</sup>, functional MRI<sup>40</sup>, free-breathing abdominal<sup>41</sup>, brain aging changes<sup>42</sup>, endometrial cancer<sup>43</sup>, pancreas<sup>44</sup>, stroke<sup>45</sup>, and prostate cancer<sup>46</sup> imaging. All of these applications were implemented at clinical field strengths of 1.5 or 3 T.

#### 1.4.2 MRI Field Strength

The clinical standard for MRI field strength is in the range of 1.5-3 T<sup>47</sup>. The amount of produced signal, often described by SNR, scales approximately proportionally to applied magnetic field strength<sup>48</sup>. For example, an image collected at 3 T would produce about 6 times the amount of signal produced at 0.5 T. This reduced signal production is a known limitation of low-field imaging that occurs at field strengths between 64 mT to 1 T<sup>47</sup>. However, produced signal is only half of the SNR ratio. Dielectric resistance, a product of dielectric effects and the primary noise contributor at higher field strengths, is reduced at low field strengths<sup>47</sup>. The reduced dielectric effects and technical advancements for device manufacturing to reduce noise have contributed to an improved SNR overall at low field.

An application where clinical MRI field strengths struggle is in regions of air-bone interfaces, where susceptibility-induced field gradients (SIFG) cause distortion. Susceptibility effects scale with field strength<sup>47</sup>. At lower fields, distortion resulting from SIFG is reduced compared to clinical fields<sup>49</sup>. This is an important advantage in anatomical areas where susceptibility distortion is a concern, such as in the middle ear.

#### 1.4.3 Resolution

Resolution depends on voxel size, a 3-dimensional pixel described by the matrix size, slice thickness, and FOV. The smaller the voxel, the better the resolution. However, the smaller the voxel, the less produced signal, since there is less substance in that area to produce a signal. As described previously, detecting recurrent or residual cholesteatoma is particularly challenging with small cholesteatomas between 2-3mm. In

order to have clinically useful images to detect these small pathologies, thin slices are needed. The challenge is that this correlates with a small voxel and reduced signal production from that voxel.

### 1.5 Motivation

As an imaging modality, CT is restricted to density imaging. This is ideal for identifying an occlusion of the auditory canal in a first-time presenting pathology, but not for differentiating between pathological and scar tissue. DW-MRI demonstrates differentiation of cholesteatoma tissue but is confounded by distortion in the auditory canal. Distortion scales with field strength and acquisition window length, and so could benefit from ms-DW-EPI at 0.5 T.

At a field strength of 0.5 T, the baseline of produced signal would be approximately  $1/6^{\text{th}}$  of that at 3 T, a typical clinical field strength. With the application of a diffusion gradient, the amount of produced signal would be further reduced. Clinically relevant resolution requires a small voxel size with reduced signal production. The claim of the MUSE paper is that even at high b-values, MUSE is not restricted by SNR<sup>33</sup>. This is supported by the clinical applications described here. However, these studies were performed at clinical field strengths between 1.5 to 3 T. Even if the MUSE algorithm itself is not hindered by SNR, an intermediate preparatory step required to calculate the phase errors is known to reduce image SNR. It is unknown whether clinically relevant ms-DW-EPI images at 0.5 T would have sufficient SNR for MUSE reconstruction.

This thesis presents an investigation into the SNR limits of MUSE with ms-DW-EPI at 0.5 T. The following hypothesis addresses this research question.

## 1.6 Hypothesis

*Sufficient SNR will be provided by ms-DW-EPI acquired at 0.5T to perform MUSE and there will be a quantifiable reduction in motion-induced ghosting compared to images reconstructed without MUSE correction.*

MUSE is not a standard reconstruction option on all MRI systems. To investigate this hypothesis, a reconstruction pipeline needed to be developed offline that could handle data acquired at 0.5 T. The following objectives address the thesis workflow to investigate this hypothesis.

## 1.7 Objectives

*Objective 1: Obtain k-space data collected with ms-DW-EPI at 0.5 T. Data must meet the following requirements: i) be available on a local server outside of vendor reconstruction restraints; ii) organized in a cartesian grid with individual shots, channels, diffusion directions, and averages stored separately.*

*Objective 2: Develop an offline reconstruction pipeline using the logic of the established MUSE technique. The pipeline must i) take ms-DW-EPI data as input and ii) output images of acceptable clinical quality. The pipeline should match the vendor reconstruction as closely as possible in order to mitigate any differences in output images to the MUSE reconstruction.*

*Objective 3: Optimize the acquisition and reconstruction for the clinical application of cholesteatoma. The acquisition should match literature standards of resolution as closely*

*as reasonable for clinical relevance. The reconstruction should minimize noise accumulated in the images along the reconstruction pipeline.*

*Objective 4: Evaluate overall image quality and motion artifact levels. Qualitative comparisons between vendor and MUSE reconstructed images should examine overall image appearance and subjective comparisons of artifacts. Quantitative evaluations measure the ghost-to-signal ratio (GSR), distortion-to-signal ratio (DSR), pathology-to-signal ratio (PSR), and pathology-to-distortion ratio (PDR).*

## 2. Background

MRI is a non-invasive imaging technique that uses the principle that a spinning charged particle produces a magnetic field and induces a current. This current is received and interpreted as an MRI signal.

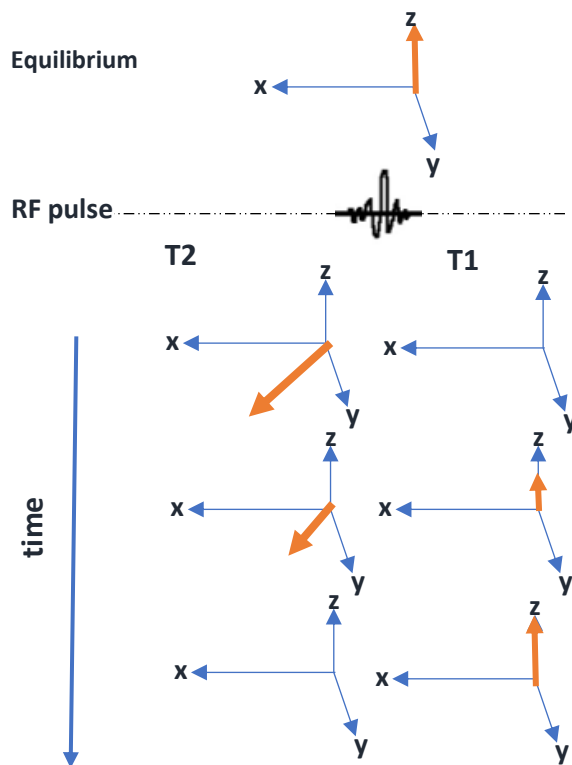
### 2.1 MRI Foundations

An atomic nucleus contains positively-charged spinning protons, known colloquially as 'spins'<sup>50</sup>. Opposing spins will pair together such that the equal and opposite contribution of each spin field cancels out and no net magnetization arises. If, however, a nucleus possesses an odd number of protons, there will be an unpaired spin. In a bulk volume, such as anatomical region of interest, the magnetic field contribution of each individual spin contributes to a net magnetization vector.

In MRI, the global environment of protons in a given volume is influenced by the application of an external electromagnetic field,  $B_o$ . At equilibrium under  $B_o$ , the net magnetization vector in a volume aligns along the z-axis in the direction of  $B_o$ . An applied radio frequency (RF) pulse perturbs the equilibrium to induce the net magnetization vector into the transverse x-y plane. The angle at which spins are flipped into the transverse plane, or the flip angle, can be adjusted. For maximum transverse magnetization, a 90° flip angle is used, and referred to as a 90° RF pulse. Directly following an RF pulse, net magnetization  $M_z$  in the z-axis is zero, and net magnetization in the x-y plane  $M_{xy}$  is at a maximum. In order to excite a particle, the resonant frequency must be matched, as described by

$$\omega = \gamma * B_o$$

where  $\omega$  is the angular frequency of the particle and  $\gamma$  is the gyromagnetic ratio (42.6 MHz/T for hydrogen). Hydrogen is a common choice for MR due to its abundance in the human body<sup>50</sup>. The net magnetization vector returns to equilibrium realignment through a process called relaxation. Relaxation occurs by independent processes in the longitudinal and transverse planes described by T1 and T2 (Figure 2.1).



**Figure 2.1.** The net magnetization vector recovers through T1 and T2 relaxation after an RF pulse. Prior to the RF pulse, the net magnetization is aligned with the applied  $B_0$ . When the RF pulse is applied, net magnetization is pushed into the transverse (x-y) plane. The transverse magnetization decays to zero through loss of phase coherence by T2. At the same time, longitudinal magnetization in the z plane recovers by T1. T1 and T2 are independent and simultaneous processes that are dependent on both the tissue and  $B_0$ .



### 2.1.1 T1: Longitudinal Relaxation Time

T1 relaxation is the rate constant that describes the net longitudinal magnetization,  $M_z$ , recovery along the direction of  $B_0$ <sup>51</sup>. T1 relaxation is described by

$$M_z(t) = M_o(1 - e^{-\frac{t}{T_1}})$$

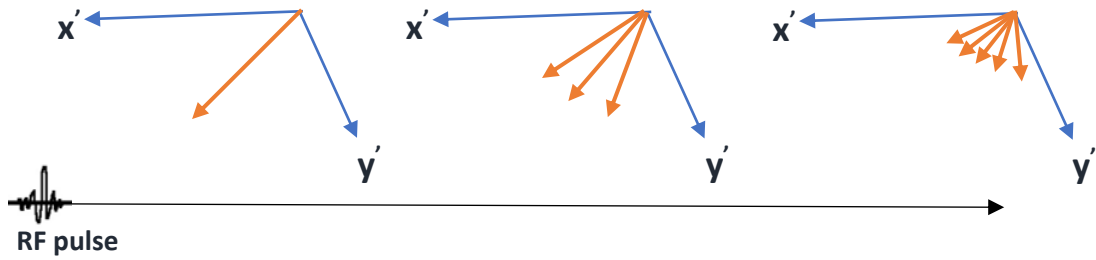
where  $M_o$  is the magnetization prior to the RF pulse,  $t$  is the elapsed time, and T1 is the rate constant of recovery. T1 is typically described by an exponential recovery curve, which is unique to a tissue and is dependent on field strength.

### 2.1.2 T2: Transverse Relaxation Time

T2 relaxation is the rate constant that describes the net transverse magnetization,  $M_{xy}$ , decay along the direction of  $B_0$ <sup>51</sup>. T2 relaxation is described by

$$M_{xy}(t) = M_o * e^{-\frac{t}{T_2}}$$

where  $M_{xy}$  is magnetization in the transverse plane and T2 is the rate constant of transverse magnetization loss. T2 is typically described by a decay curve which, like T1, is unique to a tissue and is dependent on field strength. T2 relaxation is a two-fold process of dephasing which occurs through spin-spin interactions as well as external field inhomogeneities. After the RF pulse, neighbouring spins in the transverse plane are in phase with one another (Figure 2.2). The magnetization vectors from each spin align to produce a net magnetization vector that sum to a maximum signal in the transverse plane. Shortly after, individual spins lose phase coherence, reducing the net magnetization vector. Dephasing continues until phase coherence is lost and no net magnetization remains in the transverse plane.



**Figure 2.2.** *T2 relaxation describes the reduction in net transverse magnetization due to loss of phase coherence. Shown here in a rotating frame of reference, net magnetization is pushed into the transverse (x-y) plane after an RF pulse. Initially, neighbouring spins are in phase. Over time, spin-spin interactions and external inhomogeneities cause dephasing, which leads to a net reduction in transverse signal.*

Dephasing is enhanced by a tissue-independent rate constant called  $T_2^*$ .  $T_2^*$  reflects the homogeneity of  $B_0$ . If a magnetic field is largely homogeneous,  $T_2^*$  and  $T_2$  will be similar. If inhomogeneities exist, dephasing will increase as described by

$$M_{xy}(t) = M_0 * e^{-\frac{t}{T_2^*}}$$

for a rotating frame of reference with a  $90^\circ$  RF pulse. Field inhomogeneities can exist as susceptibility-induced field gradients (SIFG) at tissue boundaries with large inherent susceptibility differences. At higher field strengths, the differences in tissue susceptibilities,  $\Delta B$ , are greater and related to  $T_2^*$  by

$$\frac{1}{T_2^*} = \frac{1}{T_2} + \gamma \Delta B$$

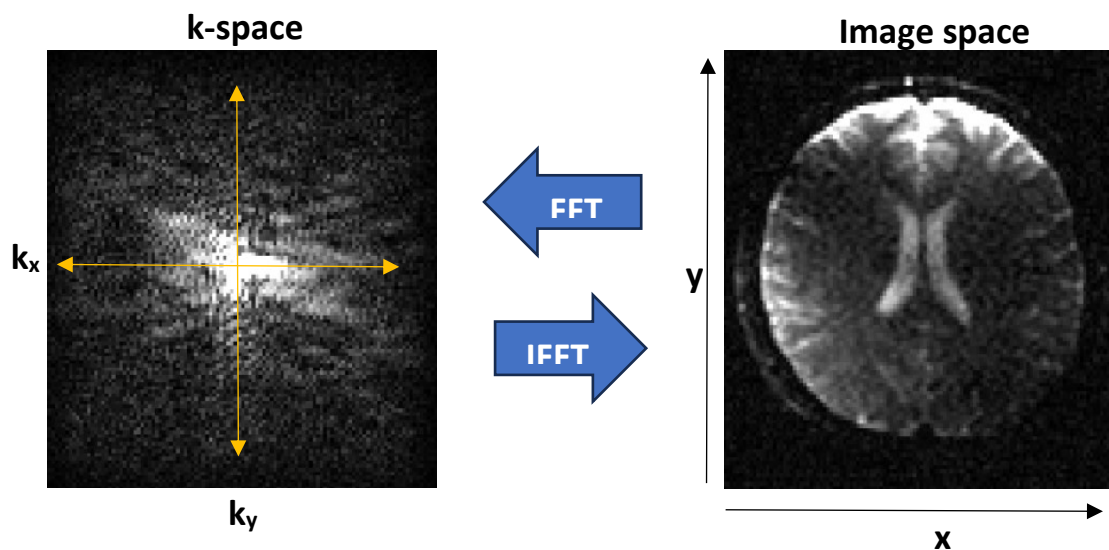
At lower field strengths,  $T_2^*$  increases due to reduced dephasing because of improved field homogeneity.

## 2.2 K-space: Encoding, Sampling, & Reconstruction

MRI image sets are acquired with a series of acquisition scans, collectively called an acquisition protocol. A pulse sequence describes the tissue contrast, signal encoding, and signal readout for a given acquisition sequence or scan.

The MRI signal can be sensitized to a particular contrast weighting with a series of protocolling decisions. The repetition time (TR) is the time between RF pulses<sup>52</sup>. Increasing the TR allows for more opportunity for T1 recovery, and thus less T1 weighting or contribution to the contrast between tissue types. The echo delay time (TE) is the amount of time between the RF pulse and signal readout. A short TE reduces T2 and T2\* effects, since there is less opportunity for dephasing to occur.

The frequency array produced in response to the applied magnetic fields is called k-space<sup>53</sup>. Frequency components represent contributions from the slice or z dimension,



**Figure 2.3.** The frequency and image space domains are related by the FFT. K-space is densely populated around the origin, where low frequencies correspond to the fundamental appearance of the image. Higher frequencies on the outer limits of k-space correspond to fine detail in the image. The FFT transforms the image domain into the frequency domain. The IFFT transforms the frequency domain into the image domain. FFT = Fast Fourier Transform; IFFT = inverse FFT;  $k_y$  = frequencies in y-dimension;  $k_x$  = frequencies in x-dimension;  $y$  = y-dimension;  $x$  = x-dimension.

frequency or y dimension, and the phase or x dimension. For simplicity, the x and y dimensions are often depicted alone on a cartesian grid (Figure 2.3). Frequencies near the center of k-space, or the origin on the grid, correspond to low frequencies that make up the underlying structure of the image, and higher frequencies provide the resolution or sharpness component of an image<sup>53</sup>. K-space can be transformed into image space with the Fast Fourier Transform (FFT).

An RF pulse excites spins in a tissue volume, but does not offer spatial discrimination. This is done with the application of gradients. The slice select gradient,  $G_z$ , is applied in the z-dimension to select a particular anatomical volume of spins to excite<sup>50</sup>.

Spatial information is encoded in the k-space array of frequencies for the x- and y-dimensions through both frequency and phase. A gradient is applied in the 'readout' or 'frequency encode' direction<sup>54</sup>. The readout gradient has a known center frequency and gradient range, and so a received signal can be located to a specific location within the slice stack. However, this only encodes the information in one dimension. One can imagine a gradient applied through the center of the brain along the y-axis. Each position along that axis will perceive a slightly different gradient strength, and so will differ from its neighbour. However, all points in the x-axis will receive the same gradient strength. In order to make a 2D image from the received signal, the data must also be encoded in the second dimension. This is done through phase encoding. In phase encoding, a gradient is applied for a known amount of time. The longer the gradient is applied, the more phase will be accumulated by a spin. Where the frequency encode

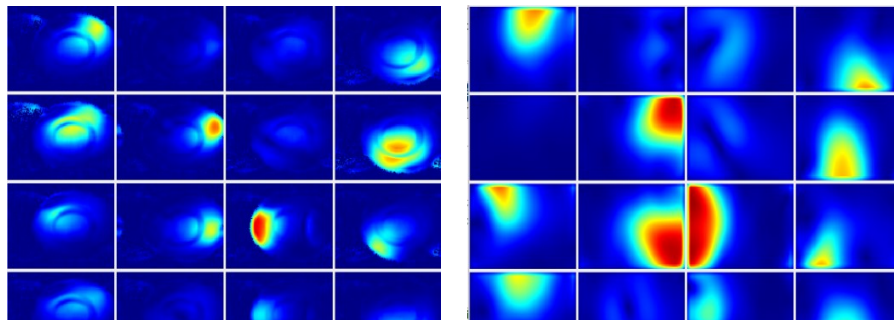
gradient is applied during readout, the phase encode gradient is classically applied one line at a time in phase encoding steps. This can be time consuming, and so alternative methods to reduce phase encoding time have been developed.

### 2.2.1 Parallel Imaging

Parallel imaging (PI) addresses lengthy scan times by reducing the number of collected phase encoding steps<sup>55</sup>. This is done by encoding spatial information in the receive coil using sensitivity maps as well as in the phase encoded spins. The receive coil, or simply coil, contains an array of receive channels for collecting the data. PI images are considered under-sampled since a complete dataset was not collected, and requires additional post-processing in terms of how the images are reconstructed. Depending on the reconstruction method, SNR is approximately reduced by the product of the square root of the under-sampling or PI factor and the geometric factor of the coil configuration<sup>56</sup>. The geometric or g-factor describes the encoding efficiency of a coil array based on the geometry of the receive channel set-up.

#### 2.2.1.1 Coil Sensitivity Maps

Coil sensitivity maps describe the relative sensitivity of each receiver in an array coil to an anatomical location<sup>55</sup>. These maps play a crucial factor in parallel imaging



**Figure 2.4.** Sensitivity maps from a 16-channel array coil. Left: data-derived sensitivities; right: pre-scan sensitivities.

reconstruction by providing some spatial information and reducing the number of necessary phase encoding steps. In general terms, sensitivity maps are derived by dividing a full-FOV image from each receive channel in an array coil by a sum-of-squares image combined across channels<sup>57</sup>. This may or may not be accompanied by normalization of the maps by dividing by a body coil image.

Coil sensitivity maps may be obtained at the beginning of a protocol as part of the pre-scan or may be data-derived (Figure 2.4)<sup>55,56</sup>. Pre-scan maps have the advantage of being acquired once at the start of a scan and so are computationally less expensive. Data-derived sensitivity maps are computationally more expensive because they are derived with each PI image set, but have the advantage of more closely matching the underlying anatomy in the case of movement between the pre-scan and the data acquisition.

Coil sensitivity maps need to be accurate and reliable in order to properly reconstruct an under-sampled image, and so understanding the limitations of these maps is necessary. For maps acquired during the pre-scan, significant patient motion across the span of the acquisition protocol can misalign the acquired maps from the underlying data<sup>55</sup>. This is considered less of an issue in rigid coils such as head coils where the anatomy is confined and movement is limited. In EPI, distortion can play a role in inaccurate sensitivity maps. This can occur if a non-EPI dataset is used to derive the sensitivities for an EPI image with PI, or if an EPI sequence is used to derive maps for an image with a different echo train length (ETL). Corrections for this involve distorting the sensitivity maps with acquired field maps to describe the acquisition-specific

distortion or by increasing the reduction factor to improve distortion. However, areas of strong inherent distortion, such as air-bone interface in the head, are still prone to distortion issues in sensitivity maps<sup>55</sup>. It is also important to note that each channel receives a similar but differently weighted version of the object being imaged, and this includes similar signal from noise. Noise correlation across channels may be amplified and translated into the image when coils are not completely decoupled<sup>56</sup>.

#### *2.2.1.2 Parallel Image Reconstruction*

PI reconstruction can happen in the k-space or image space domains. In k-space, the most common reconstruction methods are Simultaneous Acquisition of Spatial Harmonics (SMASH) and GeneRalized Autocalibrating Partially Parallel Acquisitions (GRAPPA). In SMASH, under-sampled k-space is filled in as best-fit harmonics with known coil sensitivities<sup>56</sup>. However, this method is severely restricted by the coil configuration, and has largely been replaced by more advanced versions and other techniques. GRAPPA is similar to SMASH in that under-sampled k-space lines are filled in within k-space, but it was designed with improved SNR return and less stringent constraints on coil configuration. GRAPPA is best used in inhomogeneous anatomical locations such as in the lungs and abdomen. However, when coil sensitivities are available, image-space reconstruction methods are preferable to k-space methods<sup>55</sup>. Image space methods parse out aliased information, whereas k-space methods estimate data from a least-squares fitting. The dominant image space reconstruction technique is sensitivity encoding (SENSE).

### 2.2.2 Sensitivity Encoding (SENSE)

Sensitivity encoding (SENSE) was developed by Pruessmann et. al. as a reconstruction method using coil sensitivity maps to unfold the aliased images<sup>57</sup>. SENSE reconstruction occurs in the image domain and requires no custom pulse sequence. The general methodology of SENSE is that each coil has an aliased representation of a reduced FOV image with overlapping pixels at a position every 1/R FOV, where R is the parallel imaging or reduction factor<sup>56</sup>. The matrix of coil sensitivities, which is made up of R pixels by number of channels,  $N_c$ , for each spatial location, can be used to relocate each aliased position to its full FOV position, thus resolving the full image. This can be modelled mathematically as an unfolding matrix

$$U = (S^H \psi^{-1} S)^{-1} S^H \psi^{-1}$$

where  $\psi$  is a receiver noise correlation matrix and H refers to the complex conjugate of S, the sensitivity matrix. This unfolding matrix can be applied to the aliased image set,  $a$ , by

$$v = U * a$$

to solve for the unaliased full-FOV image<sup>57</sup>. The noise correlation matrix may be omitted with the understanding that without decoupling the receiver noise, excess noise will persist in the final image and therefore reduce the overall SNR.

SENSE has gained use in applications where MRI signal is acquired with parallel imaging, including in single-shot parallel PI DW-EPI<sup>58</sup>, cardiac imaging<sup>56,57</sup>, contrast-enhanced magnetic resonance angiography, DW-MRI in the brain, and breast imaging<sup>56</sup>.

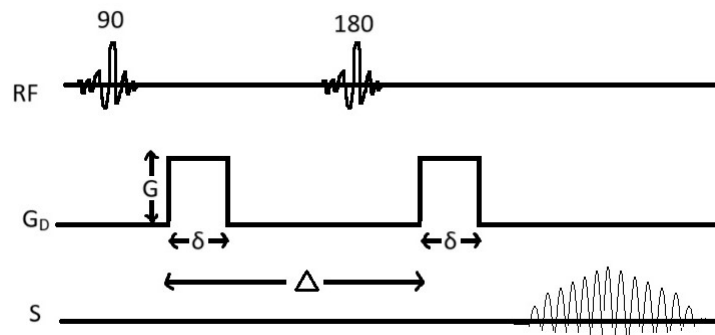


SENSE is limited by the parallel imaging factor in that it cannot exceed the number of receive channels<sup>56</sup>. As well, the SNR is reported to be higher with a lower parallel imaging factor, and SNR is typically negatively impacted after SENSE. Any differences between coil sensitivities and the data to be reconstructed can lead to reduced image quality. This can include any noise in the sensitivities which can propagate into the final image<sup>56</sup>, as well as the previously mentioned distortion differences between EPI coil sensitivities and obtained images. These can be mitigated by proper coil sensitivity processing, specifically smoothing in the case of noise.

### 2.3 Diffusion-Weighted Imaging

Stejskal and Tanner demonstrated the idea of encoding the diffusion of spins under an applied magnetic field over a short time period, setting the groundwork for the idea of diffusion-weighted imaging (DWI)<sup>59</sup>. Diffusion describes molecular motion resulting from thermal energy<sup>60</sup>. Without external restrictions or influence, water molecules will follow Brownian motion, where random diffusion is equally likely to occur in all directions<sup>61</sup>. In the body, barriers in the form of cellular or tissue boundaries act to restrict random diffusion. For example, cerebrospinal fluid flow in the ventricles is relatively unrestricted, so under a short time observation, would appear to follow a relatively unrestricted diffusion pattern. In a section of a blood vessel, diffusion appears to occur freely in the direction of flow, but restricted in others by the vessel walls. A tumor shows restricted diffusion, since water molecules are confined in the tissue mass. In this way, the diffusion properties of tissues can give insight into the local environment and can give contrast to identify pathologies without the need for contrast agents<sup>17,21</sup>.

Diffusion gradients are applied in two blocks of equal duration and strength<sup>62</sup> (Figure 2.5). The first gradient is followed by a 180° spin echo and the second diffusion gradient. In a tissue with limited or restricted diffusion, the set of spins in that volume will not diffuse a significant distance between the first and second gradient. This means that any phase accumulated during the first gradient will be reversed by the second gradient. This gives complete rephasing of neighbouring spins, and the net phase recovery produces a strong signal that translates in a DW image as a bright signal. If,



**Figure 2.5.** Schematic of DW pulse sequence. The 90° RF pulse is followed by the first diffusion gradient of strength  $G$  and duration  $\delta$ . This is followed by a 180° refocusing pulse and a second diffusion gradient of equal strength and duration to the first after a time period  $\Delta$ . Diffusion gradients may be applied along the  $x$ ,  $y$ , or  $z$  axis. Note that this diagram shows diffusion encoding but not acquisition. For acquisition, frequency and phase encoding gradients would follow the second diffusion gradient.

however, molecules in a given tissue are unrestricted and allowed to diffuse freely, spins will diffuse away from their initial position during the first applied gradient. When the second gradient is applied, spins will experience a different gradient compared to the first, meaning that they will not recover their initial phase perfectly. Neighbouring spins are unlikely to be in phase with one another, which leads to a weak produced signal from that tissue and a dark appearance on a DW image. Tissue types with intermediate diffusion restriction will fall somewhere on the greyscale spectrum depending on whether they are more or less restricted.

In practise, all water diffusion in the body is at least in part restricted due to anatomical boundaries, and so diffusion is typically described on a scale of 0 to 1, where 1 is free water diffusion and 0 is no diffusion. This is called the apparent diffusion coefficient (ADC) <sup>62</sup>. ADC maps are derived by the equation

$$S = S_0 * e^{-b*ADC}$$

$$ADC = \frac{\ln(S/S_0)}{-b}$$

where S is the signal at a given b-value and  $S_0$  is the signal without an applied diffusion gradient, or the b=0 image<sup>63</sup>. By this equation, any T1 or T2 effects are cancelled out, and so only water diffusion trends influence the image. These maps are used together with the  $b_0$  and DW images for diagnosis as each provides a unique piece of information.

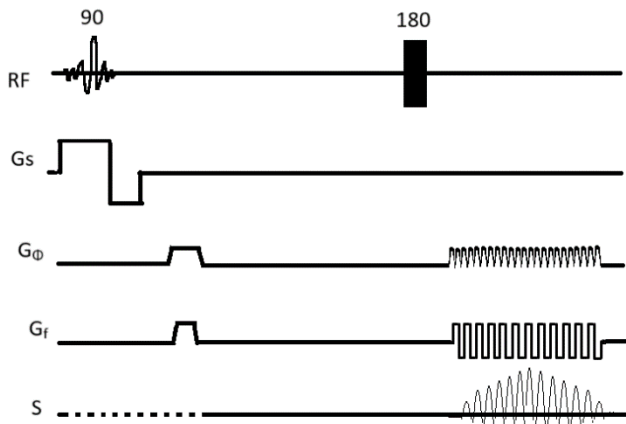
Diffusion gradient strengths, or b-values, are selected to optimize contrast between the tissues of interest. Higher b-values on the order of 1000 s/mm<sup>2</sup> or above better separate tissues based on their ADCs. However, high b-values also evoke less signal and so reduce the overall SNR. For brain applications, a b-value of 1000 s/mm<sup>2</sup> is usually selected<sup>62</sup>.

In theory, molecular diffusion can be encoded on the range of 10  $\mu\text{m}$ <sup>62</sup>. In practise, motion as a result of pulsatile blood flow, cerebrospinal fluid pulsation, and respiration can all interfere with the diffusion measurement and lead to motion

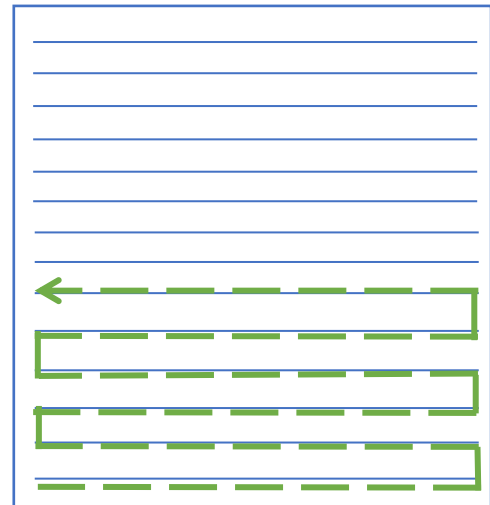
artifacts<sup>60,62,64</sup>. Motion artifacts hindered the uptake of DWI into clinical practise until rapid imaging methods were developed<sup>60</sup>.

## 2.4 Echo Planar Imaging

Echo planar imaging (EPI) is a fast-imaging technique that collects a full representation of k-space after a single radio frequency (RF) pulse<sup>65</sup>. The pulse sequence starts with a 90° pulse and slice gradient followed by preparatory phase and frequency gradients (Figure 2.6). Then, a phase encode gradient is rapidly turned off and on. At the same time a readout gradient is rapidly pulsed between a maximum positive to an equally maximum negative strength. This rapid gradient switching is what allows for the



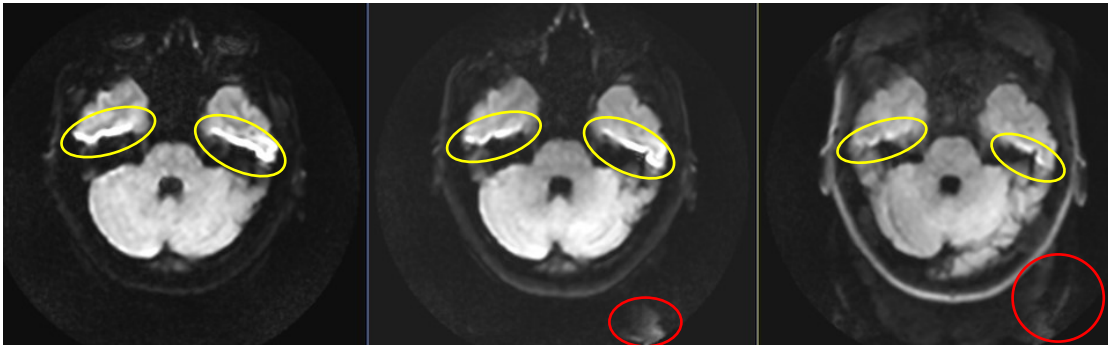
**Figure 2.6.** Schematic of EPI pulse sequence. A 90° RF pulse is delivered with the slice select gradient followed by preparatory phase and frequency pulses. For a spin echo, this may be followed by a 180° refocusing pulse. Simultaneous phase and frequency gradients are rapidly switched to encode and readout k-space, corresponding with signal production.



**Figure 2.7.** Single-shot EPI acquisition. The readout trajectory traverses the entirety of k-space in a single TR.

full k-space to be collected within a single TR. For this to be possible, high performance slew gradients are a hardware requirement to perform EPI. In this case, the slew rate describes the minimum amount of time required to reach the maximum gradient strength<sup>65</sup>.

EPI can happen in a single-shot (ss) or multi-shot (ms) acquisition. In ss-EPI, the entire k-space is collected in one TR (Figure 2.7). However, a concern with ss-EPI is the

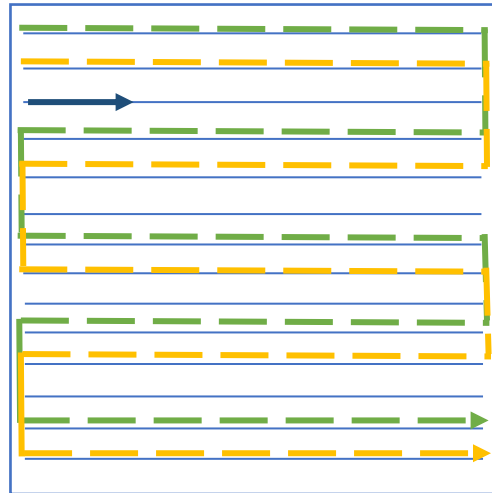


*Figure 2.8. Signal pile-up due to distortion and motion artifact (ghost) levels change with number of EPI shots. Distortion is circled in yellow and artifact in red. Left: single-shot acquisition with clear signal pile-up along the auditory canal and sinuses. No ghosting is visible. Middle: 2-shot acquisition with noticeable but reduced signal pile-up along the auditory canal and reduced across the sinus. Some ghosting from the brightest signal is visible. Right: 4-shot acquisition with reduced signal pile-up along the auditory canal and minimal signal pile-up along the sinus. Significant ghosting is visible outside the brain. All images were acquired on one healthy volunteer at 0.5 T.*

exaggeration of phase errors. Over the duration of the readout, spins lose phase coherence<sup>65</sup>. These phase variations propagate through the readout, and so the longer the readout window, the more phase errors can accumulate. This is particularly exaggerated in regions of susceptibility differences, such as at air-bone interfaces within the auditory canal. These phase errors manifest as distortion in image space (Figure 2.8).

To mitigate this, the window read length can be broken into multiple shots for ms-EPI (Figure 2.9). Increasing the number of shots decreases the time for phase errors to accumulate, thereby decreasing distortion (Figure 2.8). This comes at the cost of increasing the scan time. In practise, a 2- to 4-shot acquisition may be used as a compromise between distortion and scan time.

Another significant issue is the opportunity for motion artifacts between shots. An assumption made during ms-EPI is that the anatomy is in the same place between shots, and so any motion between shots can shift the trajectory of k-space collection and lead to artifacts in the image. To correct for this, motion correction needs to be applied to ms-EPI.



**Figure 2.9.** Schematic of multishot EPI. In this 3-shot acquisition, acquisition starts on the first line, and skips every three lines. It then re-starts on the second, then third line, and repeats the pattern. Yellow=shot 1, green=shot 2, blue=shot 3.

## 2.5 Multiplexed Sensitivity Encoding (MUSE)

Intra-shot motion in ms-DW-EPI manifests as faint, periodic repetitions of the original anatomy, called ghosting artifacts. Estimating and correcting for intra-shot phase errors could theoretically remove the ghosting artifact. This was the idea proposed by Chen et. al. in their post-processing technique entitled Multiplexed Sensitivity Encoding (MUSE)<sup>33</sup>. The purpose of MUSE was to correct for the motion artifact without the need for a custom sequence, navigators, or hardware modifications. Similar to SENSE reconstruction, under-sampled datasets with aliased pixels could be resolved with known coil sensitivities. The core SENSE algorithm

$$u_j(x, y) = S_j(x, y)p(x, y) + S_j\left(x, y + \frac{FOV_y}{2}\right)p\left(x, y + \frac{FOV_y}{2}\right)$$

describes the aliased signal  $u$  received by a coil  $j$  is the sum of the product of sensitivities  $S$  and the true signal  $p$  plus the product of the sensitivities and the aliased pixel. In MUSE, instead of standard coil sensitivity maps, phase errors due to motion are calculated from full FOV images from each shot and multiplied into the sensitivities. These full FOV images are estimated using a SENSE reconstruction, since each dataset can be considered an under-sampled aliased image. From Chen et. al.<sup>33</sup>, the phase errors for each shot can be estimated by

$$e^{i\theta(x,y)+c(x,y)} = \frac{TV(p_s(x, y))}{|TV(p_s(x, y))|}$$

where  $e^{i\theta(x,y)+c(x,y)}$  represents the phase term, with  $\theta$  being the unique phase error due to motion between each shot and  $c$  an arbitrary background phase term unrelated to motion. TV is a denoising algorithm of the total variation operated on the SENSE-derived full FOV image  $p_s$ . Modifying the original SENSE equation, the MUSE algorithm is

$$u_j(x, y) = [S_j(x, y) \frac{TV(p_s(x, y))}{|TV(p_s(x, y))|}]D(x, y) + [S_j(x, y + \frac{FOV_y}{Ns}) \frac{TV\left(p_s\left(x, y + \frac{FOV_y}{Ns}\right)\right)}{\left|TV\left(p_s\left(x, y + \frac{FOV_y}{Ns}\right)\right)\right|}]D\left(x, y + \frac{FOV_y}{Ns}\right)$$

The aliased signal  $u$  received by a coil  $j$  is now the sum of the product of sensitivities  $S$ , phase errors, and the true signal  $D$  plus the product of the sensitivities and phase errors of the aliased pixel. This describes a single shot received by a given channel. To modify

this for a multi-shot acquisition, the sign between the true and aliased signals is changed. For clarity, one paper<sup>66</sup> re-writes the MUSE equation as

$$u_{j,k}(x, y) = \sum_{r=0}^{N_s} S_j\left(x, y + \frac{r \times FOV_y}{N_s}\right) p\left(x, y + \frac{r \times FOV_y}{N_s}\right) e^{i2\pi kr/N_s} v_k\left(x, y + \frac{r \times FOV_y}{N_s}\right)$$

where the term  $v_k$  represents the phase errors due to motion and  $e^{i2\pi kr/N_s}$  is the relative shift in k-space trajectory for a given segment in a ms-EPI acquisition. In this term,  $N_s$  is the number of shots. The variable  $r$  is related to  $N_s$  in that they are numerically the same, but further describes how each  $1/r$  segment of the FOV is shifted in k-space.

The basic MUSE concept has been extended for non-cartesian acquisitions using projection onto convex sets (POCS-MUSE)<sup>66</sup> and with deep learning<sup>67</sup>.

Some limits apply to the MUSE algorithm. The number of shots in a ms-EPI acquisition is limited by the number of coil channels, for similar reasons to the SENSE reconstruction<sup>33</sup>. There is an inherent assumption magnitude is constant across shots, meaning that intra-shot differences are limited to phase. This implies that significant motion impacting the intra-shot signal magnitude cannot be handled by MUSE. Additionally, phase errors are assumed to be from motion only, and so MUSE does not impact any *inter-shot* phase errors that lead to distortion<sup>33</sup>. As discussed previously, MUSE has been implemented at clinical field strengths with increased b-values. However, it is unknown whether MUSE is limited by SNR in reduced cases, such as at a lower applied field strength.



### 3. Experimental Methods and Pipeline Engineering Design

This thesis explores the design decisions that impact image quality and artifact levels in a MUSE reconstruction of ms-DW-EPI at 0.5 T. The system design (i.e. acquisition protocol, data transfer, reconstruction pipeline) was in flux throughout the duration of the thesis research. This chapter presents a comprehensive overview of how these design decisions were made including candidate alternatives and the criteria used to select the optimal option. The MRI system, data collection, acquisition parameters, pipeline development and optimization, and data evaluation are discussed.

#### 3.1 Experimental Methods

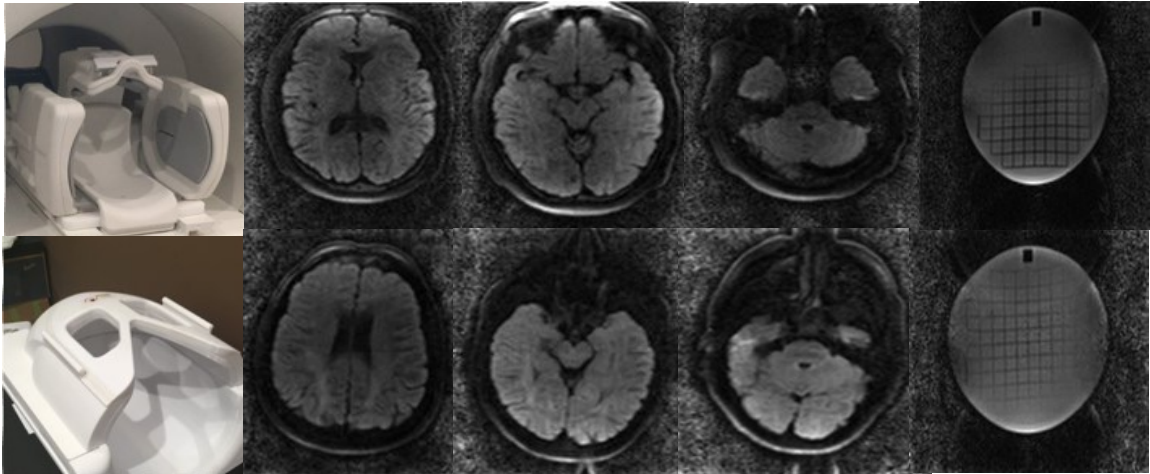
##### 3.1.1 MRI System

The MRI used for this project needed to i) meet the hardware requirements of strong, rapid gradients in order to acquire the DW-EPI data and ii) have a field strength below clinical standards of 1.5-3 T. To address these requirements, the 0.5T Synaptive Medical MRI was used (Figure 3.1). This system was available for research in the BIOTIC lab at the Halifax QEII Hospital as a head-only device. The system gradients have a peak strength of 100 mT/m and slew rate of 400 T/m/s<sup>68,69</sup>. Previous work has demonstrated comparable DWI image quality on this system to that obtained from a clinical system, even in the presence of metal implants<sup>70,71</sup>. For comparison at clinical field strength, the 3T GE Healthcare MRI in the QEII Hospital was also used.



*Figure 3.1. Synaptive 0.5 T MRI.*

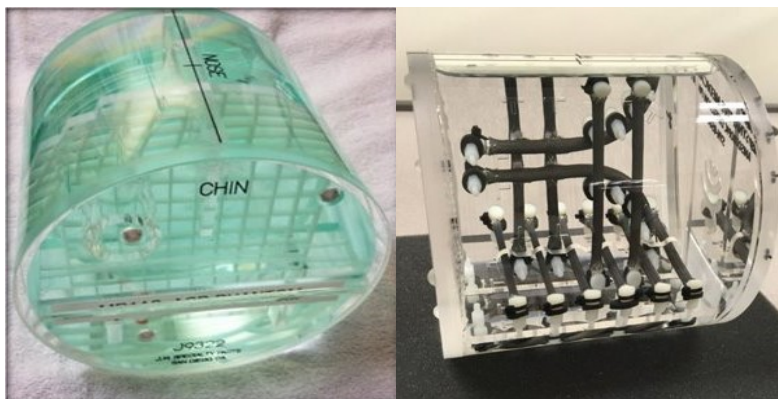
The head coil was required to have a sufficient number of channels for parallel imaging and sufficient signal to produce accurate sensitivity maps. A 16-channel and 8-channel head coil were considered. The 16-channel had adjustable side panels to maximize the filling factor of the object with the receiver, whereas the 8-channel was a rigid clip-in style. Comparing image quality in the two coils (Figure 3.2) the 16-channel gave brighter signal around the periphery of the object whereas the 8-channel produced a balanced image in terms of signal intensity from the superficial to deep structures. The 16-channel could be used with a larger parallel imaging factor, but the deeper range of sensitivities in the 8-channel resulting from each channel having a larger diameter produced superior coil sensitivity maps. The 8-channel was selected for the project.



**Figure 3.2.** Comparison of coil images across anatomical position and in an ACR phantom. Top row: 16-channel coil with example images; bottom row: 8-channel coil with example images.

### 3.1.2 Phantoms

MRI phantoms were used for quality control and pipeline development. The large ACR phantom is an accepted standard for evaluating image quality<sup>72</sup>(Figure 3.3). Built-in features with varying susceptibility and physical structures can be used to evaluate resolution and distortion. The Synaptive diffusion phantom was used to investigate whether diffusion was observable, and how diffusion directions were stored within the obtained k-space dataset (Figure 3.3).



**Figure 3.3.** MRI phantoms were used for quality control imaging. Left: Large ACR phantom. Right: Diffusion phantom (Synaptive Medical).

### 3.1.3 Human Participants

Volunteers and patients were recruited for imaging at 0.5 T under an existing technique development ethics entitled "*Development and Optimization of Point-of-Care Magnetic Resonance Imaging*" (Romeo File No. 1025269). To compare image quality to that of the clinical standard, some volunteers and patients were recruited for imaging at 3T under an existing technique development ethics entitled "*Research Sequence Development for 3 Tesla Magnetic Resonance Imaging*" (Romeo File No. 1024276). The decision to include or exclude scanning at 3 T was made based on the progress of the project, i.e. if a comparison to standard image quality and distortion levels were necessary. The number of volunteer subjects was limited to the maximum number that were approved by the hospital's research ethics board. A total of six healthy volunteers (4 female, mean age =  $27.5 \pm 4.1$  years old) were recruited with the standard MRI exclusion criteria for a 30-60 minute scan at 0.5 T. Four of the six healthy volunteers were also recruited for a 30-minute scan at 3 T. Three patients (2 males, mean age  $44.7 \pm 23.2$  years old) were recruited for scanning at 0.5 T. Patient candidates were identified by clinical collaborators based on a diagnosis of first-time presenting cholesteatoma. Clinical scan images obtained at 3 T and with high-resolution CT were acquired from the data analysis server used by physicians as allowed under the REB approved protocol.

### 3.1.4 Acquisition Parameters

The parameters used to acquire the ms-DW-EPI data were modified and optimized throughout the duration of the MUSE pipeline development. The vendor DW-EPI protocol was used as a standard, and parameters such as number of shots, averages, matrix size, and image readout were manually adjusted on the MRI console before a

scan. The initial priority was to match image integrity between the images reconstructed with the MUSE pipeline and those reconstructed with the proprietary vendor reconstruction pipeline, or the vendor reconstructed images. Then, priority shifted to correcting the motion artifact, and then to optimizing for the clinical application. The rationale for these protocolling choices is described below.

#### *3.1.4.1 Number of shots*

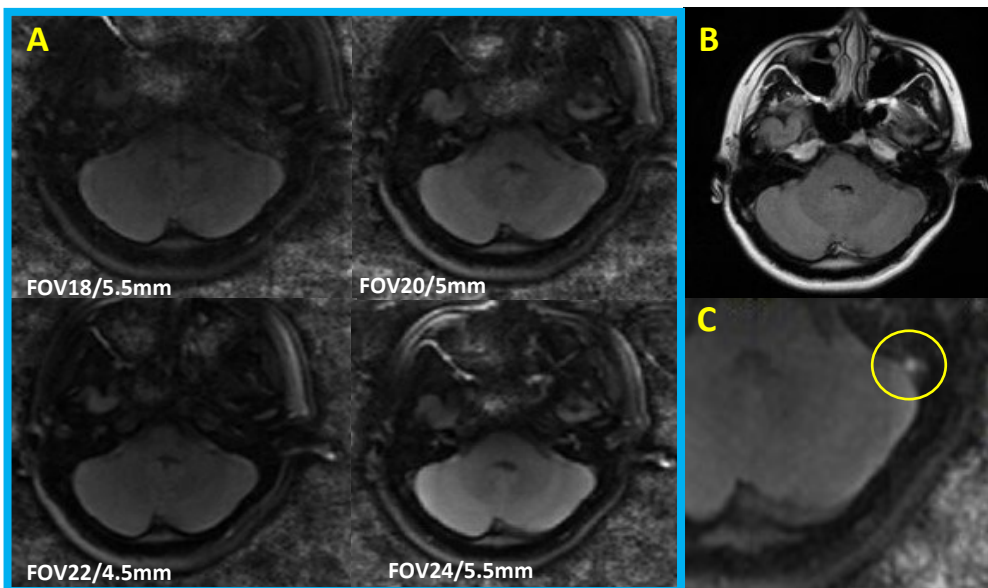
The number of shots impacts the ghosting and distortion levels. Initially, a 1-shot acquisition with minimal ghosting was acquired so that image quality could be matched between how the images were imported into Matlab and the vendor reconstructed images. Then, the number of shots was increased to 2 and 4. By doing so, a motion ghost artifact was introduced. This probed whether MUSE was implemented correctly, as increasing the number of shots would be expected to increase the level of ghosting. For the clinical application, 3 shots were collected. This was expected to reduce distortion more than a 2-shot, while introducing less ghosting artifact than a 4-shot.

#### *3.1.4.2 Number of averages*

For this work, a diffusion direction and strength is replicated for each shot and slice, and each replicate is called an average. In the vendor reconstructed images, the averages were always combined. In the current pipeline, the k-space for each individual averages was obtained before they were collapsed. Increasing the number of averages increases the overall scan time but also improves the SNR. The number of averages was selected such that the total time for one acquisition scan was around 5 minutes. This ranged from 6 to 8 averages.

### 3.1.4.3 Slice thickness, FOV, and matrix size

The slice thickness, FOV, and matrix size interrelate to create image resolution and voxel size. High image resolution gives crisper boundary visualization, but at the cost of smaller voxel size and lower produced SNR. In the literature, ideal slice thickness for recurrent cholesteatoma imaging with DW-MRI is 2-5mm<sup>11</sup>. The minimally acceptable matrix size and FOV were derived with the goal of achieving 2mm slices to match the literature gold standard. To assist with these protocolling decisions, images were obtained with FOV/slice thickness of 18 cm/5.5 mm, 20 cm/5 mm, 22 cm/4.5 mm, and 24 cm/5.5 mm (Figure 3.4). These image sets were presented to an experienced neuroradiologist, who was asked to evaluate the images for overall quality and diagnostic preference. Thin slices were preferred over thick to avoid flow artifacts (Figure 3.4 C), and a smaller FOV was preferred, but both thin slices and a small FOV were requested. The current protocol obtains 2mm slices with a small matrix size of 96 by 96 and a FOV between 17.6 and 19.2 cm.



**Figure 3.4.** Optimizing spatial resolution. A: Variations in FOV and slice thickness for comparable voxel size; B: Anatomical comparison of comparable slice; C: Flow artefact (yellow circle) in FOV18/5.5mm.

#### *3.1.4.4 Frequency Encode Direction*

The default setting in the DW-EPI protocol was to have the setting 'switch frequency' (SF) toggled on such that the readout was in the left-right direction. Antialiasing filters are applied in the frequency encode direction, meaning that it is preferable to have the readout in the direction of the longest anatomical plane to avoid wraparound of the anatomy. To switch the readout direction, SF was toggled off. Although the online reconned images appeared normal, the MUSE images were unexpectedly poor. This prompted an exploration into the impact of input anatomical offsets on image quality (Appendix V). An offset in the phase encode direction impacted MUSE image quality, not vendor reconstructed images. This could not be replicated by Synaptive engineers, and the source of the issue could not be addressed within a reasonable timeline. Since the typical added AP offset was small (10-15mm), and it did not interfere with visualizing the anatomy of interest or cause any excess wraparound, it was decided that no AP offset would be added going forwards, and readout would be in the AP direction.

#### *3.1.4.5 Working Protocol*

Acquisition parameters were in flux throughout the pipeline development as the theoretical SNR output was varied and a protocol was optimized, which was reflected in the parameters used to scan the first four healthy volunteers (Appendix VII). The final protocol was used to scan the three patients and two healthy volunteers and consisted of three DW-EPI acquisitions: 1-shot with PI2 (TE=64.7 msec, matrix =88x88, FOV 17.6 cm, slice thickness=2mm, slice spacing=2mm), 2-shot (TE=64.5 msec, matrix =88x88, FOV 17.6 cm, slice thickness=2mm, slice spacing=2mm), and 3-shot (TE=59.4 msec, matrix =96x96, FOV 19.2 cm, slice thickness=2mm, slice spacing=2mm). A balanced

steady state free precession (bSSFP) acquisition was selected for anatomical comparison due to its high SNR efficiency and demonstrated high resolution at 0.5 T<sup>73</sup>.

### 3.2 Pipeline Engineering and Optimization

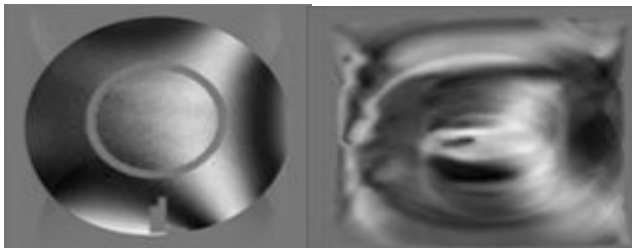
Although MUSE is an established reconstruction technique, it is not available on all MRI systems and is not publicly available. Therefore, an offline, non-vendor reconstruction pipeline needed to be developed to investigate the hypothesis in this thesis. Matlab (Matlab R2022b) met the requirements for this project of having matrix functions and consistency with other lab-developed pipelines. The pipeline design and engineering are described below. Briefly, data is transferred from the MRI system computer to the data analysis server and partially reconstructed to obtain cartesian-gridded k-space. This k-space is transferred into Matlab. Coil sensitivities and phase variations are derived from the data. Final unaliased images are solved for as per the MUSE reconstruction process<sup>33</sup>.

#### 3.2.1 Data Organization

Unprocessed data collected during an acquisition protocol is temporarily stored on the MRI console and can be captured as raw k-space. The k-space is transferred to the data storage server and then the data analysis server, where it can be organized and reconstructed.



MUSE reconstruction requires cartesian-gridded k-space. The raw k-space data exists as unorganized lines of k-space that need to be interpreted and restructured using the accompanying metadata. Two techniques were considered for this purpose. First, existing Matlab code from the lab was modified for DW-EPI data. However, the code could not correctly grid the k-space data. Alternatively, an offline reconstruction pipeline was provided by Synaptive through a Docker container. This pipeline was identical to the vendor reconstruction, but had been modified to produce reconstruction intermediates called breadcrumbs. Any early processing on the data in the vendor reconstruction would be reflected in the breadcrumbs, and so any reconstruction differences would be limited to those provided by the MUSE reconstruction. The pipeline reflected the latest version of the vendor reconstruction pipeline and was not backwards-compatible with previously acquired data (Figure 3.5).

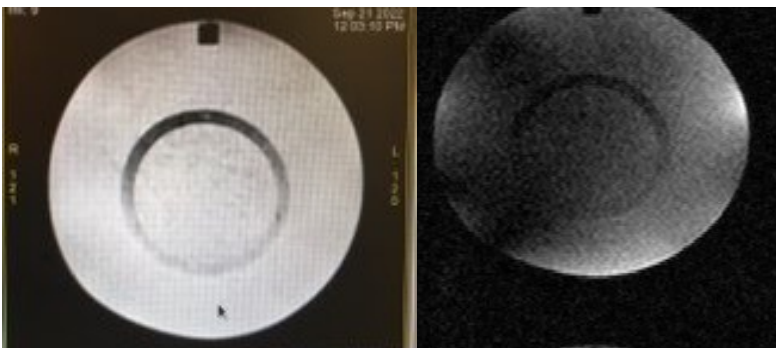


*Figure 3.5. Early versions of the offline reconstruction revealed acquisition specificity of the pipeline. Left: New collected axial 2-shot DWI. Right: DW-EPI data collected previously.*

The two breadcrumbs used for this project were hybrid images and coil coefficients. Hybrid images were matrices with one dimension in image space and the other in k-space. These could be converted into cartesian-gridded k-space by the FT in the image-domain dimension and served as the source of primary data for the project. The coil coefficients were coil sensitivity maps obtained at the beginning of the acquisition

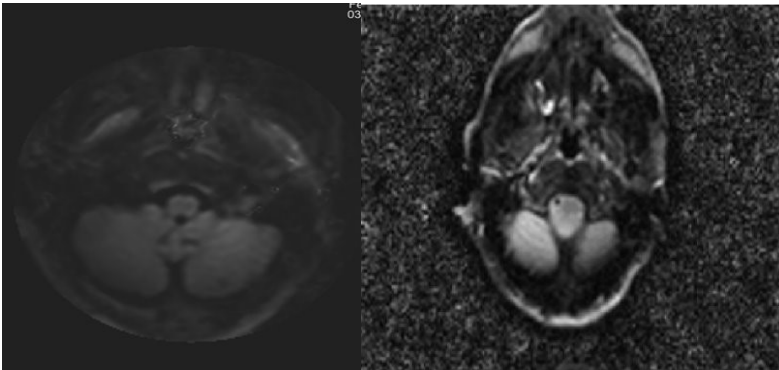
protocol. Hybrid image datasets were imported into Matlab as a matrix of size of  $[N_x, N_y, N_z, N_s, N_d, N_a, N_c]$ , representing x-matrix size, y-matrix size, number of slices, number of shots, number of diffusion directions, number of averages, and number of coil channels, respectively. As a sanity check, a 2D FFT was performed on this k-space and was saved as a separate image-space matrix.

The offline partial reconstruction pipeline underwent several iterations throughout the duration of the project. Significant problems, such as requiring different output breadcrumbs or errors in the reconstruction process (Figure 3.6, Appendix VI), led to modified versions of the pipeline. Minor issues, such as needing to modify optional reconstruction parameters, were addressed by overriding the default reconstruction parameters. This was done by including a text file in the reconstruction command, which took precedence over the default settings and circumvented the need for an entirely new reconstruction pipeline. The current version of the pipeline produces individual hybrid images for each shot, diffusion direction, slice, average, and receive channel.



*Figure 3.6. Example of FOV shift between online reconstruction image (left) and Matlab rendering of hybrid image in image space (right). Image was acquired as a 1-shot EPI with one average.*

The vendor reconstruction images were used as a gold standard for comparison. A few differences were noted in how the data was handled between the vendor reconstruction and Matlab. Notably, the vendor reconstructed images were presented as ADC maps and combined diffusion images, whereas the Matlab images stored  $b=0$  and  $b=1000$  for each diffusion direction separately. The vendor reconstruction had an automatic cropping feature to limit the FOV to a region with sufficient gradient warp correction. If offsets were not entered to center the auditory canal at the start of an acquisition protocol, it was obstructed (Figure 3.7). MUSE images were stretched in the anterior-posterior direction compared to the vendor reconstructed images. This was addressed by resizing the images in Matlab to the standard output size of 256 by 256.



**Figure 3.7.** Visible differences between images from physician data server and MUSE reconstruction. Left: Vendor reconstructed image on server is circularly cropped, obstructing part of the anatomy. Right: MUSE image stretched in the anterior-posterior direction compared to physician data server image. Slices were selected to exemplify FOV cropping and stretching, respectively, and are not slice matched to each other.

### 3.2.2 Sensitivity Maps

Coil sensitivity maps describe the relative sensitivity of each channel in a receive coil to a position in the anatomy. These maps must be accurate for proper reconstruction of under-sampled data with SENSE and MUSE. In this work, coil sensitivity maps were necessary for both the SENSE reconstruction to derive the phase errors due to motion, as well as the final MUSE calculation.

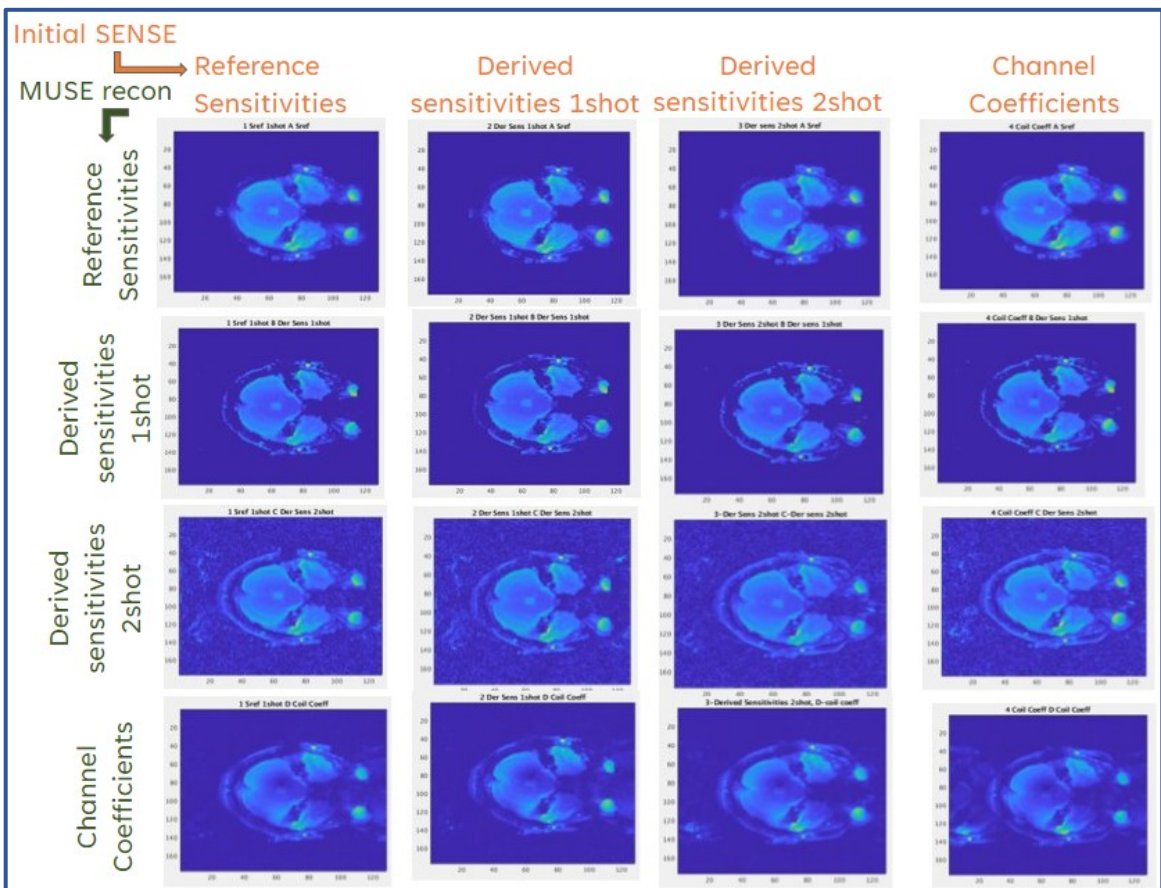
Two sources for these sensitivity maps were considered. First, channel combination coefficient breadcrumbs corresponding to sensitivity maps for each channel were output from the offline reconstruction pipeline. These were suspected to have similar post-processing to the acquired cartesian-gridded k-space from the hybrid images, and so were the first choice for coil sensitivities. The breadcrumbs were obtained in an intermediate FOV and were interpolated to match the size of the hybrid images.

To better understand the behaviour of these breadcrumbs, acquisition parameters that were anticipated to be modified during this project were adjusted one at a time, and the corresponding sensitivity maps were plotted (Appendix VIII). A visible change was expected with switching the frequency encode direction and increasing field of view. Likewise, no visible change was expected and observed with increasing the number of shots. There was no visible change when the subject was asked to move during the acquisition, suggesting the maps were collected during the pre-scan only, and not re-collected with each acquisition.

Alternatively, sensitivity maps could be derived directly from the data. The following pseudocode describes this process for each individual slice summed across averages, as described in an available tutorial<sup>74</sup>.

- 1** Inverse 2D FFT of Hanning-filtered data for b=0 k-space
- 2** Sum of squares of image data across coil channels
- 3** Matrix division of images from **1** divided by **2**

These two methods were compared for their representation of the physical object as well as the output image quality from the SENSE algorithm. For an initial understanding of how the SENSE estimation for phase maps and MUSE reconstruction depend on the sensitivities, a comparison of derived sensitivities from 1-shot and 2-shot data, channel combination coefficients, and reference sensitivity derivations from literature<sup>75</sup> was performed (Figure 3.8).



**Figure 3.8.** Comparing image reconstruction with variations of coil sensitivities. In each column from left, the first SENSE step was performed with sensitivities derived from: literature sensitivity method, 1-shot dataset, 2-shot dataset, and channel combination coefficients. In each row from top, the MUSE step was performed with sensitivities derived from: literature sensitivity method, 1-shot dataset, 2-shot dataset, and channel combination coefficients. Ghosting and noise is largely dependent on secondary MUSE reconstruction. The 1-shot derived sensitivities performed best overall with any initial sensitivity. Coil coefficients and 2-shot derived sensitivities left noise and ghosting, indicating that MUSE was not functioning correctly.

The 1-shot sensitivities performed best for both the initial SENSE and final MUSE, and the channel coefficient breadcrumbs left the most ghosting, suggesting that they were not working effectively. A few differences may have contributed to this.

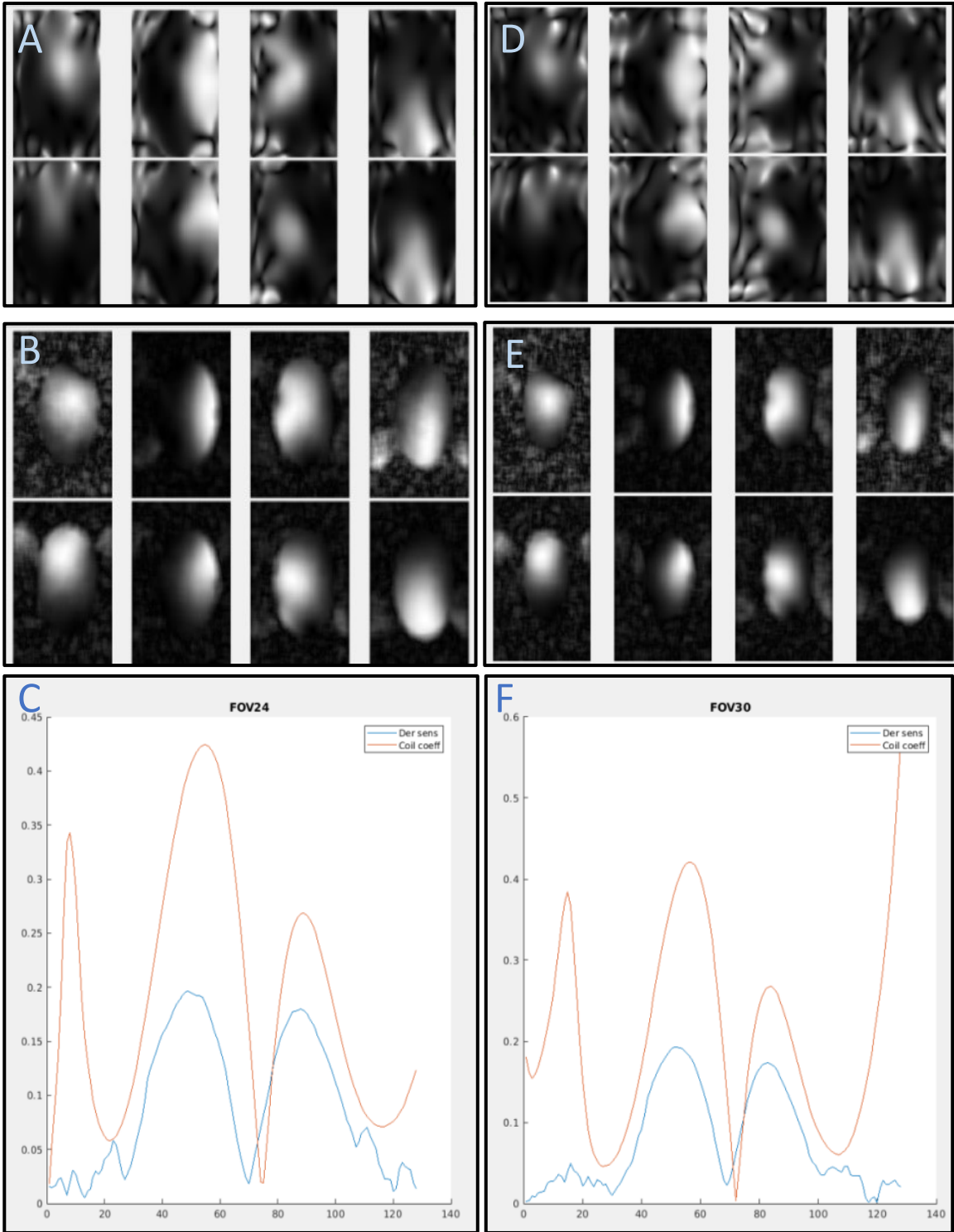
First, there was a noticeable shift in the x-direction between the coil combination coefficient breadcrumbs and the derived sensitivities (Figure 3.10 E & F). An intensity plot through the center of a representative coil sensitivity for both the breadcrumbs and derived sensitivities suggested a consistent yet slightly shifted intensity pattern between the two (Figure 3.10 C & F). This contradicted what Synaptive engineers observed, where the observed intensity patterns for their derived sensitivities matched the coil coefficients exactly. This was resolved with a modification of the offline reconstruction pipeline.

With this update to the offline reconstruction pipeline, a separate coil coefficient breadcrumb was produced for each average, shot and diffusion direction. Visual inspection revealed that they were identical for a given average and diffusion direction and similar across shots, but that they were being replicated due to the configuration of the upgrade (Figure 3.9).



*Figure 3.9. Channel combination coefficient breadcrumbs across diffusion directions. No visible differences were observed.*

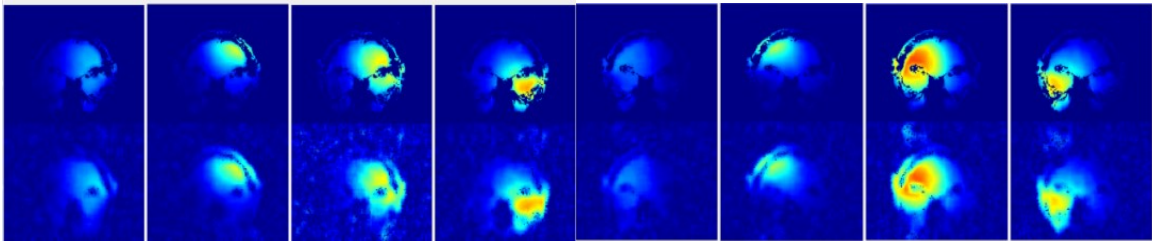
An FOV discrepancy was identified between the coil coefficient breadcrumbs and the derived sensitivity. The coil coefficients appeared to be 'zoomed in' compared to the derived sensitivities and the object of interest (Figure 3.10 B & E). This observation was consistent across fields of view. The apparent FOV difference was suggested to be a restriction put on the coil coefficients to mitigate abrupt changes in sensitivities, but may have also resulted from EPI distortion. For an EPI acquisition, the channel coefficient breadcrumbs were calibrated from undistorted gradient echo images, since EPI is known to have geometric distortions from B0 inhomogeneities. The idealized coil coefficients may not have matched up closely enough with the distorted image collected with EPI. At this point, it was decided that channel combination coefficients were not an ideal fit for the current project, and so focus turned to optimizing the derived sensitivities.



**Figure 3.10.** FOV difference between coil coefficient breadcrumbs (coil coeff) and derived sensitivities (der sens). At FOV 24cm, the coil coeff (A) show a circular object occupying the full panel and the der sens (B) representing the expected FOV. An intensity map through the middle of the sensitivity plots (C) for both der sens (blue) and coil coeff (red) shows shifted peaks and valleys. Similarly at FOV 30 cm, the coil coeff (D) appear zoomed in compared to the der sens (E), and again the peaks and valleys are shifted in the coil coeff compared to the der sens when the center of the sensitivities are plotted (F).



Initially, sensitivities were derived from a 1-shot, multi-average dataset that was collected in addition to the multi-shot data in a given scan. This was done so that the data was fully sampled and unaliased. However, minimizing scan time is preferable for patient comfort, and so an alternative pseudo 1-shot dataset derived from data already being collected was explored. This was done by combining the k-space from the multi-shot acquisition across shots in addition to averages for each given slice. Although previously investigated, improvements to the pipeline as a whole warranted a further look. Comparing the general appearance of 1-shot derived and multi-shot or pseudo 1-shot derived sensitivities (Figure 3.11), sensitivity patterns were similar. The pseudo-1-

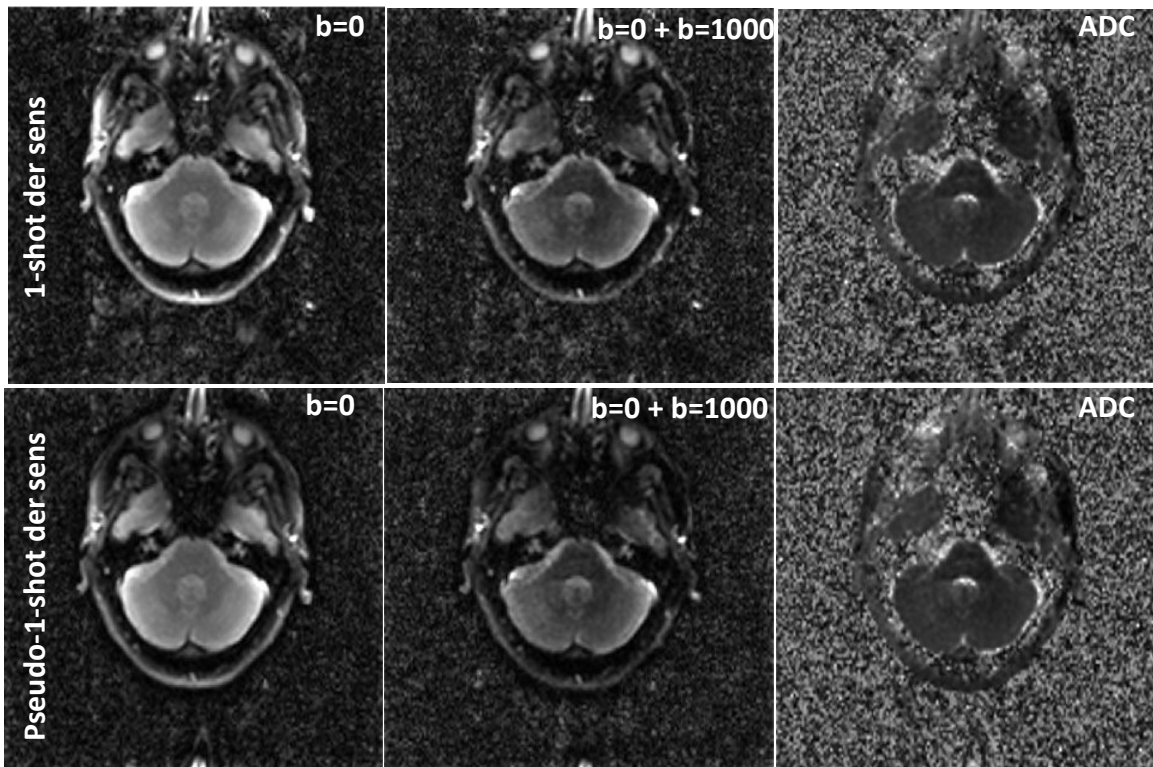


**Figure 3.11.** Comparison of 1-shot derived (top row) and 2-shot derived (bottom row) sensitivities. Top row shows sensitivities derived from 1-shot data. Bottom row shows sensitivities derived from 2-shot data combined to create a pseudo-1-shot dataset.

shot derived sensitivities appeared more blurred across regions of transition (e.g. between the skull and cortical tissue) compared to the crisp transitions in the 1-shot derived sensitivities. As well, the background noise was more prominent with potential residual ghosting in the pseudo-1-shot. However, it was reasoned that this could be addressed by adjusting the filtering and smoothing functions. Looking at the MUSE output images using either 1-shot or pseudo-1-shot derived sensitivities for both the initial SENSE estimation and the MUSE step, the overall image quality was similar for  $b=0$ , combined diffusion directions, and ADC maps regardless of which sensitivity map

was used (Figure 3.12). Images reconstructed with the pseudo-1-shot derived sensitivities had comparable ghosting levels to images reconstructed with 1-shot derived sensitivities. This evidence, along with the added benefit of removing the need for an additional scan, supported the use of the pseudo-1-shot derived sensitivities for the rest of the project.

Next, focus turned to optimizing the derived sensitivities. This included smoothing and filtering considerations. Initial smoothing was done following the method outlined in the SENSE tutorial<sup>74</sup>. The following pseudocode describes the logic of deriving sensitivities.



**Figure 3.12.** Output images from the MUSE pipeline using 1-shot derived and pseudo 1-shot derived sensitivities. Top row shows 1-shot derived sensitivities (*der sens*) and bottom row shows pseudo-1-shot *der sens*. Residual ghosting is strongly evident in the 1-shot *der sens*  $b=0$  and combined diffusion direction ( $b=0+b=1000$ ) images, and some residual ghosting in the pseudo-1-shot  $b=0$  and  $b=0+b=1000$  images. This is particularly noticeable with the image right-side ear, which is a particularly bright feature. Note that the wraparound of the nose in each of the images is not indicative of ghosting.

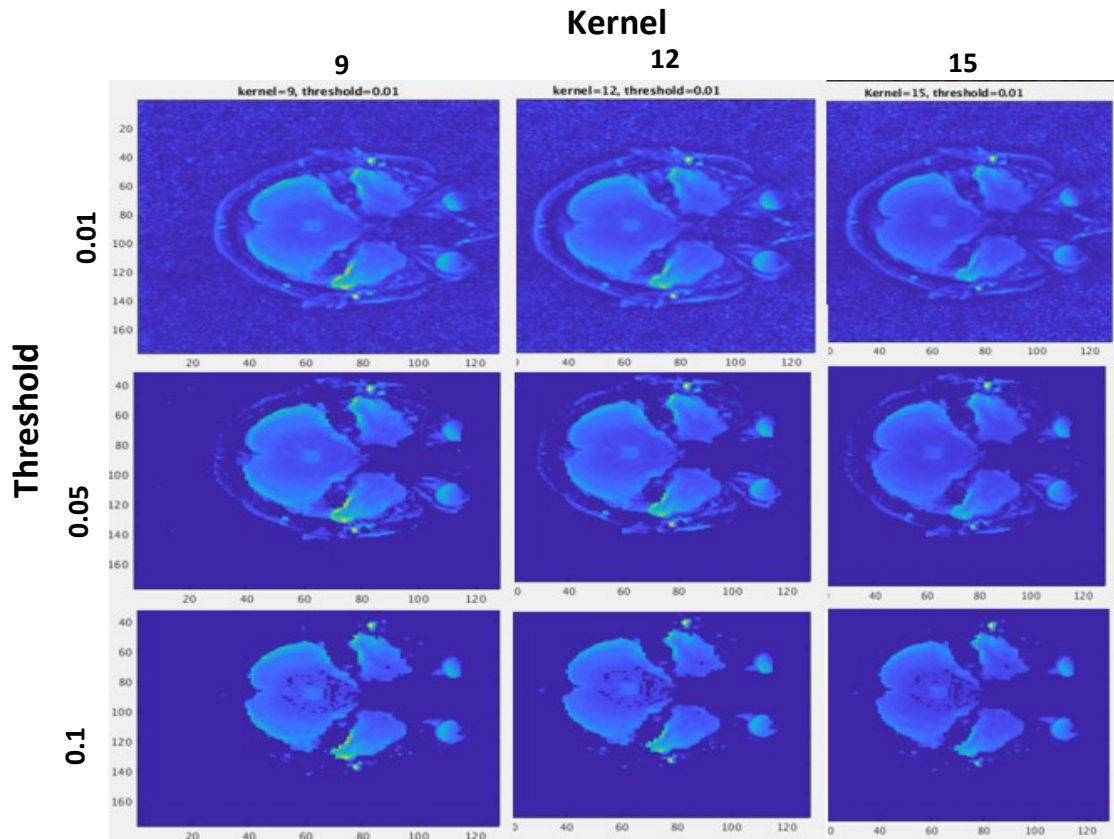
## **% Data prep**

- 1** Load individual shots of k-space as 'dataset'
- 2** Perform 2D inverse FFT of cropped dataset to obtain image space

## **% Derive sensitivities**

- 3** Transform across coils by  $(\sum_{l=1}^{N_c} |img|^2)^{1/2}$  where img is the 2D inverse FFT of dataset
- 4** Divide **2** by **3** to obtain an estimate of coil sensitivities
- 5** Perform 2D convolution on sensitivities from **4** to obtain smoothed sensitivities
- 6** Define a threshold to differentiate region of interest from background
- 7** Define a mask of values in image above threshold
- 8** Apply mask to smoothed sensitivities
- 9** Set masked values (ie 0-values) to 80% of the maximum

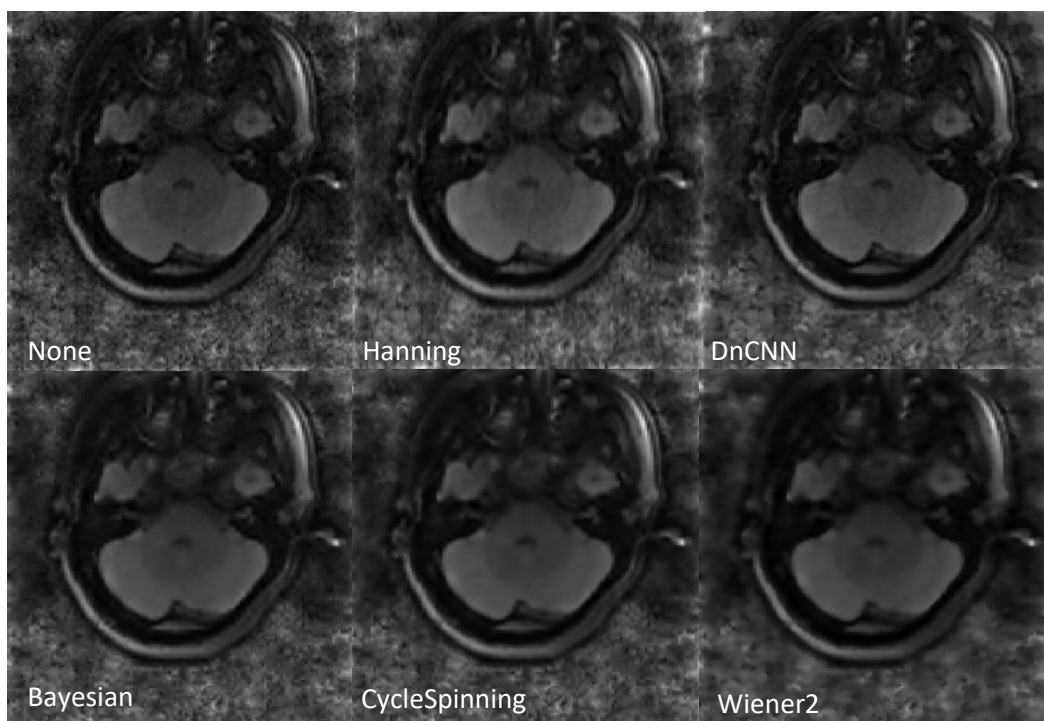
This used a smoothing kernel on each of the channels. The kernel indicates the size of the smoothing function as a matrix of ones and is optimized for area coverage without losing image reconstruction integrity. After smoothing, a threshold mask was applied to suppress noise. Since the overall performance of the sensitivities was dependent on both the smoothing and threshold mask functions, variations of the two were tested to determine the optimal combination (Figure 3.13). The threshold value between 0.01 to 0.1 was multiplied by the maximum pixel value and anything below was set to zero. Increasing the threshold improved the background noise, but also degraded



*Figure 3.13. Investigating optimal threshold and kernel size combinations for sensitivity masking.*

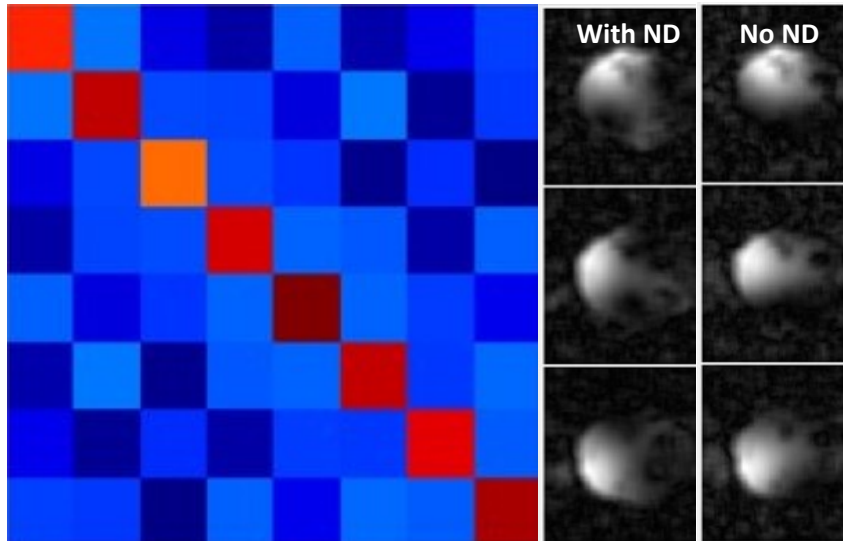
the periphery of the image. An intermediate combination using a kernel of 12 and threshold of 0.05 was selected.

Alternative methods for filtering and denoising the sensitivities were considered (Figure 3.14). It was decided that filtering during the smoothing function was sufficient, and so pre-filtering was omitted going forwards.



**Figure 3.14.** Denoising considerations for derived sensitivities. Denoising in *k*-space looked at the Hanning filter. Image space denoising included a deep neural network (DnCNN), wavelet denoising with Bayesian and CycleSpinning methods, and a Wiener2 filter. The Hanning filter and DnCNN most closely represented the original image, while the wavelet and Wiener2 filters were blurred versions of the original.

A significant issue with the derived sensitivities was artificial noise enhancement during the matrix inversion during the SENSE step, which escalated the background noise. In addition to the aforementioned filtering methods, several strategies were investigated to address this. First, a method in the literature to decorrelate noise across channels with a noise decorrelation matrix and multiply them into the sensitivities before SENSE reconstruction was implemented<sup>76</sup>. While this concept did change the appearance of the coil coefficients (Figure 3.15), it was not necessarily improving the noise. Therefore, this method was abandoned. Second, a denoising algorithm called TV-L1 denoise, which will be discussed further in regards to the phase errors, was applied to the coil sensitivity maps in an attempt to remove the noise. However, this method was too aggressive even if the denoising rigor was lowered significantly.



*Figure 3.15. Noise decorrelation matrix trials to address excess background noise. Left: intensity map of noise correlation across 8 channels. Dark red indicates strong correlation and dark blue indicates weak correlation. Center diagonal line of red squares indicates correlation between same channels. Right: Sample coil sensitivity maps with and without noise decorrelation.*

The end protocol for addressing the noise in the sensitivity maps applied a mask using a threshold of between 15-20% of the maximum intensity from the pseudo-1-shot image and multiplying it by the sensitivity maps. This was followed by setting any zero value to 0.8. This prevented the noise from being amplified during the matrix inversion and multiplication. In addition, during the matrix inversion step, a tolerance was set such that values under the set value were treated as zero and were not inverted. It was found that each dataset varied in noise intensity, and so the threshold and tolerance values had to be adjusted slightly for each dataset. With this, the coil sensitivities were deemed to be optimized for the current project.



### 3.2.3 SENSE Estimation of Images

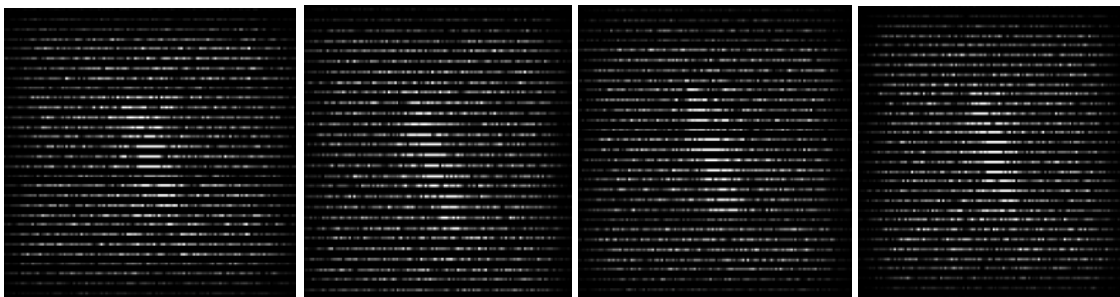
For both the SENSE and MUSE steps, each diffusion direction and slice were processed and stored separately. The channels were combined during the SENSE and MUSE algorithms. Separate shots were processed and stored separately for the SENSE reconstruction and combined during the MUSE reconstruction.

The initial stages of pipeline development began with an in-depth exploration into sensitivity encoding (SENSE) logic. SENSE is a technique used to reconstruct under-sampled data from parallel imaging using coil sensitivities and aliased data. In traditional parallel imaging, data is under-sampled by some factor in order to reduce scan time, and the missing data is approximated with the coil sensitivities. In this project, a full dataset representing all lines of k-space is collected, but the collection is broken into multiple shots. Each of these shots contains an under-sampled representation of the full k-space, where every  $n$ th line is omitted as dictated by the number of shots (Figure 3.16). Therefore, each shot can be treated as an under-sampled dataset (Figure 3.17), and SENSE can be used to reconstruct a full FOV image for each shot (Figure 3.18). This is important because these estimated full images provide insight into the phase variations due to motion between each shot and are used further in the pipeline to correct for motion. Note that this section will largely focus on SENSE, but was worked on in tandem with the MUSE reconstruction, and so comparisons between the two are discussed.

A publicly available SENSE tutorial with Matlab code<sup>74</sup> was used for learning the algorithm and as a starting outline to work off of, and remained an integral part of the pipeline. The following pseudocode describes the framework of the SENSE pipeline.

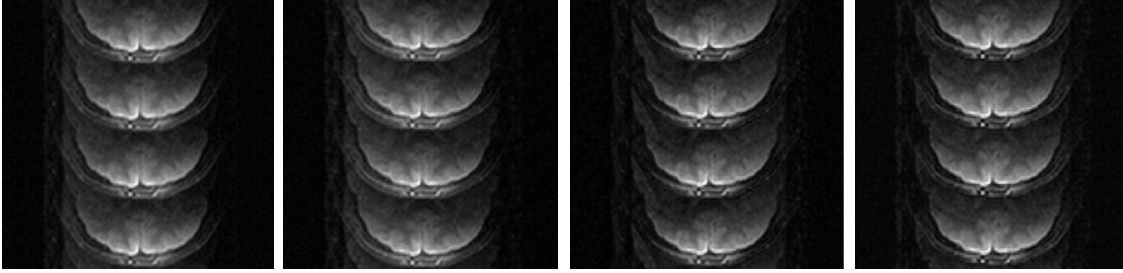
Early exploration of the SENSE algorithm followed the SENSE tutorial closely. This included using the provided raw data, copying the code over and adjusting for the current version of Matlab, and verifying that the obtained results matched the expected results. This also allowed opportunity to adjust variables in the built-in Matlab functions to investigate their function. Next, an acquired 1-shot dataset was run through the pipeline, which exposed specific characteristics unique to the acquired data that required pipeline modification. One important modification was in how the data was looped over. This involved switching from looping over the top half of the image and the entire left-right extent to looping over the entire top-bottom extent and  $1/N_s$  of the left-right extent. This translated into the following pseudo-code.

```
% Loop over the one side of the image  
  13 For  $1/N_s$  of  $y$   
    % Loop over the entire image  
      14 For 1 to the size of  $x$   
        15 Pick out the sub-problem sensitivities  
        16 Solve the sub-problem in the least-squares sense  
      End  
    End  
End
```

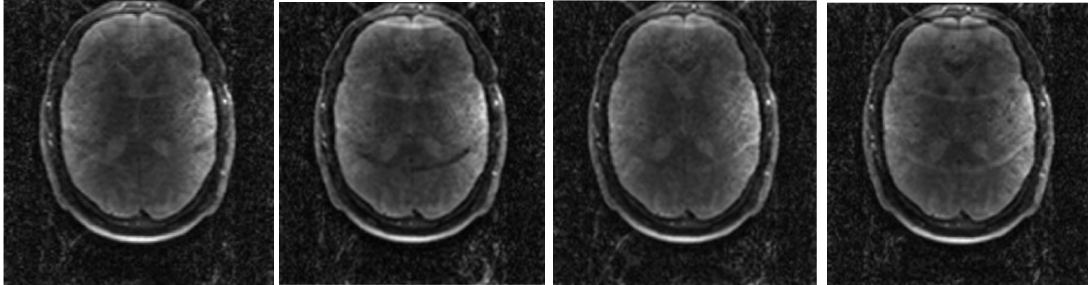


*Figure 3.16. K-space representation of 4 individual shots from a 4-shot acquisition.*





**Figure 3.17.** Image space of each shot from a 4-shot acquisition. All images were matched for  $b=0$  diffusion direction, slice, and channel.



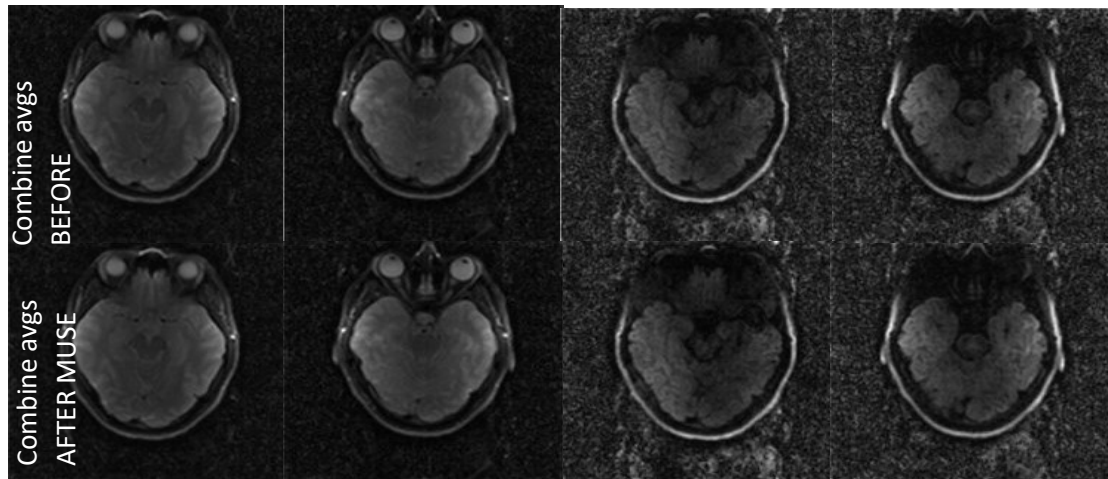
**Figure 3.18.** Estimated full FOV image for each shot from a 4-shot acquisition after SENSE reconstruction. All images are  $b=0$  and slice-matched. Images represent early SENSE reconstruction attempts with acquired 4-shot data. Residual ghosting suggests inaccurate coil sensitivity maps.

Datasets examining the impact of SNR on MUSE reconstruction were explored.

One way to increase SNR is by increasing the number of combined averages, and so early investigations of SENSE varied the number of combined averages and looked at how the output image was impacted. This was done with the understanding that the final version of the pipeline would have combined averages for the initial SENSE, but that this could give insight into how the MUSE algorithm might behave with varying number of averages. As well, it was assumed that the averages were similar, but still needed to be probed whether increasing the number of averages did improve the appearance of the full image.

First, it was tested whether combining averages before or after the MUSE step impacted image quality (Figure 3.19). As expected, there were no noticeable differences in image quality. However, there was residual ghosting after MUSE. To investigate this,

individual averages were examined (Figures 3.20-21). There was noticeable image

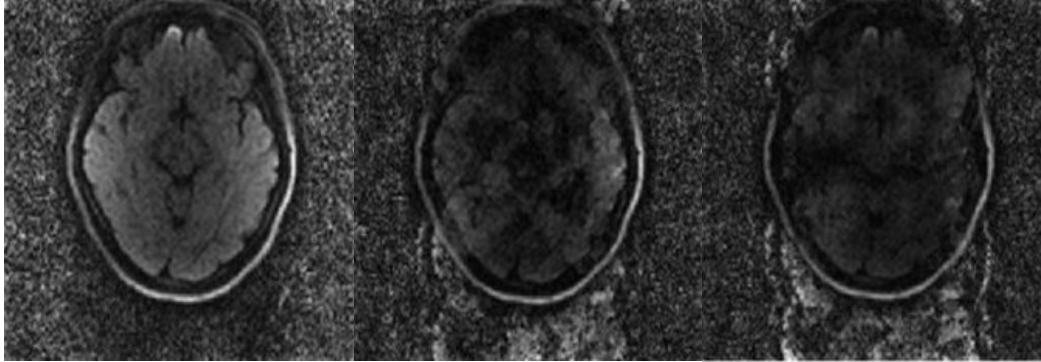


**Figure 3.19.** Image quality comparison when averaging before or after the MUSE step. There were no noticeable changes in image resolution, noise, or anatomical structure whether averages were combined before or after MUSE. Left two columns of images show  $b=0$  images across two slices. Right two columns show  $b=1000$  images across two slices. Slices were matched for combining averages before and after MUSE.

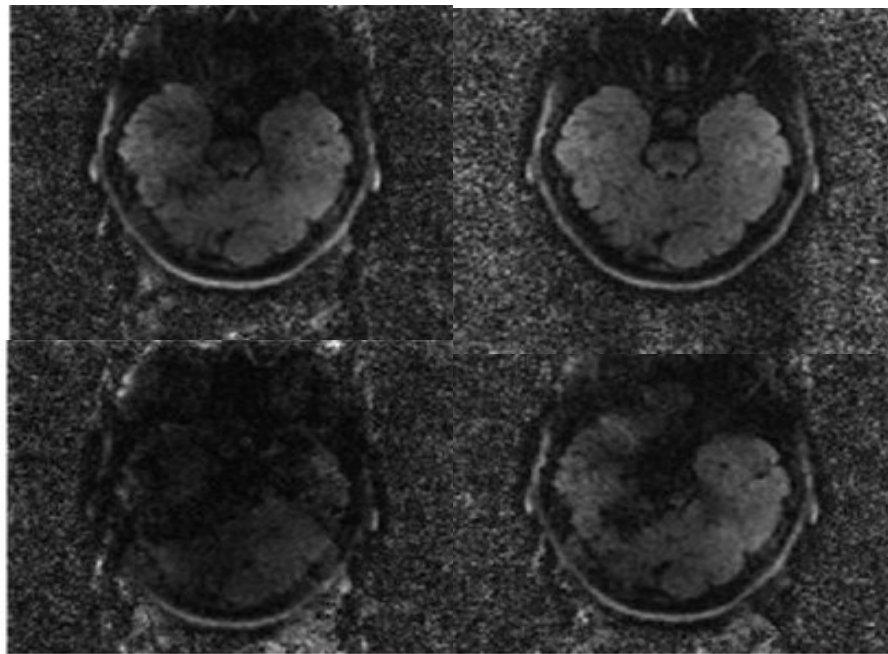
degradation between the individual averages, regardless of diffusion direction. This was not seen in the  $b=0$  images, which looked reasonable across averages. The first average was consistently clearer quality compared to the others for the  $b=1000$  images. This led to an extensive investigation into the trends of averages across slices and acquisitions (Appendix IV). This included probing image quality with different combinations of averages, how SNR changed with different combinations of averages, and how image quality changed after the MUSE step with and without the motion correction.

One hypothesis for the poor image quality seen in some averages after a SENSE reconstruction was that the SNR limit had been reached. This was supported by the observation that the  $b=1000$  images were impacted and not the  $b=0$  images. However, this did not explain why some averages reconstructed well while others did not, and also did not explain why increasing the number of combined averages did not always improve image quality (Figure 3.22). This was rectified with the modifying text file aimed

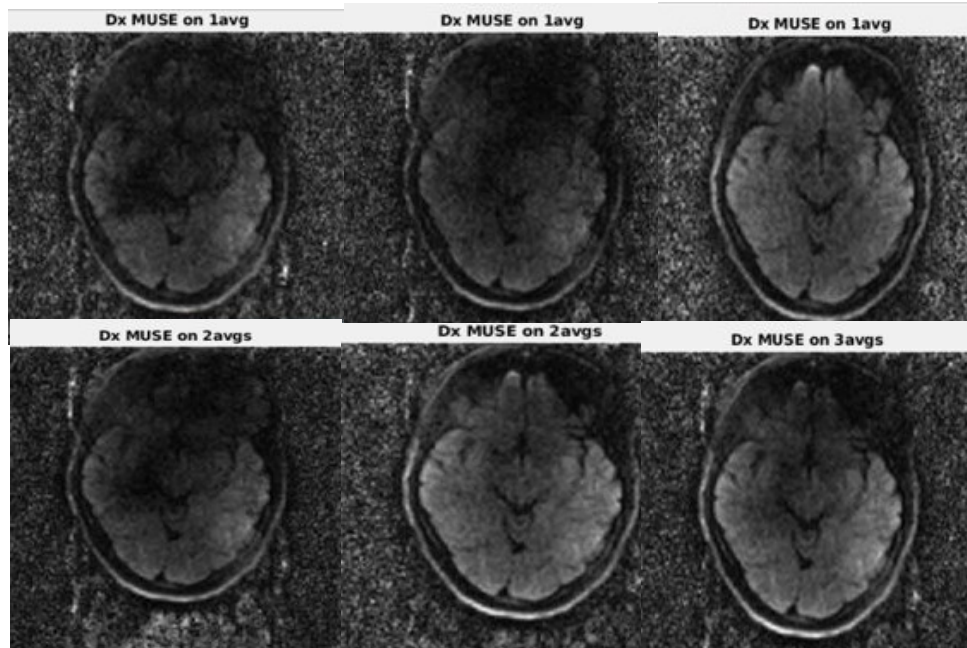
at altering the navigator data (Figure 3.23). At this point, combining the averages and reconstructing with SENSE for full FOV estimations of each shot was acceptable to focus on estimating phase errors.



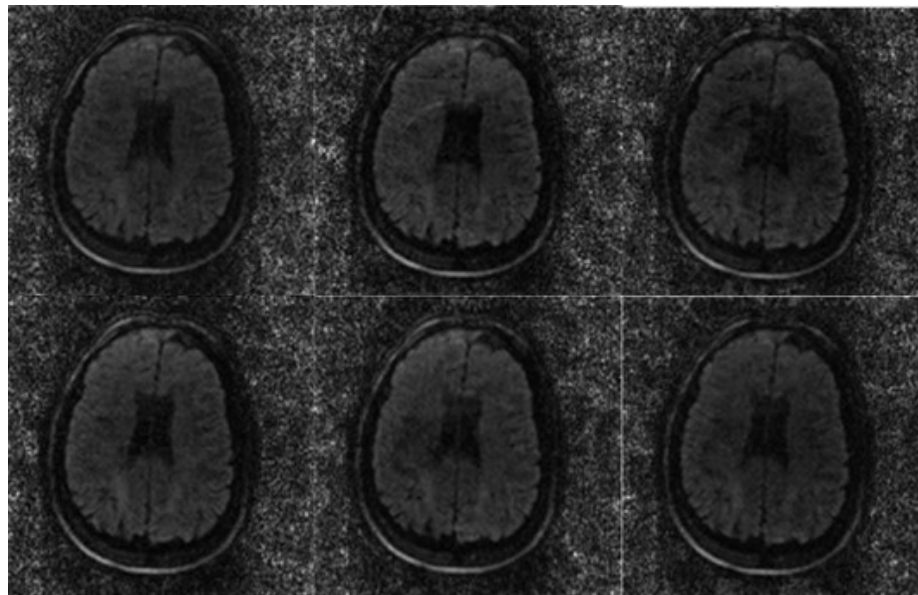
*Figure 3.20. Comparing averages from a three average acquisition in the z-diffusion direction.*



*Figure 3.21. Comparing individual averages in a single slice for a single diffusion direction for quality. Clockwise from top right: collapsed averages, average 1, average 3, average 2.*



**Figure 3.22.** Comparison of individual and combined averages. Top row: Individual averages from a three-average acquisition in the x-diffusion direction. Bottom row: different combinations of averages. From left: combining average 1 and 2, combining averages 2 and 3, all three averages combined.



**Figure 3.23.** Individual averages from a six average acquisition after implementing a modified reconstruction pipeline.

### 3.2.4 Phase Error Estimation Due to Motion

The key feature of MUSE is an estimation of the phase errors due to motion between shots in a multi-shot EPI acquisition. As described in the original MUSE paper<sup>33</sup>, the phase errors can be approximated as

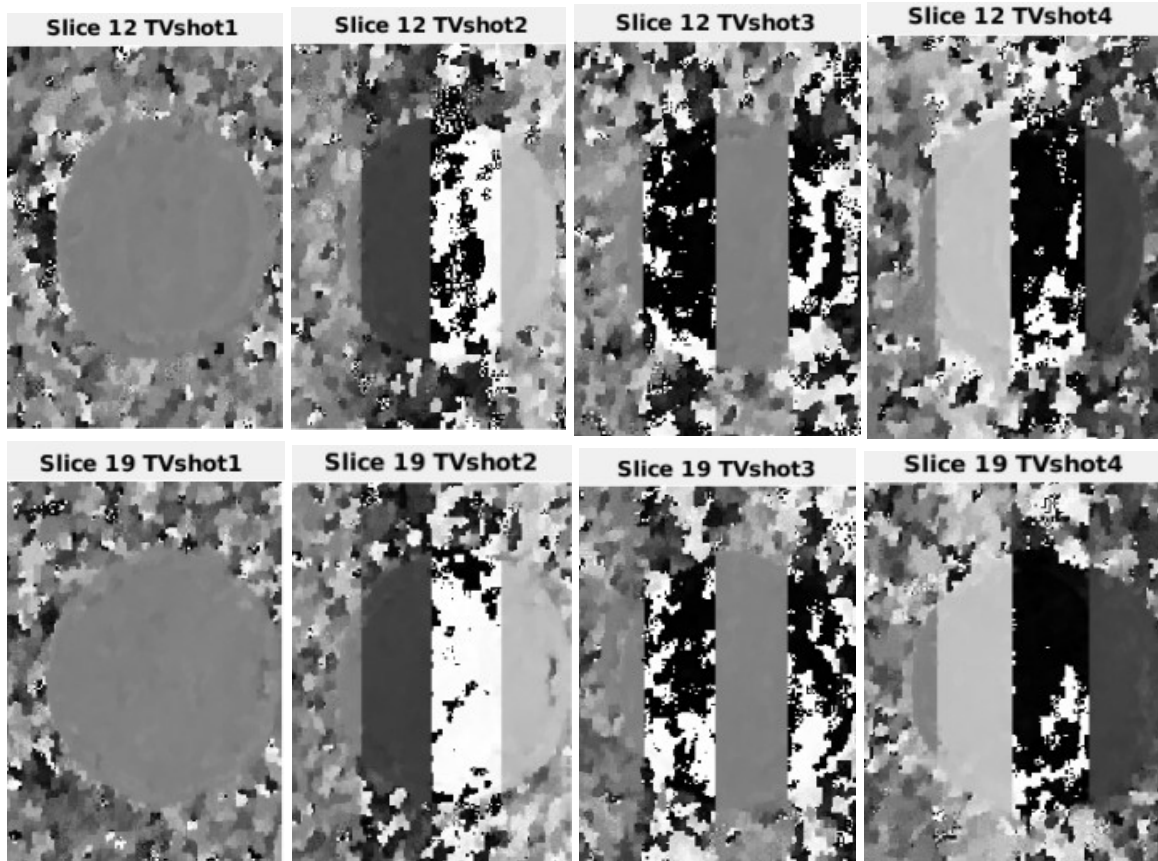
$$e^{i\theta(x,y)+c(x,y)} = \frac{TV(p_s(x,y))}{|TV(p_s(x,y))|}$$

Where  $e^{i\theta(x,y)+c(x,y)}$  describes the phase error for each shot,  $\theta$ , plus the inherent background phase,  $c$ , and TV represents the total variation for each shot. This can be interpreted as the total variation for the full image of each shot divided by the absolute value of the total variation of each shot gives the phase variation. Since the magnitude of each image represents a positive intensity value, dividing by the absolute value sets the magnitude of the image to 1 and leaves a phase map for each shot.

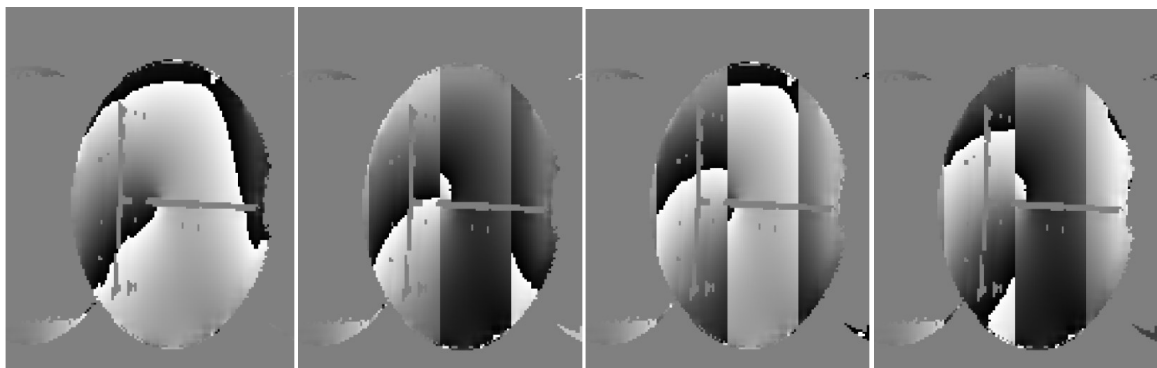
The total variation algorithm selected for this project was a publicly available Matlab algorithm called TV-L1 denoising algorithm<sup>77</sup>. This function simultaneously denoised the image while calculating the total variation, and had options to adjust the regularization coefficient and number of iterations, which allowed for sufficient control on how much denoising was performed on each image. A lower regularization coefficient and an increased number of iterations indicated more rigorous denoising. These variables were re-visited as other denoising methods were added into earlier steps in the pipeline, but were found to be optimized with a regularization coefficient of 1 and 100 iterations and stayed consistent throughout development. The magnitude and imaginary parts for each shot were run through the algorithm separately and then recombined into a complex number. The magnitude of the complex total variance was taken, and then the complex number was divided by the magnitude to produce phase maps (Figure 3.24). A block pattern was observed in the data, where the phase map was divided into the number of shots, and each shot had a unique blocking pattern that



seemed to be consistent across slices. This pattern can be understood by looking at the underlying math describing the phase, and this will be discussed with the development of the 'MUSE off' condition further on.



**Figure 3.24.** Phase maps for a 4-shot acquisition on a phantom in two slices. Each row represents the phase maps for shots 1-4 for a separate slice. TV = total variance.



**Figure 3.25.** Sensitivity maps corrected for motion with the phase maps. Each image represents one shot of a 4-shot acquisition.

The final step to correct for motion was to apply the phase maps to the sensitivity maps (Figure 3.25). This was done by multiplying the shot-specific phase map by the coil sensitivity matrix. By doing so, a corrected sensitivity matrix was created for each shot. The matrices for each shot were concatenated across channels to create a single matrix of coil sensitivities for all shots.

### 3.2.5 MUSE Correction

The MUSE algorithm is described as solving the aliased image for the least squared solution. This is the same logic used previously for SENSE, but instead of estimating the full image from each individual shot, the shots are concatenated together such that the number of images used to solve for the final image is [number of shots \* number of channels]. In terms of the setup in Matlab, this means for the number of shots, the original k-space converted into image space is concatenated into a single matrix across channels. This gives a single matrix with the appearance of having [number of shots] times as many images for each channel. In this way, the corrected sensitivities and raw data are comparable sizes and the Matlab pseudocode can be modified slightly from SENSE to the following:

```
% Loop over the one side of the image
  13 For 1/Ns of y
    % Loop over the entire image
      14 For 1 to the size of x
        15 Pick out the sub-problem sensitivities from the corrected sensitivities
        16 Solve the sub-problem in the least-squares sense
      End
    End
End
```

One way to state the fundamental MUSE algorithm is as

$$f(x, y) = \sum_{r=0}^{Ns} S_j \left( x, y + \frac{r * FOV_y}{Ns} \right) p \left( x, y + \frac{r * FOV_y}{Ns} \right) e^{\frac{i2\pi kr}{Ns}}$$

Where  $S_j$  and  $p$  represent the sensitivities and aliased image, respectively. For each image, the term  $e^{\frac{i2\pi kr}{Ns}}$  reflects the relative k-space trajectory shift as a result of skipping lines of k-space in a multi-shot EPI acquisition. As shown earlier (Figure 3.24), phase images appear to be broken into segments depending on the number of shots. For example, a 4-shot acquisition would appear to be broken into 4 segments. The cause of the apparent abrupt shifts, the boundaries of the segments, can be mathematically modelled by the term  $e^{\frac{i2\pi kr}{Ns}}$  where  $k=shot\ number$  and  $r=segment\ number$ . For example, if we look at shot 2 ( $k=2$ ) in a 4-shot acquisition, the relative trajectory shift for each segment can be described as:

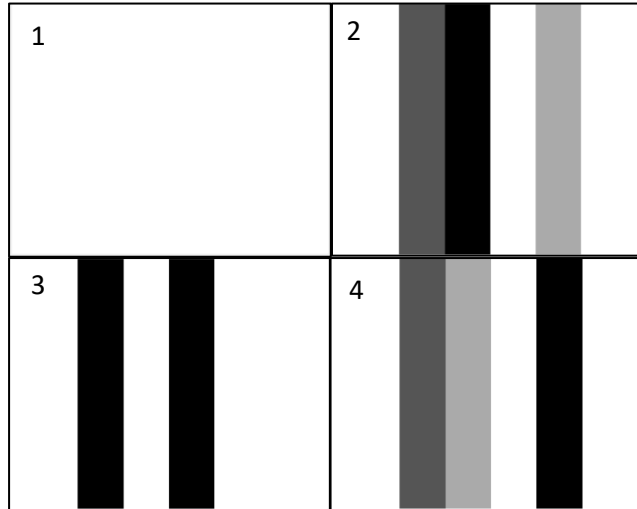
$$r = 0, \quad e^{\frac{i2\pi 2 * 0}{4}} = e^0 = 1$$

$$r = 1, \quad e^{\frac{i2\pi 2 * 1}{4}} = e^{i\pi} = -1$$

$$r = 2, \quad e^{\frac{i2\pi 2 * 2}{4}} = e^{i2\pi} = 1$$

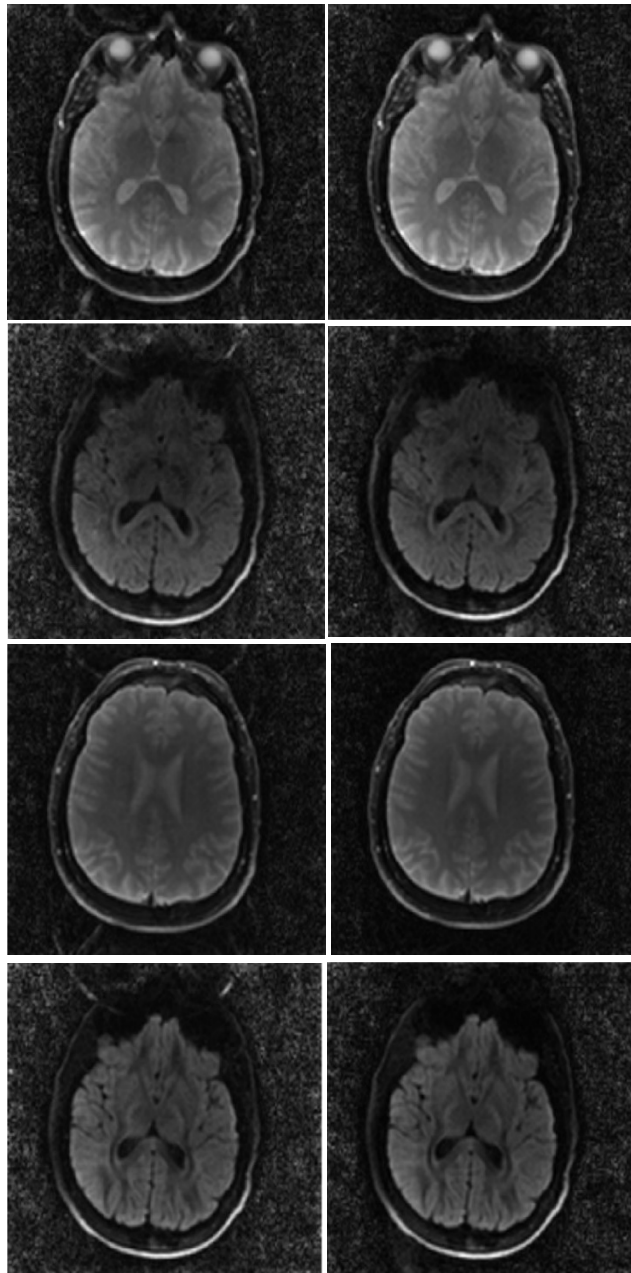
$$r = 3, \quad e^{\frac{i2\pi 2 * 3}{4}} = e^{i3\pi} = -1$$





*Figure 3.26. Modelled k-space phase trajectory shifts for a 4-shot acquisition. The numbers represent the shot numbers from 1-4.*

For a 4-shot acquisition, these can be modelled as shown in Figure 3.26. This was confirmed to be the source of the segmentation by calculating the expected term for each shot and segment, then inverting the sign and applying to the derived phase maps. This largely nulled out the phase, confirming that this phenomenon was the source of the segmentation. As described by the MUSE algorithm, the phase includes the inherent background phase, k-space trajectory shift, and phase shifts due to motion. While the inherent background phase and trajectory shift are expected to be consistent and predictable across datasets, it's including the phase errors due to motion which make the MUSE correction effective. Another way to say this is that all else being equal, the MUSE reconstruction with phase error correction should be the difference between removing ghosting and not.



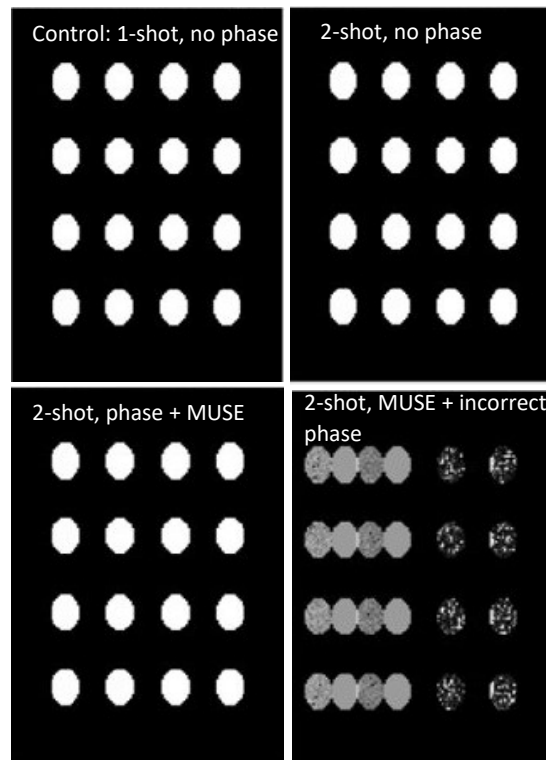
**Figure 3.27.** Comparing MUSE on to MUSE off images for ghosting and image quality. Left column shows  $b=0$  images reconstructed with MUSE correction and right column shows MUSE off. Ghosting can be observed in the MUSE on images as faint, vertical repetitions of the brain. This is reduced in the MUSE off images, suggesting that the phase correction was not being applied correctly.

To test this, a control condition called ‘MUSE off’ was designed. If the phase correction was being applied correctly, the ‘MUSE on’ case should produce less ghosting than the ‘MUSE off’ case. If the phase correction was not being applied correctly, then it

would be expected that having MUSE on or off would not make a difference in ghosting levels.

There was a noticeable discrepancy between MUSE on and off, in which MUSE off images had reduced ghosting levels (Figure 3.27). It was apparent that something in the phase correction was failing, but it was unclear what step was not working correctly. To address this in a controlled manner, a generated phantom was modelled in Matlab using an available phantom generator on the data analysis server. First, the model was used to confirm that the issue was with the phase (Figure 3.28). A generated 1-shot acquisition with derived sensitivities did not impact image integrity. As well, a 1-shot acquisition manually separated into 2 shots with or without added phase did not impact image integrity when reconstructed with the MUSE algorithm. However, if the phase was intentionally uncorrected, the image did not reconstruct properly. This suggested that it was not the TV-L1 phase error correction with the derived sensitivities itself that was the issue, but rather that the phase error correction was not being applied correctly. This helped to narrow down the troubleshooting in the MUSE pipeline. As well, an attempt to identify motion tolerance for MUSE was made by adding artificial movement into the generated model, but it was not deemed a realistic representation of physiological motion, and so focus turned back to the pipeline.

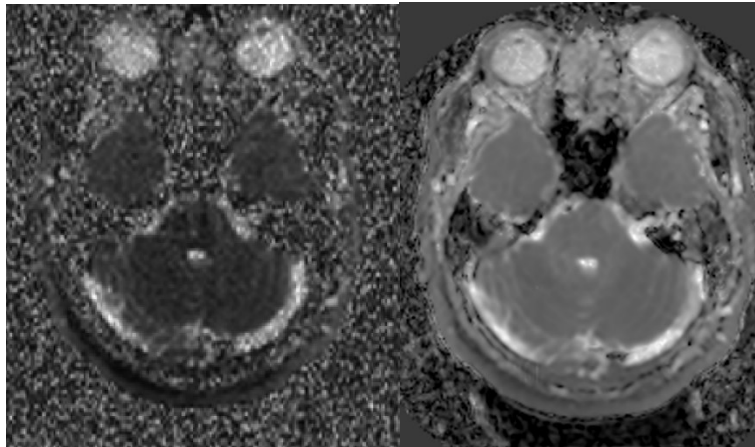
With the problem identified, the correct order of steps to apply the motion correction was confirmed and then applied to the acquired multi-shot data. With the correct sequence of steps, as well as improved derived sensitivities as described previously, the MUSE correction was working at a sufficient level.



**Figure 3.28.** Identifying the source of the MUSE reconstruction issue using a generated phantom model. *Control, 1-shot, no phase:* A control 1-shot with derived sensitivities maintained phantom integrity after going through the MUSE algorithm. *2-shot, no phase:* A 1-shot generated phantom model separated into 2 shots with derived sensitivities concatenated together maintained phantom integrity after MUSE. *2-shot, phase+MUSE:* Adding different phase to each of the shots and applying the TV-L1 derived phase correction maintained image integrity. *2-shot, MUSE + incorrect phase:* 2 shots with different phase and incorrect phase correction did not reconstruct properly.

In addition to individual diffusion images reconstructed with MUSE, it was of interest for clinical application to reconstruct ADC maps. Clinicians use these maps along with the diffusion images to identify cholesteatoma. While not a primary focus for the

project, ADC maps were calculated by  $\frac{\log\left(\frac{b_{1000n}}{b_0}\right)}{b}$  for each diffusion direction, and then the diffusion directions were summed together. From a feasibility standpoint, the ADC maps could be reconstructed with the available SNR (Figure 3.29).



*Figure 3.29. ADC maps reconstructed with MUSE and from the vendor reconstruction. MUSE is shown at left and vendor reconstruction is shown at right.*

Once the MUSE reconstructed images were of an acceptable quality, it was of interest to push the images back to the physician analysis server for ease of comparison with the vendor reconstruction images. Before doing so, some post processing needed to be done to match the images as closely as possible to the vendor standard. First, images were resized. In addition, zero padding of the image was explored so as not to change the shape of the anatomy. However, it was decided that standard interpolation was advantageous since the anatomy was already stretched in Matlab and interpolation was found to correct the stretch to match the shape of the vendor image. Following these steps, the images were written into a DICOM with modified code on the data analysis server<sup>78</sup> and pushed back to the physician analysis server.

### 3.3 Data Analysis

This project was focused on characterizing the changes in ghosting levels with and without the application of MUSE correction. This was analyzed with both visual inspection and characteristic ratio calculations.

#### 3.3.1 Qualitative Analysis

With the correct implementation of MUSE, a reduction in ghosting can be observed by visual inspection. The primary concern with the presence of ghosting in diagnostic images is reducing clinical confidence in decision making. This can be from concerns of artificially bright signal from a ghost overlapping with an existing structure leading to false positives, or reducing confidence in the image integrity simply by the observation of a faint structure that shouldn't be there. This is a critical limiting factor for the potential applicability of this work, and so visual inspection was prioritized, with quantitative analysis being used as a supplementary support of observations. For this purpose, images were presented informally to an otolaryngologist and neuroradiologist familiar with cholesteatoma. They were asked for their opinions on overall image quality and confidence in detection of pathology. They were also asked for input on slice thickness, slice orientation preference, noise levels, ghosting levels, and resolution.

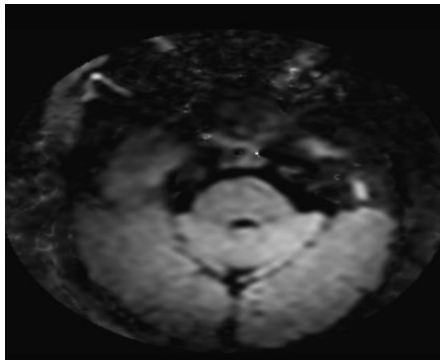
#### 3.3.2 Quantitative Analysis

The purpose of the quantitative analysis was to bolster and support the visual observation of ghosting levels.

For the purpose of this analysis, ghosting was identified as bright regions of signal outside the anatomy resembling the structure of the original anatomy at a displacement  $1/N_s$  away from the anatomy. This is a modified definition of what was used in the

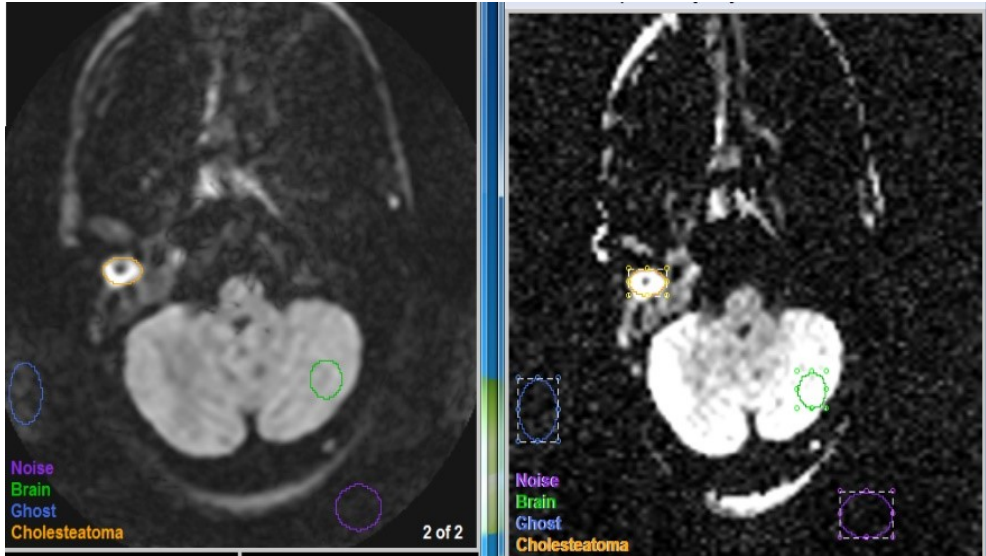
qualitative analysis, which included ghosting inside the anatomy. This distinction was made because ghosting outside the brain was clearly isolated and subject only to interference from background noise level. It was not possible to say with confidence if ghosting inside the brain appeared bright due to strong ghosting or whether it was being artificially amplified by underlying signal. This was easier to evaluate with visual inspection, where the entire image of ghosting and intensities could be observed at once. One caveat of quantifying the ghosting this way was that it may have been impacted by background noise. As mentioned previously, the noise floor was different between the MUSE and vendor images. This may have had an impact on the relative brightness of ghosting from MUSE and vendor images. However, since comparisons were being made within datasets such that noise would be consistent across a given image set, this method was preferred over measuring ghosting inside the anatomy.

Commonly reported values for EPI images are the signal-to-noise ratio (SNR) and ghost-to-noise ratio (GNR). Due to the fundamental differences in noise between the vendor and MUSE reconstruction images, ratios that included noise were avoided. Instead, the ratios used to evaluate the images were ghost-to-signal (GSR) and



*Figure 3.30. Circular cropping in the vendor reconstruction for participant MUSE\_005 hindered accurate ghosting detection.*

distortion-to-signal (DSR). For patient image sets, pathology-to-signal ratio (PSR) and pathology-to-distortion ratio (PDR) were also calculated.



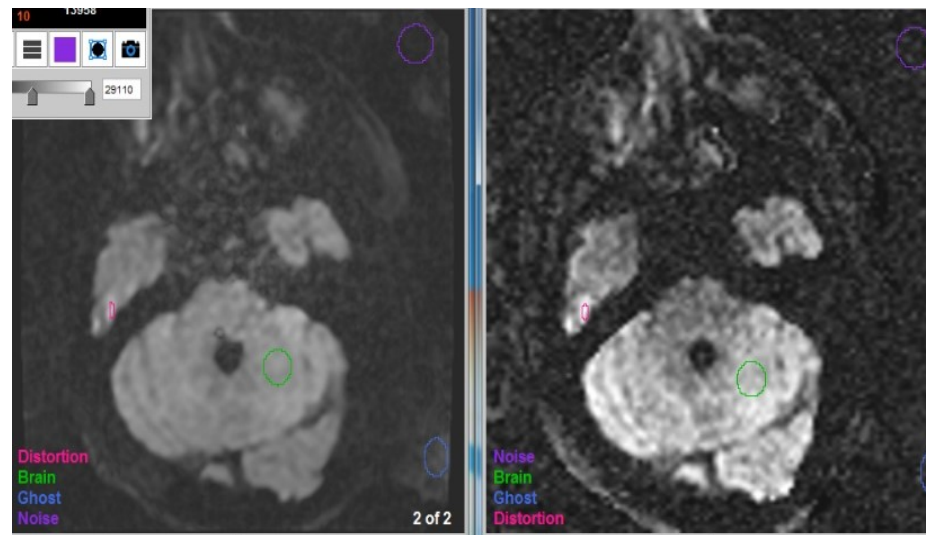
**Figure 3.31.** Representative example of ROIs drawn on a participant dataset with known pathology. Left: vendor recon. Right: MUSE recon. Slices were matched between datasets.

It was of interest to quantify these ratios across 1-shot vendor and MUSE, 1-shot with parallel imaging vendor, 2-shot vendor and MUSE, and 3-shot vendor and MUSE. Note that 1-shot with parallel imaging was collected for interest, but the current MUSE pipeline does not yet support reconstruction of parallel imaging datasets, and so this acquisition is mentioned but not largely discussed here. A consistent acquisition protocol was used for participants MUSE\_006 through MUSE\_009, and so these were the datasets chosen for analysis. Participant MUSE\_005 presented with pathology and so was included to improve the sample size for pathology ratios, but note that at the time of this scan, the protocol was not finalized and so the acquisition parameters varied slightly from the other patient scans (Appendix VII). As well, the participant's auditory canal was not properly centered in the slice stack, and the built-in vendor reconstruction cropped out the majority of the ghosting (Figure 3.32). Ghosting for this



participant was estimated based on the patterns in uncropped images. Participant MUSE\_008 had abnormally high levels of ghosting in their 1-shot acquisition, and so this was dropped as an outlier.

Analysis was done in Mango. Regions of interest (ROIs) were drawn around brain tissue, ghost, distortion, and pathology (Figures III.33-34). Brain tissue was chosen as a consistent area of occipital lobe white matter. Cholesteatoma ROIs, if applicable, were drawn around areas of brightest signal. This often meant choosing a small portion of the pathology rather than the full mass. Distortion was localized to the poles of the



*Figure 3.32. Representative example of ROIs drawn on a healthy volunteer dataset. Slices were matched between vendor (left) and MUSE (right).*

temporal lobe along the auditory canal as well as along the edges of the cerebral tissues following the auditory canal. Similar to pathology, ROIs were chosen for the brightest distortion pixels. Ghosting was chosen outside the brain, most commonly as a ghost of the occipital lobe, since it was the most obvious and consistent. Noise ROIs were collected but not used for analysis. For each dataset, approximately 5 ROIs of each variable were chosen. As much as possible, ROIs were collected in the same slice,

particularly pathology and brain. However in some cases such as distortion, better representations were found in superior or inferior slices, and so the ROIs were collected there. For each acquisition method (1-shot, 2-shot, or 3-shot), ROIs were drawn for each slice in the vendor and MUSE images concurrently to mitigate human error in consistency of ROI selection.

The global and point stats for each ROI in each dataset were exported into Excel for processing. For brain tissue and pathology, the mean signal across the ROI was obtained from the global stats and averaged across slices. For the ghost and distortion ROIs, the maximum signal was obtained from the point stats and averaged across slices. This was done since abnormally bright pixels are the concern for ghosting and distortion, rather than the average signal. The ratios were calculated by dividing the average across slices for each value for each acquisition. This was done in the order of the ratio wording i.e. the ghost-to-signal ratio was calculated by dividing the average ghost maximum signal by the average brain signal for a given acquisition. These values were then transferred into GraphPad Prism for statistical analysis.

The paired t-test was chosen for statistical analysis. This allowed comparison of one acquisition and reconstruction method to another. For each of GSR, DSR, PSR, and PDR, the average mean across participants were compared between 1-shot, 2-shot vendor and MUSE, and 3-shot vendor and MUSE. The paired t-test was chosen because the subjects in each group are not independent of each other<sup>79</sup>. The subjects in each group could be thought of as matched pairs, since the same participants were scanned in each acquisition method.

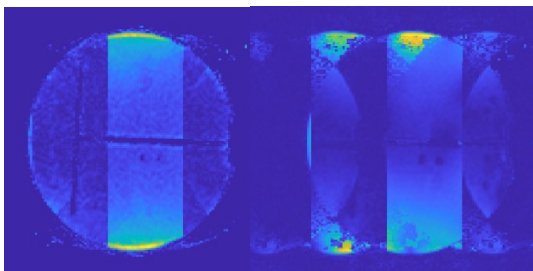
## 4. Results and Discussion

In the current work, the question of whether DW-EPI at 0.5 T provides sufficient SNR to implement MUSE was explored with the development of an offline reconstruction pipeline. This chapter presents and discusses the results that directly test the thesis hypothesis. The primary set of results demonstrates the progressive functionality and optimization of the reconstruction pipeline in phantoms to healthy volunteers and patients. The secondary set of results explores the clinical applicability of cholesteatoma imaging at 0.5 T with MUSE.

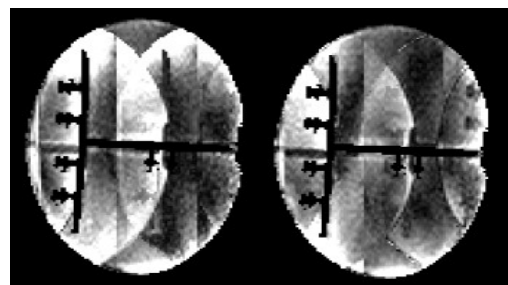
### 4.1 MUSE Reconstruction

#### 4.1.1 Phantom Results

Data was collected on the phantoms as a means of quality control and testing image integrity (Figures 4.1 and 4.2). The measure of progress in the early stages of pipeline development was set as maintaining image quality in phantoms with MUSE compared to the vendor reconstruction. This was to ensure that image quality was not degraded by MUSE, as well as to test sequences before recruiting human participants.

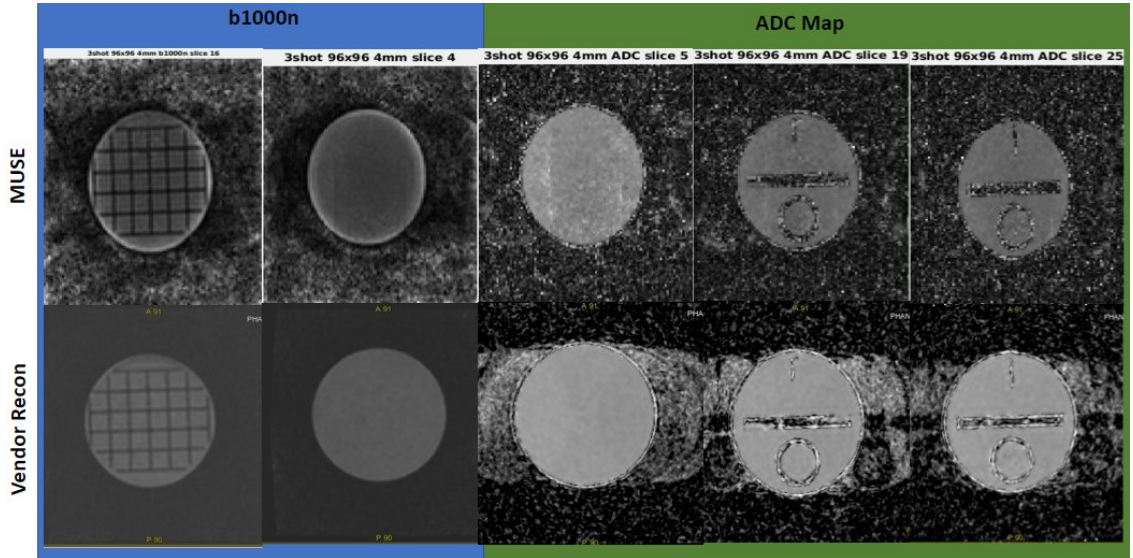


**Figure 4.1.** Examples of the phantom data being used to find issues with the phase correction. Both images were collected with a 4-shot acquisition and clearly demonstrate an issue in the phase correction for at least one segment.

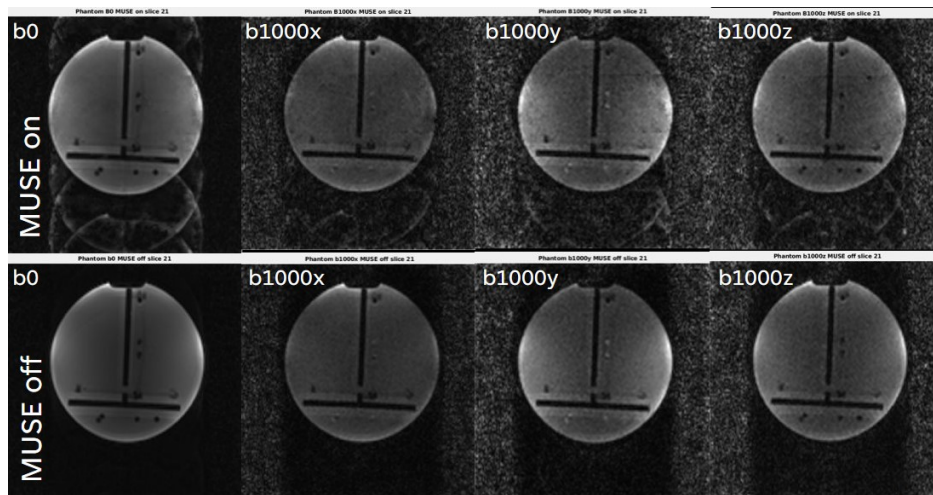


**Figure 4.2.** Phantom data used to develop the MUSE pipeline. Left: MUSE off. Right: MUSE on. The phantom demonstrated that the overall shape was being maintained but that reconstruction was not being performed properly. This was most likely due to improper coil sensitivities leading to poor SENSE estimations.

Once ghosting was sufficiently reduced and image quality was not negatively impacted, phantom data was used to modify the reconstruction pipeline for data collected with the current acquisition protocol. Before acquiring on the first patient, the sequence was run on an ACR phantom (Figure 4.3) and diffusion phantom (Figure 4.4)



**Figure 4.3.** Quality control images produced with the current 3-shot 96x96 protocol with and without MUSE. Top row: images reconstructed with MUSE. Bottom row: vendor reconstruction images. There was minimal ghosting in the vendor diffusion images and significant ghosting in the ADC maps. The MUSE images had minimal ghosting in the diffusion images and qualitatively reduced ghosting in the ADC maps.



**Figure 4.4.** Phantom images reconstructed with and without MUSE across diffusion directions. Residual apparent ghosting remains in the MUSE on images but not in the MUSE off case. This was contradictory to what was found using the same sequence collected on a human volunteer.

and used to modify the pipeline to accommodate 3-shot DW-EPI data as well as to ensure that the MUSE reconstruction would run with the reduced signal.

#### 4.1.2 Phantom Discussion

Pipeline issues were identified by phantom imaging. For example, phantoms were used to illustrate persistent issues with the initial SENSE unaliasing (Figure 4.2). The resulting image had the correct circular phantom shape, but aliasing remained within the object. The Matlab reconstruction introduced a vertical stretch in the object compared to the vendor reconstruction, which was clearly identified by the circular phantom appearing oblong.

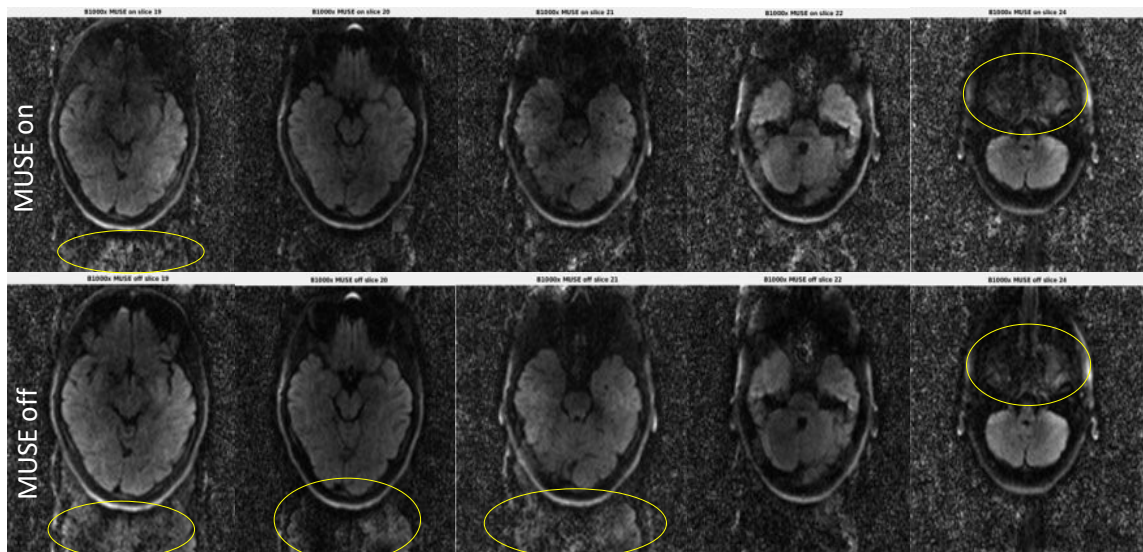
When exploring the phase maps, particularly understanding how the phase varied between segments, the phantom data clearly illustrated issues that needed to be resolved (Figure 4.1). This was advantageous over human data because the phantoms had a known shape with known uniform signal, and it was clear to identify when this was not the case in the reconstruction.

A comparison with the vendor reconstruction between diffusion images and ADC maps with the MUSE and vendor reconstruction showed similar image quality between diffusion images and reduced ghosting in the ADC maps (Figure 4.3). In these MUSE images, the diffusion images in the x, y, and z directions were summed to produce net diffusion images, called  $b=1000n$ . The phantom images illustrated a suspected sign of phase error estimation failure in the form of a vertical line that indicated MUSE was close to its limit, but was not detrimental (Figure 4.3, MUSE  $b=1000n$ ).

However, the use of phantoms was limited. The phantoms by nature have hard boundaries that produce artifacts (Figure 4.4). This gave the false impression that there was an issue with MUSE even when the pipeline was working as expected on brain data. Therefore, once the pipeline had been adequately developed and switched from construction to optimization, brain data was preferred to phantom data.

#### 4.1.3 Healthy Volunteer Results

The MUSE pipeline was considered to be working adequately when i) the anatomy looked comparable to the vendor reconstruction and ii) ghosting was reduced in the MUSE on case compared to the MUSE off and vendor reconstruction. Specifically, the MUSE pipeline was considered sufficient when ghost reduction was seen in both the  $b=0$  (no diffusion) and  $b=1000$  (applied diffusion gradient) MUSE on images compared to MUSE off (Figure 4.5).

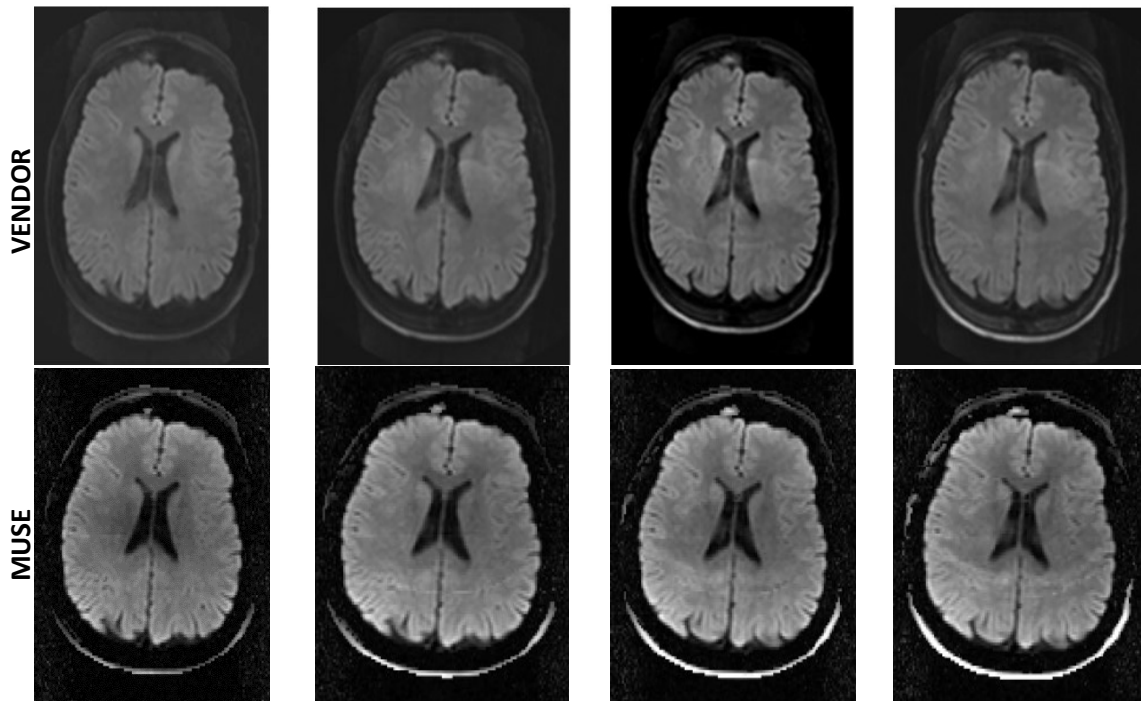


**Figure 4.5.** Proof of concept of reduced ghosting with MUSE. Yellow circles indicate ghosting. Top row: MUSE on shows reduced ghosting outside the brain, while some ghosting of the occipital lobe remains in the most caudal slice (far right). Bottom row: MUSE off shows significant ghosting outside the brain.

Repeatability was tested with a quality control scan where four repetitions of the same acquisition sequence were performed one after another on the same person



(Figure 4.6). A slice with clear ghosting of the skull was selected and matched across repeated trials.



*Figure 4.6. Four repetitions of consecutive, identical 4-shot acquisition in a single patient. Top row: Vendor reconstructed images; Bottom row: MUSE reconstructed images.*

#### 4.1.4 Healthy Volunteers Discussion

Ghosting reduction as a result of MUSE reconstruction was demonstrated in Figure 4.5. Some residual ghosting was observed in the MUSE on condition for some slices, but it was qualitatively reduced compared to the MUSE off case.

Healthy human brain images demonstrate the applicability of MUSE at 0.5 T to human applications, but also expose opportunities for improvement. In the proof of concept in Figure 4.5, MUSE is reducing the overall ghost artifact. However, the algorithm was not completely correct, since residual ghosting remained. This led to further work investigating coil sensitivity map accuracy, as described previously. Human datasets also highlighted the need to center the image in the FOV, and demonstrated

the need to switch the frequency encode direction so that the antialiasing filter could be applied in the direction most likely to incur wraparound. This was demonstrated in Figure 4.5, where the nose is seen to wrap around from the image top to bottom. The frequency encode direction was switched into the anterior-posterior direction to address this, as previously discussed.

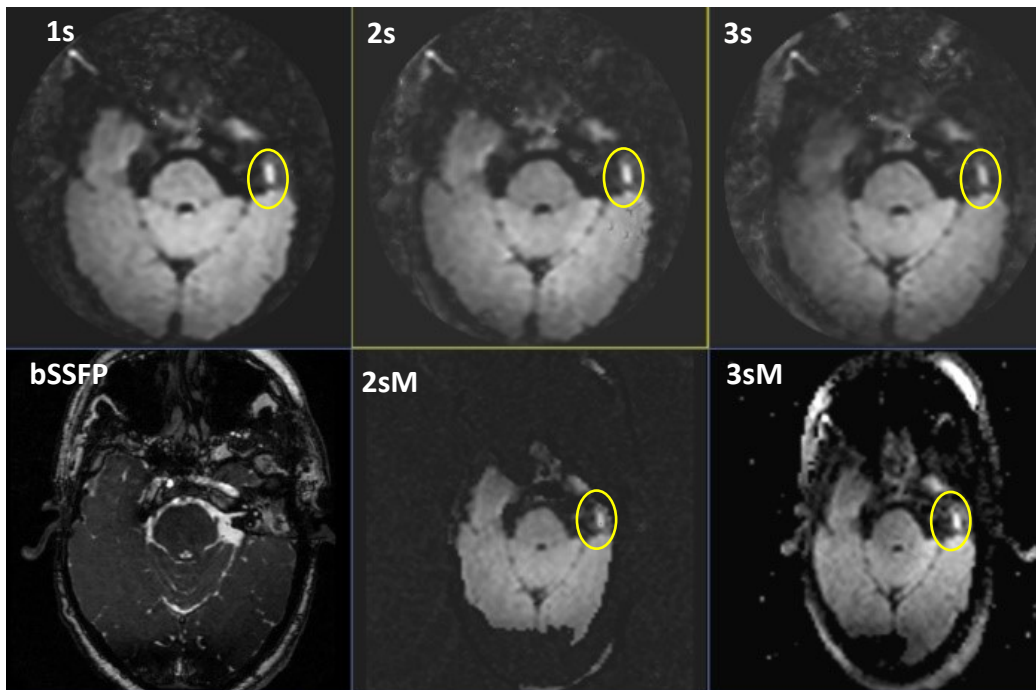
The repeated trials investigation was performed to test the consistency of the MUSE reconstruction. In Figure 4.6, subtle differences arising from patient motion across trials are visible in the amount of residual ghosting in both the MUSE and vendor reconstructed images. The MUSE images consistently maintain image integrity and do not worsen ghosting levels compared to the vendor reconstructed images. Some residual ghosting of the skull remains in the MUSE images in some trials, but ghosting outside the skull is consistently reduced in the MUSE images compared to the vendor reconstruction.

#### 4.1.5 Patient and Quality Control Volunteer Results: Qualitative Comparison

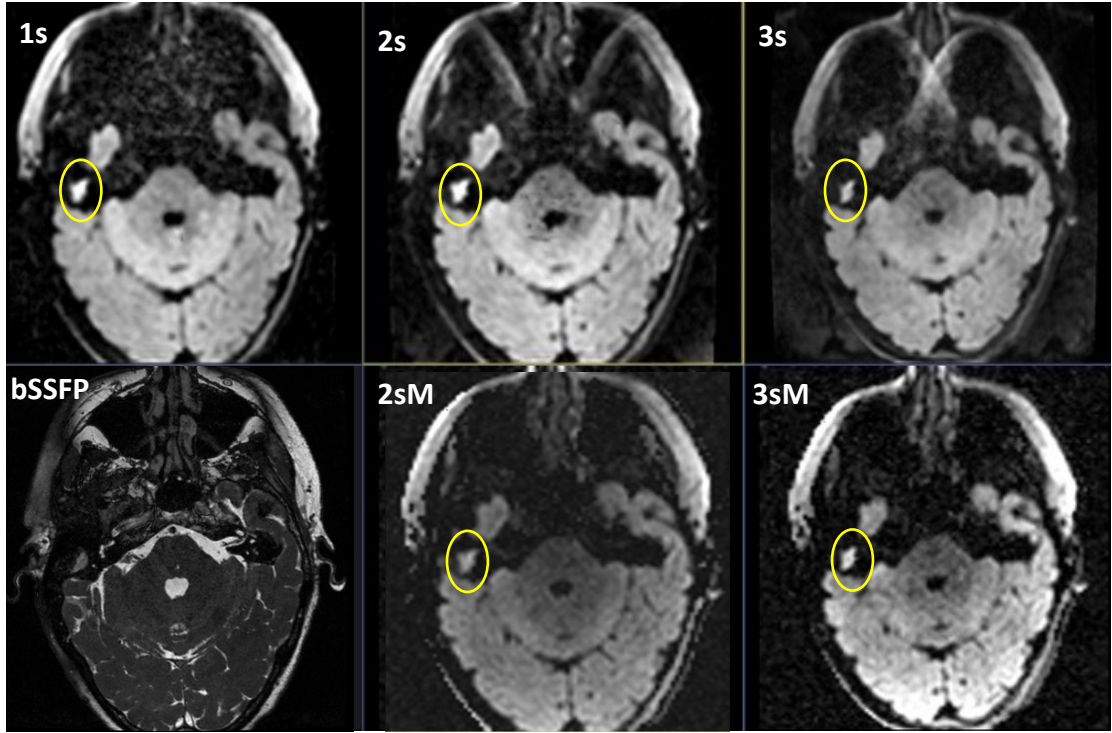
In Chapter 3.2.8, a consistent protocol was developed and used to scan four patients with a diagnosed cholesteatoma and two healthy volunteers. Each participant was scanned with an anatomical bSSFP, 1-shot DW-EPI with parallel imaging, 2-shot DW-EPI, and 3-shot DW-EPI. The results for each individual participant are presented and discussed in Figures IV.7-11. For each image set, the images are presented as top row of vendor 1-shot DW-EPI with parallel imaging (1s), 2-shot DW-EPI (2s), and 3-shot DW-EPI vendor (3s). The bottom row of each has the anatomical bSSFP, 2-shot DW-EPI with MUSE (2sM) and 3-shot DW-EPI with MUSE (3sM). The participants are referred to by



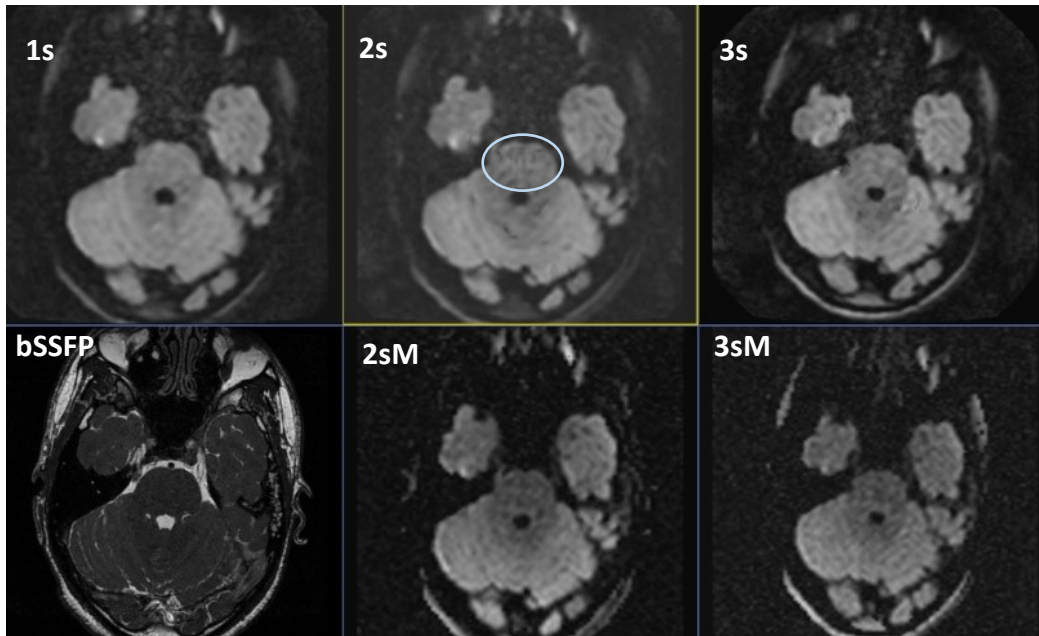
their study ID, and the associated number represents the order in which they were recruited to the MUSE study overall. For example, Figure 4.7 shows the images of participant MUSE\_005. This participant was the first of the patients, but fifth overall to be recruited for the MUSE project, after the healthy volunteers.



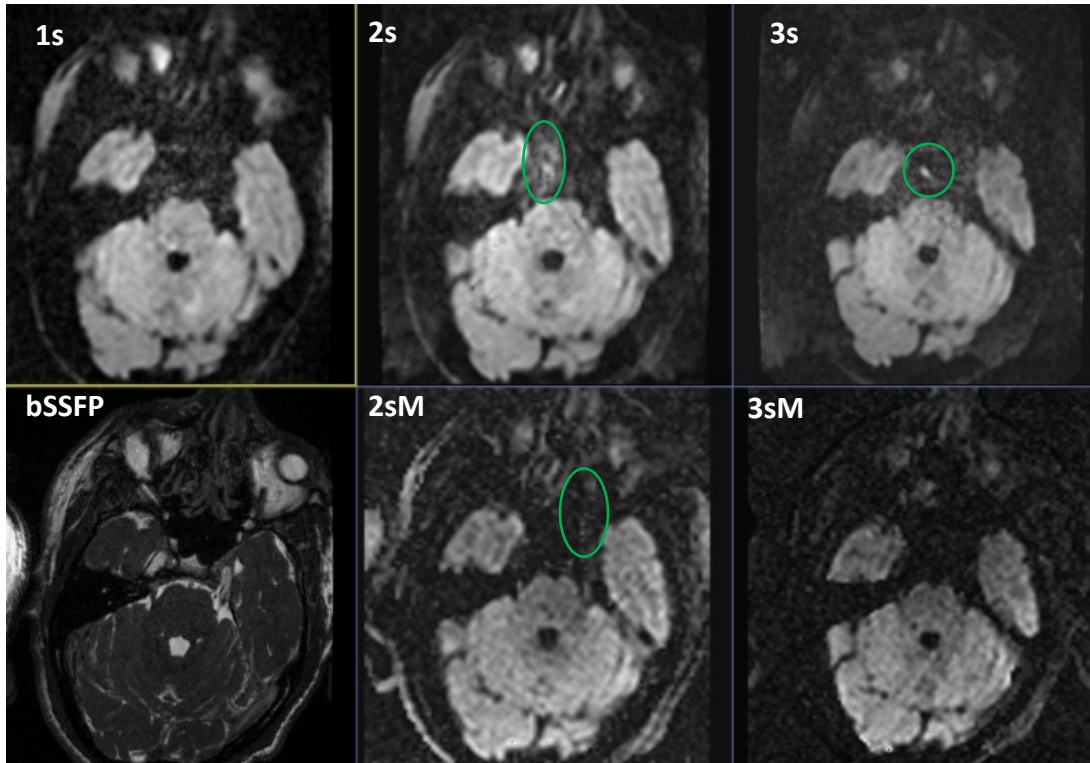
**Figure 4.7.** Volunteer MUSE\_005 with a diagnosed cholesteatoma. Imperfect centering led to the anatomy of interest being on the end of the slice stack and resulted in severe circular cropping with vendor reconstruction images from physician analysis server. Ghosting is therefore difficult to identify. Cholesteatoma is circled in yellow. 3-shot MUSE sensitivity maps could not be filtered properly, leading to pinpoint noise in resulting image. Distortion is visually similar across number of shots. This patient had undergone previous surgery for cholesteatoma in the other ear and was being treated for a new occurrence. Physician experts noted that they did not see signal from the previous surgical site, suggesting that the surgical material used did not present brightly in DW-EPI at 0.5 T.



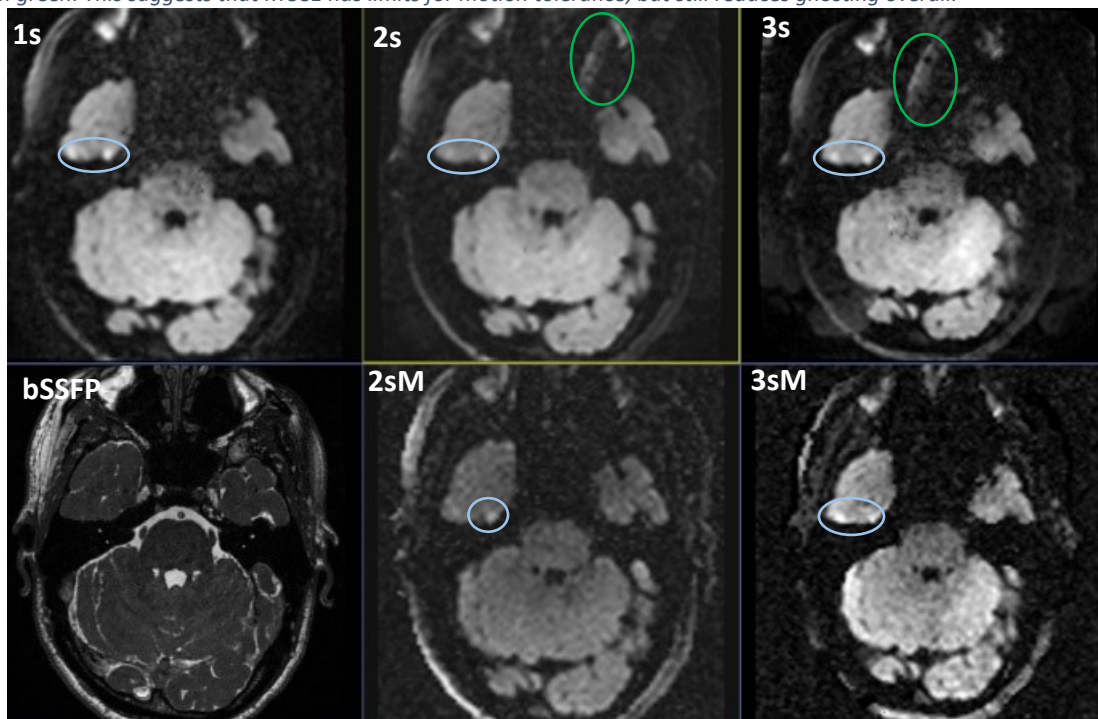
**Figure 4.8.** Patient diagnosed with a large cholesteatoma (MUSE\_006). The cholesteatoma (circled in yellow) spanned across multiple slices, and so the best representation in the middle was chosen. The pathology is clearly visualized in each acquisition. The 2-shot and 3-shot vendor (2s and 3s) have clear skull ghosting across the nose. This is cleaned up in both 2-shot MUSE (2sM) and 3-shot MUSE (3sM). Both MUSE images have some skull degradation due to denoising attempts that do not interfere with identifying the pathology.



**Figure 4.9.** Patient with a suspected cholesteatoma and a suspicious fluid mass across acquisitions (MUSE\_007). The cholesteatoma (not visible in this slice) was identified across acquisition methods. This dataset was difficult to balance for the denoising parameters, which led to a compromise of reduced noise but at the cost of degrading some of the skull. Skull degradation had been discussed previously with physicians and was less of an issue than obvious noise. This patient had little motion and ghosting but some phase incoherence, circled here in blue, which was cleaned up with MUSE.



**Figure 4.10.** Healthy volunteer (MUSE\_008) acquired with the cholesteatoma protocol. This volunteer's head filled the FOV and was off-centre, leading to wraparound in the left-right direction that did not interfere with visualizing the auditory canal. Significant ghosting was visible with the 2- and 3-shot acquisition. This was largely rectified with MUSE, but some residual ghosting may have been left around the nose and eyes, as circled in green. This suggests that MUSE has limits for motion tolerance, but still reduces ghosting overall.



**Figure 4.11.** Healthy volunteer MUSE\_009 across acquisition methods. This slice clearly demonstrates  $1/N_s$  ghosting of the skull (circled in green) that is removed with MUSE, as well as clear distortion manifesting as bright signal along the temporal lobe (circled in blue).

#### 4.1.6 Patient and Quality Control Volunteer Discussion: Qualitative Comparison

Each image set was analyzed for overall image quality and visible ghosting levels.

A specific discussion accompanied each figure, but some overall trends were observed.

For each patient and healthy volunteer presented, MUSE consistently reduced ghosting.

In healthy volunteer MUSE\_008, excess motion led to severe ghosting, and some faint signal in the MUSE images may have been residual ghosting that the pipeline could not

fully remove. However, ghosting was still reduced in this case. This suggests that the

MUSE pipeline may have a limit of how much motion it can tolerate before the

algorithm fails. This is unsurprising, as intentional motion in the generated phantom had

similar results where reconstruction began to fail if simulated motion between shots

was added in. The overall appearance of the anatomy between vendor and MUSE

reconstruction is generally consistent. However, there was a right-left compression and

anterior-posterior stretch in some MUSE images. This is most likely a result of improper

slice centering and lack of the vendor post-processing in the MUSE pipeline. As well,

some of the MUSE images had skull degradation. This was a direct result of noise

filtering in the sensitivity map step. For each dataset, the optimal combination of

sensitivity map filtering to remove noise while maintaining image quality was selected.

This issue of skull degradation was discussed with physician collaborators. They

indicated that this was not a concern, as long as the anatomy of interest (i.e. the

auditory canal and surrounding region) were intact.

In terms of the hypothesis, these results support that DW-EPI at 0.5 T produces sufficient signal to perform MUSE.

#### 4.1.7 Patient and Quality Control Volunteer Results: GSR

Four ratios were calculated to quantify the relative signal intensity changes across number of shots with and without MUSE. The ghost-to-signal ratio (GSR) directly tests the hypothesis and so will be addressed in this section.

A comparison of GSR across number of shots with and without MUSE is presented as a box-and-whisker plot in Figure 4.12.

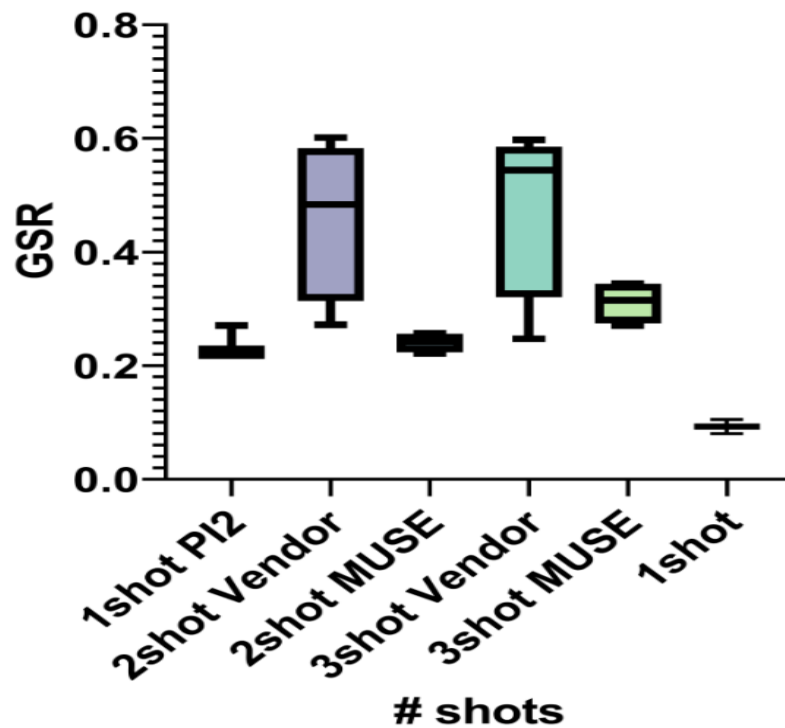


Figure 4.12. Box and whisker plot comparing mean GSR across number of shots with and without MUSE. PI2 = Parallel imaging factor of 2.

The numerical values from the paired t-test comparing mean GSR across number of shots with and without MUSE are presented in Table IV.1.



**Table 4.1.** Paired t-test analysis of ghost-to-signal (GSR) datasets across number of shots and reconstruction methods. Coloured cells indicate support of expected trends. The 2-shot vendor and MUSE reconstructions had statistically different means for GSR (p-value = 0.049, red cell). The 1-shot with and without parallel imaging compared to 2-shot and 3-shot MUSE had statistically not different means (green cells). The 3-shot vendor and MUSE images had statistically not different means.

GSR	p-value	Mean 1	Mean 2	Diff	SE of diff
2-shot Vendor vs MUSE	0.049	0.46	0.24	0.22	0.069
3-shot Vendor vs MUSE	0.098	0.48	0.31	0.17	0.072
1-s PI2 vs 2shot MUSE	0.920	0.24	0.24	0.0029	0.025
1shot vs 2shot MUSE	0.079	0.093	0.23	0.13	0.016
1-s PI2 vs 3-shot MUSE	0.18	0.24	0.32	0.081	0.040
1shot vs 3shot MUSE	0.14	0.093	0.31	0.21	0.049

#### 4.1.8 Patient and Quality Control Volunteer Discussion: GSR

The GSR is a measure of ghosting reduction compared to average signal intensity. GSR was chosen over SNR because noise handling varied between the vendor and MUSE reconstructions, and so using signal as a baseline circumvented the issue of noise handling.

The acquisition protocol set used to acquire the data had a 1-shot scan with PI. This scan was expected to have a comparable readout window length time, and therefore distortion reduction, of a 2-shot acquisition, but without ghosting, since instead of collecting the data in two shots, every other line is not collected. For interest's sake, two 1-shot datasets without parallel imaging from the earliest volunteers (MUSE\_001 and MUSE\_002) were also included in the analysis.

From Figure 4.12, the GSR for the 2- and 3-shot vendor images is visibly higher with a greater spread than the 1-shot with and without PI, 2-shot MUSE, and 3-shot MUSE. This is supported by the statistics. From Table 4.1, the 2-shot vendor and 2-shot MUSE had statistically different means for GSR (p-value 0.049, Table 4-red cell). As well, the 1-shot with and without parallel imaging had statistically unsimilar means (Table 4.1, green cells). This suggests that not only was the mean of the GSR for the 2-shot vendor statistically different and higher than the 2-shot MUSE GSR, the 2- and 3-shot MUSE mean GSRs were not statistically different than the 1-shot mean GSRs. This is important because the 1-shot acquisitions were not expected to have ghosting. The 1-shot with PI2 may have displayed residual aliasing from the interpolated data that could be construed as ghosting. This supports the hypothesis that ghosting is reduced with MUSE.

However, it should be noted that the 3-shot vendor and 3-shot MUSE reconstructions did not have statistically different GSR means (0.098). The most likely explanation for this is that the sample size was small (n=5), and the effect of any outlier would be greater.

It should be noted that the ghosting seen here did not directly interfere with the auditory canal. Most observable ghosting happened outside the brain or in the nasal sinus region. The reason this ghosting may still be considered an issue, even though it does not appear to directly impact the anatomy of interest, is that observable ghosting reduces overall clinician confidence in images. That is, seeing, for example, a ghosted skull fragment where there clearly should not be one raises suspicion that there could be other, smaller structures appearing where they should not, such as along the

auditory canal. Or, knowing that some portion of a signal has moved and maybe taken away from the overall strength of the signal could raise questions as to whether a structure should be hyperintense when it appears isointense relative to the surrounding tissue. Both of these concerns were raised in discussion with clinicians as hesitations for using DW-EPI MRI. With the implementation of MUSE, phase errors leading to misplaced signal are rectified, addressing both concerns around signal misplacement.

Overall, the results discussed here support and agree with the qualitative observations in ghosting level changes with MUSE. Taken together, these results confirm the hypothesis that sufficient SNR will be provided by ms-DW-EPI acquired at 0.5 T to perform MUSE and there will be a quantifiable reduction in motion-induced ghosting compared to images reconstructed without MUSE correction.

These results support the further investigation of ms-DW-EPI acquired at 0.5 T for cholesteatoma imaging.

#### 4.2 Application of ms-DW-EPI at 0.5 T for cholesteatoma imaging

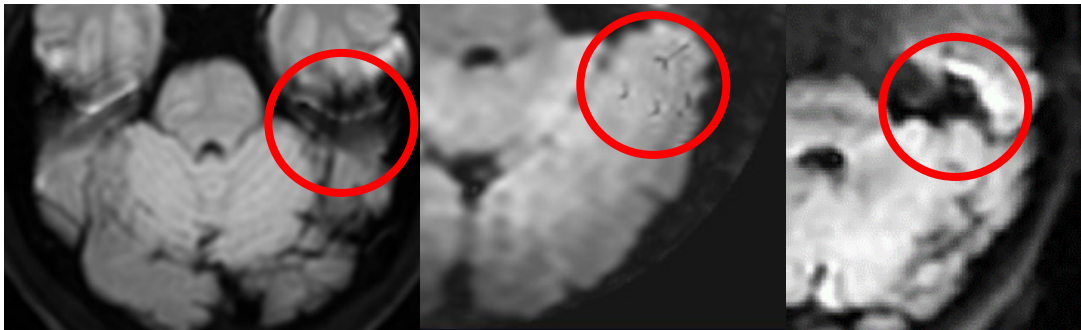
The rationale for using a field strength of 0.5 T in this work was that distortion from SIFG is reduced at lower field strengths. As previously discussed, distortion can result from dephasing in EPI as well as SIFG. These effects are compounded at higher field strengths and at areas of air-bone interfaces. This has been a limiting factor for using DW-EPI with cholesteatoma imaging at clinical field strengths. This section will explore how distortion changes with number of shots in ms-DW-EPI as well as how distortion changes with field strength.



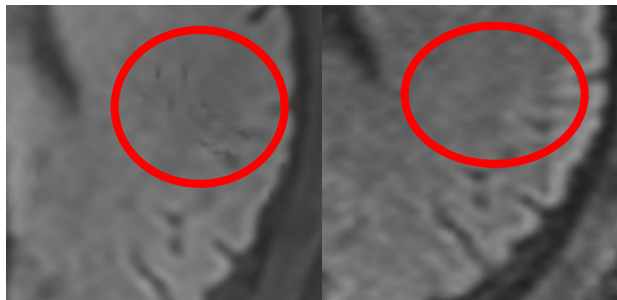
#### 4.2.1 Distortion Characterization

Up to this point, distortion has generally been referred to as signal pile-up causing an artificially bright region. However, three manifestations were observed in this work.

Distortion may result in signal being misplaced onto a region of sparse signal, may cancel out existing signal, or may be misplaced on top of existing signal. Misplaced signal across an area where there should not be any leads to a wisp-like appearance (Figure 4.13).



**Figure 4.13.** Examples of distortion. Left: misplaced signal onto an otherwise void area is circled in red. Middle: circled y-shaped features represent loss of signal resulting from signal misplacement; right: signal pile-up circled in red as a result of misplaced signal amplifying existing signal.



**Figure 4.14.** Misplaced interfering signal removed with MUSE. Left: Vendor recon; Right: MUSE recon.

Phase errors can lead to artificial signal loss (Figures IV.13-14). This issue is corrected with MUSE since MUSE realigns phase.

Finally, signal pile-up resulting from signal misplacement onto areas of existing signal leads to an artificially bright region. While the first two manifestations of distortion are important to recognize to avoid confusion, they do not have the same potential for giving false positives in cholesteatoma detection as the signal pile-up due to distortion. This manifestation of distortion is found along the auditory canal and appears brighter than healthy brain tissue, making it a concern for physicians in using MRI to detect cholesteatoma. Therefore, this was selected as the characteristic to identify distortion in images.

#### 4.2.2 Distortion at 0.5T: Results

The distortion to signal ratio (DSR) across number of shots with and without MUSE was analyzed with paired t-tests and presented in a box-and-whisker plot (Figure 4.15).

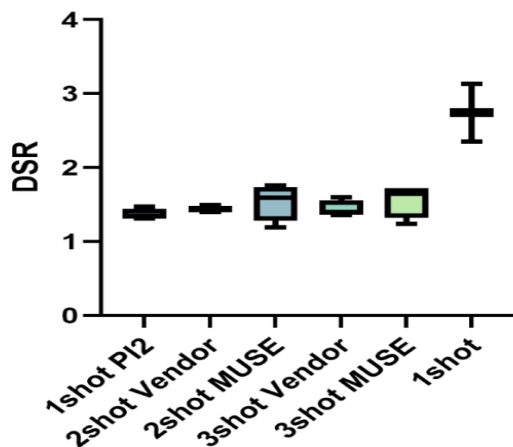


Figure 4.15. Box-and-whisker plot of DSR across number of shots with and without MUSE reconstruction. DSR = distortion-to-signal ratio.

Further, the pathology-to-signal ratio (PSR) and pathology to distortion ratio (PDR) were calculated across number of shots with and without MUSE reconstruction (Figure 4.16).

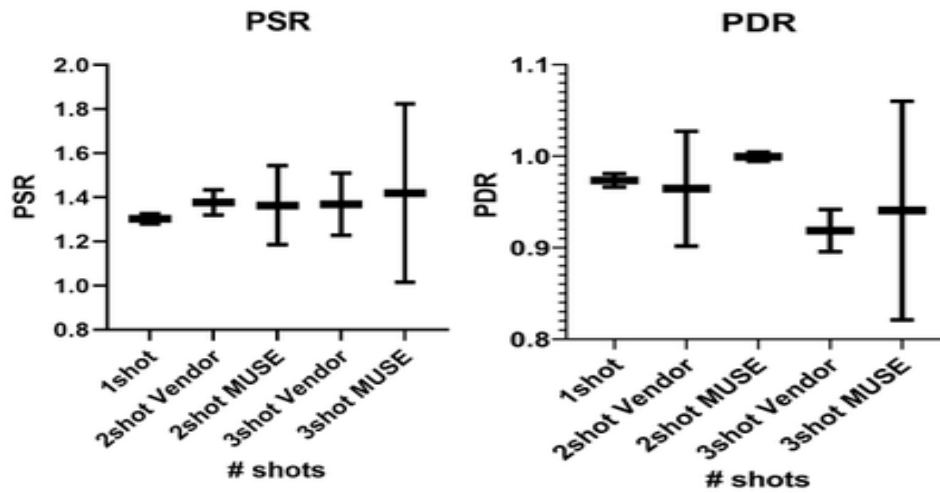


Figure 4.16. Box and whisker plot of paired t-test analysis comparing means between acquisition and reconstruction methods.; PDR = pathology-to-distortion ratio; PSR = pathology-to-signal ratio;

#### 4.2.2 Distortion at 0.5T: Discussion

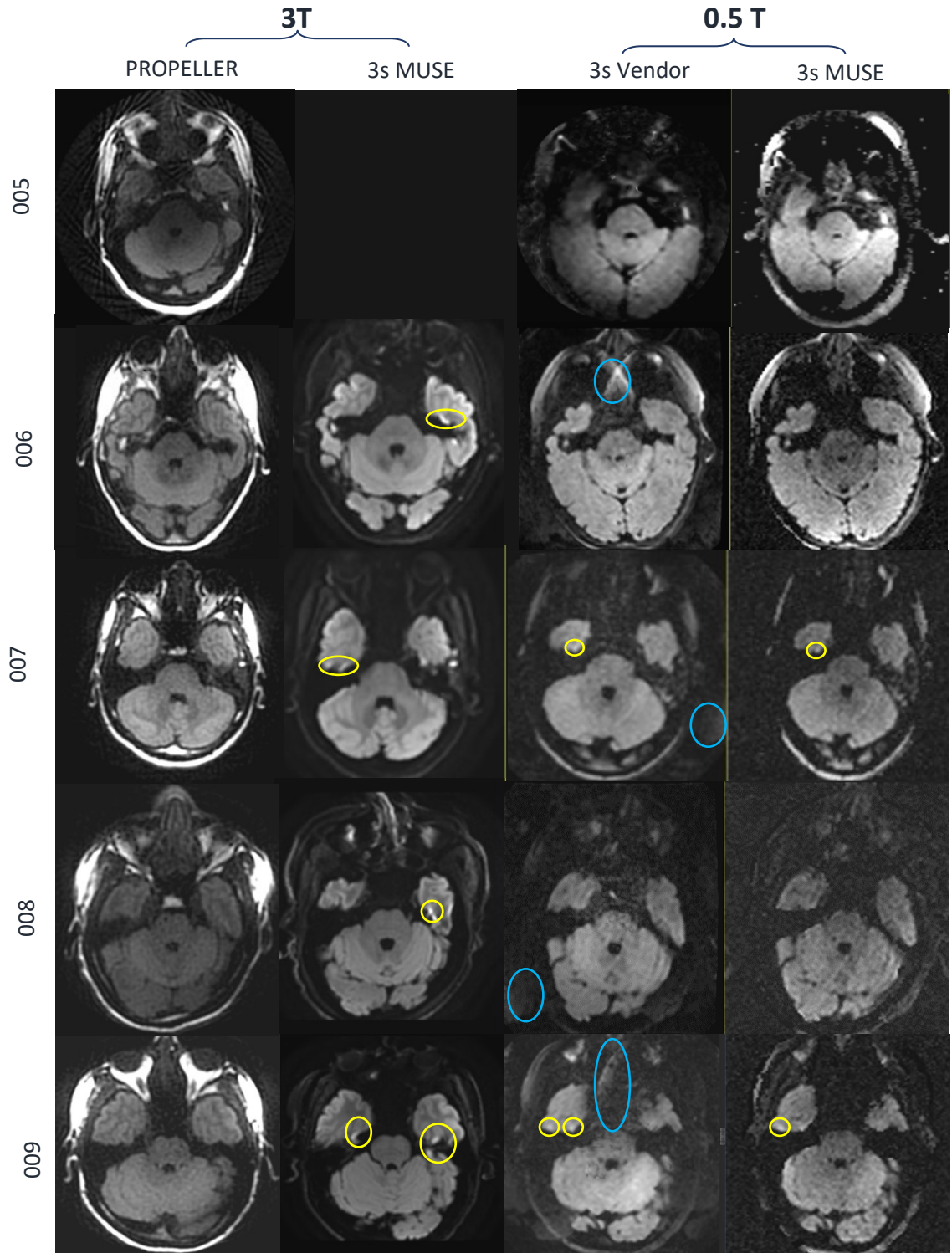
All else being equal, distortion should decrease with an increasing number of shots and MUSE should not change distortion one way or another. Looking at DSR from Figure 4.15, there was a consistency within error across acquisitions with the exception of 1-shot without PI. The spread of means for the MUSE acquisitions was large, and the lowest average DSR was observed in the 1-shot with PI. Looking at the acquisition parameters from the final protocol, the 1-shot with PI2 and 2-shot have a reduced matrix size and FOV compared to the 3-shot. As well, the 1-shot with PI2 should have similar distortion to the 2-shot acquisition. Taken together, this can explain the similar DSR across acquisitions. As expected, the 1-shot data without PI had significantly higher DSR than the other acquisition types. This can be explained by the 1-shot having a longer readout window length compared to 1-shot with PI or multi-shot sequences.

For the purpose of cholesteatoma imaging, it is of interest to reduce distortion levels to below cholesteatoma signal intensity. As well, it is of interest to have pathology

signal intensity above cortical tissue signal intensity. It was demonstrated in Figure 4.16 that the pathology signal intensity was consistently above cortical tissue signal intensity across number of shots with and without MUSE, as indicated by PSR above 1. The pathology, however, was consistently below distortion levels as indicated by PDR below 1. This leaves room for improvement in protocolling to further decrease distortion. It should be noted that the slices chosen to analyze distortion were rarely the same slices as those with cholesteatoma. In these image sets, the most significant distortion was found in superior slices. The practical impact that this distortion has on cholesteatoma diagnosis would need to be discussed with physicians.

#### 4.2.3 Distortion at 0.5 T and 3 T: Results

To explore the impact of field strength on distortion, patients and healthy volunteers were scanned at 3 T with PROPELLER, the current standard for cholesteatoma imaging, and a 3-shot DW-EPI with parameters matched to the final protocol within reason. Patient MUSE\_005 had undergone clinical scanning prior to the study and did not have a comparable 3 T scan with MUSE. These image sets were compared with the standardized 3-shot DW-EPI acquisition at 0.5 T (Figure 4.17). Within reason between participants and field strengths, slices and contrast through window and level were matched. The images were compared for overall anatomical appearance (head shape, feature warping) and distortion. For further support of MUSE at 0.5 T, ghosting levels were also compared.



**Figure 4.17.** Visual comparison of ghosting and distortion across field strengths and acquisitions. Patient 005 had undergone previous clinical scanning without 3-shot MUSE at 3T, and so a comparison was unavailable. Signal pile-up due to distortion is circled in yellow and ghosting is circled in blue. Slices were matched for a given participant across acquisitions within reason but were subject to tilt.

#### 4.2.4 Distortion at 0.5 T and 3 T: Discussion

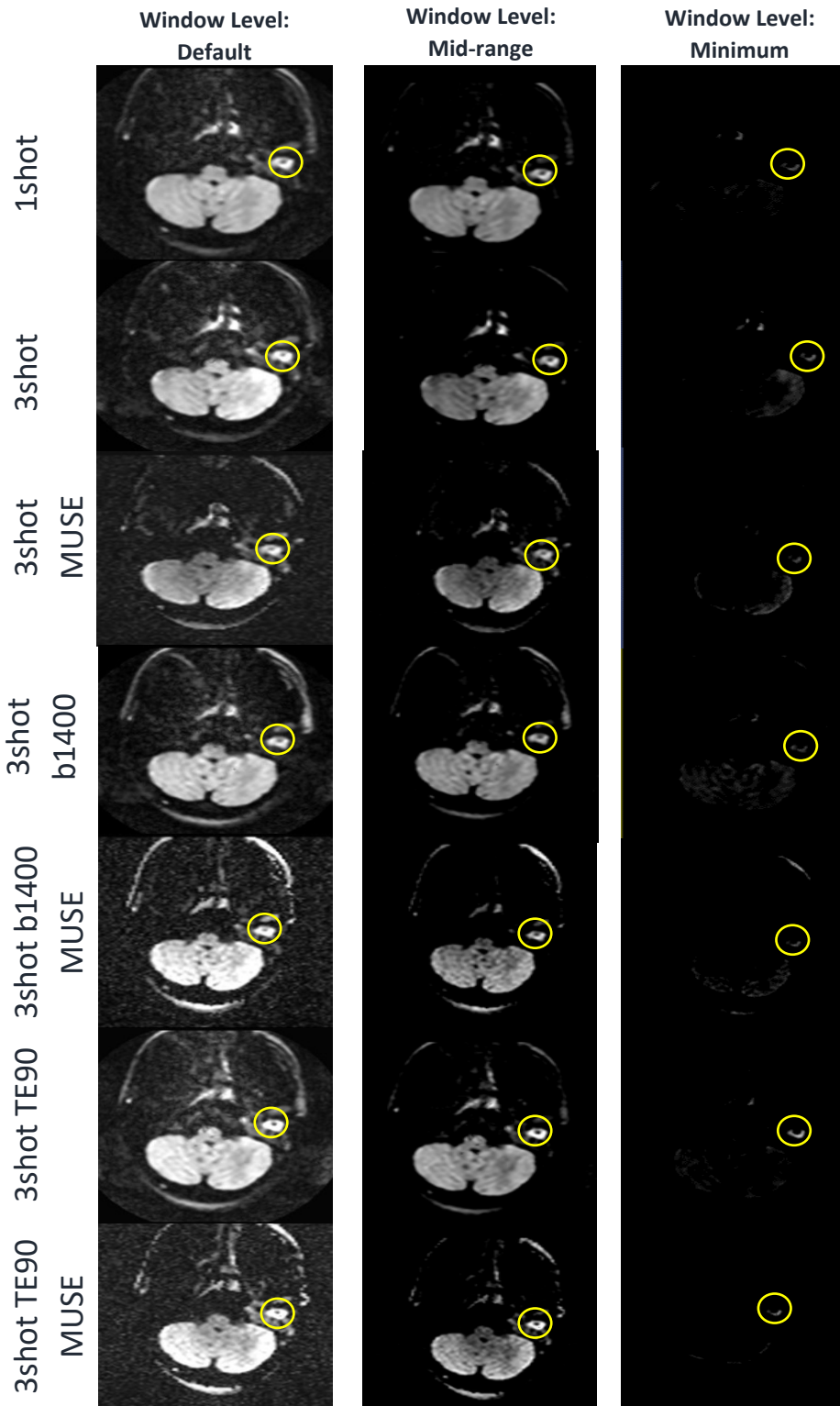
Signal pile-up due to distortion was observed in every participant with MUSE at 3 T, while only visible in two participants at 0.5 T. The standard PROPELLER did not have an observable distortion-induced signal pile-up, but there was a stoke-like artifact in patient MUSE\_005. Ghosting was not present in the PROPELLER images and removed in the 0.5 T MUSE images. In the 0.5 T vendor images, the ghosting was quite prominent. In the 3 T MUSE images, there is no visible ghosting. However, in MUSE\_008, there appeared to be warping in the nose and skull that is not observable in any other acquisition for that participant. This suggests that MUSE at 3 T could be interfering with the integrity of the images in some patients. Taken together, these results suggest that MUSE with DW-EPI at 0.5 T does not reduce image quality compared to PROPELLER, with the exception of the skull degradation resulting from incomplete noise handling. This supported the further investigation of DW-EPI at 0.5 T for cholesteatoma imaging.

#### 4.2.5 Optimizing b-value and TE for cholesteatoma contrast: Results

Physician collaborator preference for cholesteatoma detection is to be able to lower the window and level such that cholesteatoma is the brightest feature in the image. For this to happen, several requirements must be met. Signal pile-up due to distortion must be reduced to a level below cholesteatoma, but preferably similar to cortical tissue. Ghosting causing artificially bright signal must be mitigated to prevent false positives. Additionally, cholesteatoma tissue contrast compared to cortical tissue must be optimized. From Figure 4.16, the current protocol has relatively constant PSR across number of shots with and without MUSE. This sits between 1.3 and 1.4, which

does indicate that pathology is brighter than signal. However, the PDR is around or below 1 for each acquisition, suggesting that pathology is not brighter than distortion.

In the literature, cholesteatoma contrast is attributed to diffusion restriction and/or T2 shine-through<sup>4,17</sup>. To explore optimal contrast, one patient with a known large cholesteatoma (TD05T\_MUSE\_007) was recruited for scanning at 0.5 T with both the standard protocol and additional scans exploring diffusion restriction and T2 shine-through. From the ADC map of one of the ms-DW-EPI scans, the ADC of the cholesteatoma was approximated to be 0.55. From there, two scans were added. One scan increased the b-value of 1400 s/mm<sup>2</sup>. The other increased TE to 90 msec. All other parameters were matched to the standard protocol. For contrast analysis, the window and level were gradually dropped for each dataset to probe cholesteatoma contrast (Figure 4.18).



**Figure 4.17.** Protocolling decisions impact pathology contrast. Windowing level was reduced from high to low to highlight the brightest feature. Cholesteatoma is circled in yellow. Distortion and skull are brightest in all except the 3shot TE90 acquisition.



#### 4.2.4 Discussion: Optimizing b-value and TE for cholesteatoma contrast

It was expected that the 1-shot acquisition would show similar contrast between cholesteatoma and distortion, and this was observed. It was expected that if cholesteatoma contrast was dependent on b-value, TE value, or both, the relative cholesteatoma contrast between the standard 3-shot acquisition and the optimized acquisitions would change.

Surprisingly, cholesteatoma contrast was similar between applied b-values of 1000 and 1400  $s/mm^2$  despite the low ADC. Adjusting the TE value to 90, however, had the effect of improved cholesteatoma contrast. This suggests a dominant T2 shine-through effect compared to diffusion restriction for cholesteatoma contrast. However, this investigation was done on only a single patient. This participant was suspected to have a cholesteatoma and may have also had a fluid-filled mass in an anatomically similar region. This may have confounded the results. Further investigation would need to be done to further explore this phenomenon.

Taken together, these results demonstrate that the MUSE reconstruction pipeline designed in this study was implemented in such a way as to effectively reduce ghosting in ms-DW-EPI images at 0.5 T. This supported a pilot investigation into its use with cholesteatoma imaging. The results shown here demonstrate that the offline MUSE reconstruction pipeline does not degrade overall image quality compared to clinical standard, and that this technique offers pathology contrast with distortion reduction that warrants further investigation.

## 5. Conclusions and Future Directions

In the current work, an offline MUSE reconstruction pipeline was developed to explore the hypothesis that sufficient SNR will be provided by ms-DW-EPI acquired at 0.5T to perform MUSE and there will be a quantifiable reduction in motion-induced ghosting compared to images reconstructed without MUSE correction. In this work, it has been demonstrated that ms-DW-EPI at 0.5 T with MUSE correction reduces ghosting and maintains image integrity, confirming the hypothesis.

The investigation into this hypothesis was divided into four objectives. First, a protocol to offload raw k-space data from the MRI console and organize it into a logical structure was developed. To do this, an offline reconstruction pipeline that took raw k-space data as input and produced intermediate breadcrumbs as output was obtained and modified to produce individual files for each average, slice, diffusion direction, and shot. These files were transformed into cartesian-gridded k-space to address the second objective. Here, an offline MUSE reconstruction pipeline was developed to correct for the motion-induced phase errors inherent to ms-DW-EPI as described by Chen et. al.<sup>33</sup>. Phantom, healthy volunteer, and patient data was used to develop and troubleshoot, refine for human subjects, and specialize the pipeline for the clinical application, respectively. As the MUSE pipeline reached a point of producing images of acceptable quality, the acquisition sequence parameters were adjusted towards the standard for clinical application, addressing objective three. These changes reduced the overall produced signal, and so the pipeline was simultaneously adjusted to accommodate this. The fourth objective was to qualitatively evaluate the produced images with visual

inspection of ghosting and quantitate GSR, DSR, PSR, and PDR. The MUSE images consistently had reduced ghosting compared to the vendor reconstructed images. This was supported by the mean GSR of the 2-shot vendor images being significantly less than the 2-shot MUSE images ( $p=0.049$ ), as well as the mean GSR for the 1-shot with and without PI, 2-shot MUSE, and 3-shot MUSE being not significantly different.

A pilot investigation into the clinical applicability of ms-DW-EPI at 0.5 T for cholesteatoma imaging looked at factors impacting signal pile-up due to distortion such as field strength and number of shots. At 0.5 T, the pathology was distinguishable with a PSR above 1 regardless of acquisition or reconstruction method. However, distortion robustness could still be improved as the PDR was not significantly above 1 for any of the acquisition or reconstruction methods. Comparing with 3 T, the 0.5 T images outperformed the 3 T MUSE for distortion reduction. An initial exploration into optimizing acquisition parameters for pathology contrast explored the effects of b-value and TE. This provides a basis on which further work can build off of for optimizing pathology contrast for use by clinical experts.

Future directions for this work should address the current limitations in order to strengthen clinical applicability. The most significant source of error in this project was the coil sensitivities. The coil coefficient breadcrumbs were the ideal source of sensitivities to most closely resemble the vendor reconstruction. However, there were challenges in matching the coil coefficients to the acquired data, most likely related to how sensitivities are unwrapped in the online vendor reconstruction pipeline. The derived sensitivities were sufficient for the current work, but the parameters for the

functions used to mitigate the noise needed to be adjusted for each dataset. On a small sample size as in this study, this is reasonable. However, onboarding the MUSE pipeline into the online vendor reconstruction would allow for the use of the vendor coil sensitivities, as well as gradient warping correction and proper image resizing. It would also allow for a streamlined large-scale investigation into the use of DW-EPI at 0.5 T for use with cholesteatoma imaging.

Considerations for reducing distortion and optimizing pathology contrast were explored here. The current offline reconstruction pipeline is limited to fully sampled datasets since the sensitivities are derived from the data, and accurate sensitivities cannot be derived from an under-sampled dataset because of the under-sampling artifact. If coil sensitivities were not a barrier, parallel imaging could be combined with ms-DW-EPI. In doing so, the time saved by collecting fewer k-space lines could be used to increase the number of averages while still reducing distortion by using a multishot acquisition. It has been demonstrated here that the vendor reconstruction of 1-shot PI2 has reduced distortion compared to a 1-shot without PI. It would be expected that combining a multishot acquisition with PI should also improve distortion. The ETL and matrix size are currently limited by vendor restraints, but once these are overcome, both can be adjusted to reduce readout time and improve distortion further. With reduced distortion, focus can turn to making pathology the brightest feature for ease of physician use. This could include looking at how a larger sample size of cholesteatoma tissue behaves under different TE and b-values. Furthermore, with an optimized protocol and consistent noise reduction from onboarding the MUSE pipeline onto the

MRI console, it could be of interest to recruit a large cohort of patients with diagnosed cholesteatoma for scanning with the current protocol and clinical standard at 3 T, and to present the results to clinical experts for comparison of image quality and diagnostic confidence.

Taken together, a ms-DW-EPI acquisition at 0.5 T with MUSE correction has been demonstrated to reduce ghosting and maintain image integrity. Demonstrated cholesteatoma image quality supports further exploration into the optimal acquisition sequence for reduced distortion and maximum cholesteatoma contrast.

## References

1. Swartz JD. Cholesteatomas of the Middle Ear: Diagnosis, Etiology, and Complications. *Radiol Clin North Am.* 1984;22(1):15-35. doi:10.1016/S0033-8389(22)01134-4
2. Morris P. *Chronic Suppurative Otitis Media.*; 2013. www.aafp.org/afp.
3. Im GJ, do Han K, Park KH, et al. Rate of chronic otitis media operations and cholesteatoma surgeries in South Korea: a nationwide population-based study (2006-2018). *Sci Rep.* 2020;10(1):11356. doi:10.1038/s41598-020-67799-5
4. Baráth K, Huber AM, Stämpfli P, Varga Z, Kollias S. Neuroradiology of cholesteatomas. *AJNR Am J Neuroradiol.* 2011;32(2):221-229. doi:10.3174/ajnr.A2052
5. Ansari A, Tariq MA, Sadiq NM. *Histology, Ear.*; 2023.
6. Bollmann R, Knopp U, Tolsdorff P. [DNA cytometric studies of cholesteatoma of the middle ear]. *HNO.* 1991;39(8):313-314.
7. Rothschild S, Ciernik IF, Hartmann M, Schuknecht B, Lütolf UM, Huber AM. Cholesteatoma triggering squamous cell carcinoma: case report and literature review of a rare tumor. *Am J Otolaryngol.* 30(4):256-260. doi:10.1016/j.amjoto.2008.06.011
8. Miyamoto RT. Otitis Media (Chronic Suppurative). Merck Manual.
9. Newsted D, Rosen E, Cooke B, Beyea MM, Simpson MTW, Beyea JA. Approach to hearing loss. *Can Fam Physician.* 2020;66:803-809.
10. Chee NW, Tan TY. The value of pre-operative high resolution CT scans in cholesteatoma surgery. *Singapore Med J.* 2001;42(4):155-159.
11. Jindal M, Riskalla A, Jiang D, Connor S, O'Connor AF. A systematic review of diffusion-

weighted magnetic resonance imaging in the assessment of postoperative cholesteatoma. *Otol Neurotol*. 2011;32(8):1243-1249.

doi:10.1097/MAO.0b013e31822e938d

12. Mount Sinai. Cholesteatoma. Mount Sinai.
13. Møller PR, Pedersen CN, Grosfeld LR, Faber CE, Djurhuus BD. Recurrence of Cholesteatoma - A Retrospective Study Including 1,006 Patients for More than 33 Years. *Int Arch Otorhinolaryngol*. 2020;24(1):e18-e23. doi:10.1055/s-0039-1697989
14. Myers EN, Stangerup S, Drozdiewicz D, Tos M, Hougaard-Jensen A. Recurrence of Attic Cholesteatoma: Different Methods of Estimating Recurrence Rates. *Otolaryngol Neck Surg*. 2000;123(3):283-287. doi:10.1067/mhn.2000.104666
15. Vercruyse J-P, De Foer B, Pouillon M, Somers T, Casselman J, Offeciers E. The value of diffusion-weighted MR imaging in the diagnosis of primary acquired and residual cholesteatoma: a surgical verified study of 100 patients. *Eur Radiol*. 2006;16(7):1461-1467. doi:10.1007/s00330-006-0160-2
16. Keeler JA, Kaylie DM. Cholesteatoma: Is a second stage necessary? *Laryngoscope*. 2016;126(7):1499-1500. doi:10.1002/lary.25385
17. Osman NMM, Rahman AA, Ali MTAH. The accuracy and sensitivity of diffusion-weighted magnetic resonance imaging with Apparent Diffusion Coefficients in diagnosis of recurrent cholesteatoma. *Eur J Radiol Open*. 2017;4:27-39. doi:10.1016/J.EJRO.2017.03.001
18. Migirov L, Tal S, Eyal A, Kronenberg J. MRI, not CT, to rule out recurrent cholesteatoma and avoid unnecessary second-look mastoidectomy. *Isr Med Assoc J*. 2009;11(3):144-146.

19. Djalilian HR, Rubinstein M, Wu EC, et al. Optical coherence tomography of cholesteatoma. *Otol Neurotol*. 2010;31(6):932-935.  
doi:10.1097/mao.0b013e3181e711b8
20. Henninger B, Kremser C. Diffusion weighted imaging for the detection and evaluation of cholesteatoma. *World J Radiol*. 2017;9(5):217. doi:10.4329/wjr.v9.i5.217
21. Mas-Estelles F, Mateos-Fernandez M, Carrascosa-Bisquert B, Facal de Castro F, Pcuahses-Román I, Morera-Perez C. Contemporary Non-Echo-planar Diffusion-Weighted Imaging of Middle Ear Cholesteatomas. *Radiographics*. 2012;32(4):1197-1213.
22. Choi DL, Gupta MK, Rebello R, Archibald JD. Cost-comparison analysis of diffusion weighted magnetic resonance imaging (DWMRI) versus second look surgery for the detection of residual and recurrent cholesteatoma. *J Otolaryngol - Head Neck Surg*. 2019;48(1):58. doi:10.1186/s40463-019-0384-1
23. Lehmann P, Saliou G. 3T MR Imaging of Postoperative Recurrent Middle Ear Cholesteatomas: Value of Periodically Rotated Overlapping Parallel Lines with Enhanced Reconstruction Diffusion- Weighted MR Imaging. *Am J Neuroradiol*. 2009;30(2):423-427.  
doi:https://doi.org/10.3174/ajnr.A1352
24. Dubrulle F, Souillard R, Chechin D, Vaneecloo FM, Desaulty A, Vincent C. Diffusion-weighted MR imaging sequence in the detection of postoperative recurrent cholesteatoma. *Radiology*. 2006;238(2):604-610. doi:10.1148/radiol.2381041649
25. Schwartz KM, Lane JI, Bolster BD, Neff BA. The utility of diffusion-weighted imaging for cholesteatoma evaluation. *AJNR Am J Neuroradiol*. 2011;32(3):430-436.  
doi:10.3174/ajnr.A2129



26. Paireudeau C, Mendonca C. Anaesthesia for major middle ear surgery. *BJA Educ.* 2019;19(5):136-143. doi:10.1016/j.bjae.2019.01.006
27. Kimitsuki T, Suda Y, Kawano H, Tono T, Komune S. Correlation between MRI Findings and Second-Look Operation in Cholesteatoma Surgery. *ORL.* 2001;63(5):291-293. doi:10.1159/000055760
28. Amoodi H, Mofti A, Fatani NH, Alhatem H, Zabidi A, Ibrahim M. Non-echo Planar Diffusion-Weighted Imaging in the Detection of Recurrent or Residual Cholesteatoma: A Systematic Review and Meta-Analysis of Diagnostic Studies. *Cureus.* December 2022. doi:10.7759/cureus.32127
29. Migirov L, Wolf M, Greenberg G, Eyal A. Non-EPI DW MRI in Planning the Surgical Approach to Primary and Recurrent Cholesteatoma. *Otol Neurotol.* 2014;35(1):121-125. doi:10.1097/MAO.0000000000000234
30. Khemani S, Lingam RK, Kalan A, Singh A. The value of non-echo planar HASTE diffusion-weighted MR imaging in the detection, localisation and prediction of extent of postoperative cholesteatoma. *Clin Otolaryngol.* 2011;36(4):306-312. doi:10.1111/j.1749-4486.2011.02332.x
31. Li P, MCMC, Linos E, Gurgel RK, Fischbein NJ, Blevins NH. Evaluating the utility of non-echo-planar diffusion-weighted imaging in the preoperative evaluation of cholesteatoma: A meta-analysis. *Laryngoscope.* 2013;123(5):1247-1250. doi:10.1002/lary.23759
32. Feinberg DA, Moeller S, Smith SM, et al. Multiplexed Echo Planar Imaging for Sub-Second Whole Brain fMRI and Fast Diffusion Imaging. Valdes-Sosa PA, ed. *PLoS One.* 2010;5(12):e15710. doi:10.1371/journal.pone.0015710

33. Chen N kuei, Guidon A, Chang HC, Song AW. A robust multi-shot scan strategy for high-resolution diffusion weighted MRI enabled by multiplexed sensitivity-encoding (MUSE). *Neuroimage*. 2013;72:41-47. doi:10.1016/j.neuroimage.2013.01.038
34. Liu J, Xu M, Ren J, Li Z, Xi L, Chen B. Synthetic MRI, multiplexed sensitivity encoding, and BI-RADS for benign and malignant breast cancer discrimination. *Front Oncol*. 2022;12:1080580. doi:10.3389/fonc.2022.1080580
35. Hu Y, Ikeda DM, Pittman SM, et al. Multishot Diffusion-Weighted MRI of the Breast With Multiplexed Sensitivity Encoding (MUSE) and Shot Locally Low-Rank (Shot-LLR) Reconstructions. *J Magn Reson Imaging*. 2021;53(3):807-817. doi:10.1002/jmri.27383
36. Naranjo ID, Gullo R Lo, Morris EA, et al. High-Spatial-Resolution Multishot Multiplexed Sensitivity-encoding Diffusion-weighted Imaging for Improved Quality of Breast Images and Differentiation of Breast Lesions: A Feasibility Study. *Radiol Imaging Cancer*. 2020;2(3).
37. El Homsy M, Bates DDB, Mazaheri Y, Sosa R, Gangai N, Petkovska I. Multiplexed sensitivity-encoding diffusion-weighted imaging (MUSE) in diffusion-weighted imaging for rectal MRI: a quantitative and qualitative analysis at multiple b-values. *Abdom Radiol (New York)*. 2023;48(2):448-457. doi:10.1007/s00261-022-03710-2
38. Chang H-C, Chen G, Chung H-W, et al. Multi-shot Diffusion-Weighted MRI With Multiplexed Sensitivity Encoding (MUSE) in the Assessment of Active Inflammation in Crohn's Disease. *J Magn Reson Imaging*. 2022;55(1):126-137. doi:10.1002/jmri.27801
39. Konar AS, Fung M, Paudyal R, et al. Diffusion-Weighted Echo Planar Imaging using MULTiplexed Sensitivity Encoding and Reverse Polarity Gradient in Head and Neck Cancer:

An Initial Study. *Tomogr (Ann Arbor, Mich)*. 2020;6(2):231-240.

doi:10.18383/j.tom.2020.00014

40. Chang H-C, Gaur P, Chou Y, Chu M-L, Chen N. Interleaved EPI based fMRI improved by multiplexed sensitivity encoding (MUSE) and simultaneous multi-band imaging. *PLoS One*. 2014;9(12):e116378. doi:10.1371/journal.pone.0116378
41. Chu M-L, Chang H-C, Chung H-W, et al. Free-breathing abdominal MRI improved by repeated k-t-subsampling and artifact-minimization (ReKAM). *Med Phys*. 2018;45(1):178-190. doi:10.1002/mp.12674
42. Xie S, Zhang Z, Chang F, et al. Subcortical White Matter Changes with Normal Aging Detected by Multi-Shot High Resolution Diffusion Tensor Imaging. *PLoS One*. 2016;11(6):e0157533. doi:10.1371/journal.pone.0157533
43. Ota T, Tsuboyama T, Onishi H, et al. Diagnostic accuracy of MRI for evaluating myometrial invasion in endometrial cancer: a comparison of MUSE-DWI, rFOV-DWI, and DCE-MRI. *Radiol Med*. 2023;128(6):629-643. doi:10.1007/s11547-023-01635-4
44. Bai Y, Pei Y, Liu WV, et al. MRI: Evaluating the Application of FOCUS-MUSE Diffusion-Weighted Imaging in the Pancreas in Comparison With FOCUS, MUSE, and Single-Shot DWIs. *J Magn Reson Imaging*. 2023;57(4):1156-1171. doi:10.1002/jmri.28382
45. Liu X, Hui ES, Chang H-C. Elimination of residual aliasing artifact that resembles brain lesion on multi-oblique diffusion-weighted echo-planar imaging with parallel imaging using virtual coil acquisition. *J Magn Reson Imaging*. 2020;51(5):1442-1453. doi:10.1002/jmri.26966
46. Chen ZQ, Zhang D, Wang Z, et al. The value of DISCO and MUSE-DWI combined with

prostate specific antigen density in the diagnosis and risk stratification of prostate cancer. *Zhonghua Yi Xue Za Zhi*. 2023;103(19):1461-1468. doi:10.3760/cma.j.cn112137-20221018-02176

47. Klein H-M. Low-Field Magnetic Resonance Imaging. *Fortschr Röntgenstr*. 2020;192:537-548.
48. Collins CM, Smith MB. Signal-to-noise ratio and absorbed power as functions of main magnetic field strength, and definition of "90°" RF pulse for the head in the birdcage coil. *Magn Reson Med*. 2001;45(4):684-691. doi:10.1002/mrm.1091
49. Breit H-C, Vosschenrich J, Bach M, Merkle EM. Neue klinische Anwendungsbereiche der Niederfeld-Magnetresonanztomographie. *Radiologe*. 2022;62(5):394-399. doi:10.1007/s00117-022-00967-y
50. Hashemi RH, Bradley WGJ, Lisanti CJ. Basic Principles of MRI. In: *MRI: The Basics*. Third. Lippincott Williams & Wilkins; 2010:16-29.
51. Hashemi RH, Bradley WGJ, Lisanti CJ. T1, T2, and T2\*. In: *MRI: The Basics*. Third. Lippincott Williams & Wilkins; 2010:40-47.
52. Hashemi RH, Bradley WGJ, Lisanti CJ. TR, TE, and Tissue Contrast. In: *MRI: The Basics*. Third. Lippincott Williams & Wilkins; 2010:48-56.
53. Mezrich R. A Perspective on K-Space. *Radiology*. 1995;195:297-315.
54. Rosen B, Wald L. MR Image Encoding. 2006.
55. Larkman DJ, Nunes RG. Parallel magnetic resonance imaging. *Phys Med Biol*. 2007;52(7):R15-R55. doi:10.1088/0031-9155/52/7/R01

56. Blaimer M, Breuer F, Mueller M, Heidemann RM, Griswold MA, Jakob PM. SMASH, SENSE, PILS, GRAPPA: How to Choose the Optimal Method. *Top Magn Reson Imaging*. 2004;15(4):223-236.
57. Pruessmann KP, Weiger M, Scheidegger MB, Boesiger P. SENSE: Sensitivity encoding for fast MRI. *Magn Reson Med*. 1999;42(5):952-962. doi:10.1002/(SICI)1522-2594(199911)42:5<952::AID-MRM16>3.0.CO;2-S
58. Bammer R, Keeling SL, Augustin M, et al. Improved diffusion-weighted single-shot echo-planar imaging (EPI) in stroke using sensitivity encoding (SENSE). *Magn Reson Med*. 2001;46(3):548-554. doi:10.1002/mrm.1226
59. Stejskal EO, Tanner JE. Spin Diffusion Measurements: Spin Echoes in the Presence of a Time-Dependent Field Gradient. *J Chem Phys*. 1965;42(1):288-292. doi:10.1063/1.1695690
60. Le Bihan D. Diffusion MRI: What water tells us about the brain. *EMBO Mol Med*. 2014;6(5):569-573. doi:10.1002/emmm.201404055
61. Baliyan V, Das CJ, Sharma R, Gupta AK. Diffusion weighted imaging: Technique and applications. *World J Radiol*. 2016;8(9):785. doi:10.4329/wjr.v8.i9.785
62. Dietrich O, Biffar A, Baur-Melnyk A, Reiser MF. Technical aspects of MR diffusion imaging of the body. *Eur J Radiol*. 2010;76(3):314-322. doi:10.1016/j.ejrad.2010.02.018
63. Park MY, Byun JY. Understanding the Mathematics Involved in Calculating Apparent Diffusion Coefficient Maps. *Am J Roentgenol*. 2012;199(6):W784-W784. doi:10.2214/AJR.12.9231
64. Anderson AW, Gore JC. Analysis and correction of motion artifacts in diffusion weighted

- imaging. *Magn Reson Med*. 1994;32(3):379-387. doi:10.1002/mrm.1910320313
65. Hashemi RH, Bradley WGJ, Lisanti CJ. Echo Planar Imaging. In: *MRI: The Basics*. Third. Philadelphia: Lippincott Williams & Wilkins; 2010:257-267.
66. Chu M-L, Chang H-C, Chung H-W, Truong T-K, Bashir MR, Chen N. POCS-based reconstruction of multiplexed sensitivity encoded MRI (POCSMUSE): A general algorithm for reducing motion-related artifacts. *Magn Reson Med*. 2015;74(5):1336-1348. doi:10.1002/mrm.25527
67. Zhang H, Wang C, Chen W, et al. Deep learning based multiplexed sensitivity-encoding (DL-MUSE) for high-resolution multi-shot DWI. *Neuroimage*. 2021;244:118632. doi:10.1016/J.NEUROIMAGE.2021.118632
68. Panther A, Thevathasen G, Connell IRO, et al. A Dedicated Head-Only MRI Scanner for Point-of-Care Imaging Barriers to MRI being used at the point-of-care.
69. Stainsby JA, Bindseil GA, Connell IR, et al. Imaging at 0.5 T with high-performance system components System Components.
70. Connell IR, Panther A, Chronik BA. Specific Absorption Rate in Head-Only Mid-Field Scanner: Comparisons to 1.5 T and 3 T. doi:10.3174/ajnr
71. Stainsby JA, Harris CT, Bindseil GA, Wiens CN, Beatty PJ, Curtis AT. High-Performance Diffusion Imaging on a 0.5T System. *Proc Annu Meet Int Soc Magn Reson Med*. 2019:1-2.
72. Price R, Allison J, Clarke G, et al. Medical Physicist's/MRI Scientist's Section. In: *Magnetic Resonance Imaging Quality Control Manual*. American College of Radiology; 2015:60-61.
73. Reeve S, Guida A, Bowen C, et al. Super resolution permits fast, low resolution bSSFP

imaging of the temporal bone...but do radiologists agree on image quality? In:  
*Proceedings of the Annual Meeting of the International Society for Magnetic Resonance  
in Medicine*. Toronto; 2023.

74. Chiew M. SENSE Parallel Imaging.  
[https://users.fmrib.ox.ac.uk/~mchiew/docs/SENSE\\_tutorial.html](https://users.fmrib.ox.ac.uk/~mchiew/docs/SENSE_tutorial.html).
75. Walsh DO, Gmitro AF, Marcellin MW. Adaptive reconstruction of phased array MR  
imagery. *Magn Reson Med*. 2000;43(5):682-690. doi:10.1002/(sici)1522-  
2594(200005)43:5<682::aid-mrm10>3.0.co;2-g
76. Herterich R, Sumarokova A. Coil Sensitivity Estimation and Intensity Normalisation for  
Magnetic Resonance Imaging. October 2019. doi:10.13140/RG.2.2.22886.04169
77. Lourakis M. TV-L1 Image Denoising Algorithm. 2022.  
[https://www.mathworks.com/matlabcentral/fileexchange/57604-tv-l1-image-denoising-  
algorithm](https://www.mathworks.com/matlabcentral/fileexchange/57604-tv-l1-image-denoising-algorithm).
78. Pryde M, Reeve S. COPY\_Rad\_Study\_FINAL\_Stroke\_Pipeline\_FHM.m. 2022.
79. Xu M, Fralick D, Zheng JZ, Wang B, Tu XM, Feng C. The Differences and Similarities  
Between Two-Sample T-Test and Paired T-Test. *Shanghai Arch psychiatry*.  
2017;29(3):184-188. doi:10.11919/j.issn.1002-0829.217070

## Appendix A: Data Transfer

The protocol for transferring raw k-space off the console MRI and partially reconstructed offline is as follows.

### 1. Get DataCapture reconstruction ID

- If acquisition type is 'raw'
  - In separate tab, navigate to 'Data' -> on left hand side of screen click on desired acquisition -> on right-hand of screen click on DataCapture -> record ReconID
- If acquisition type does not include 'raw'
  - In separate tab, navigate to 'Data' -> on left hand side of screen click on desired acquisition -> on right-hand of screen click on 'run DataCapture' -> when reconstruction reaches 100% click on DataCapture -> record ReconID
- Note: **Do not click 'End Study' before until ReconIDs are recorded**

### Offline:

#### 1. Copy data capture off 0.5T into working directory

- a. Search `ls -ltr` of `/lauterbur/synaptive/` and check filename for reconstruction ID
- b. Move to `/biotic/home/allyk/data/TestData`
- c. Rename as
  - a. Phantom: `[Date]_[slice plane]_DWI_[num shot]_[num avg]`
  - b. Volunteer: `TD05T_MUSE_[ID number]_[slice plane]_DWI_[num shot]_[num avg]`

#### 2. Run offline reconstruction within Docker

- Log into biotic server
  - In terminal: `docker run --rm --it --v /biotic/home/allyk/data/TestData:/Data -v /biotic/home/allyk/Desktop/OfflineEPIRecon/dev-bin:/dev-bin --net=host --env="DISPLAY" -v $HOME/.Sauthority:/root/.Xauthority --name=synrun2204 synaptive/run 2204`
  - Change directory: `cd /Data`
- #### 3. Run reconstruction
- `/dev-bin/Epi_Attempt4-Offline -p params_good.json -f filename.h5 -m dorecon`
  - Move breadcrumbs:
    - `Mv Breadcrumbs Breadcrumbs_filename`

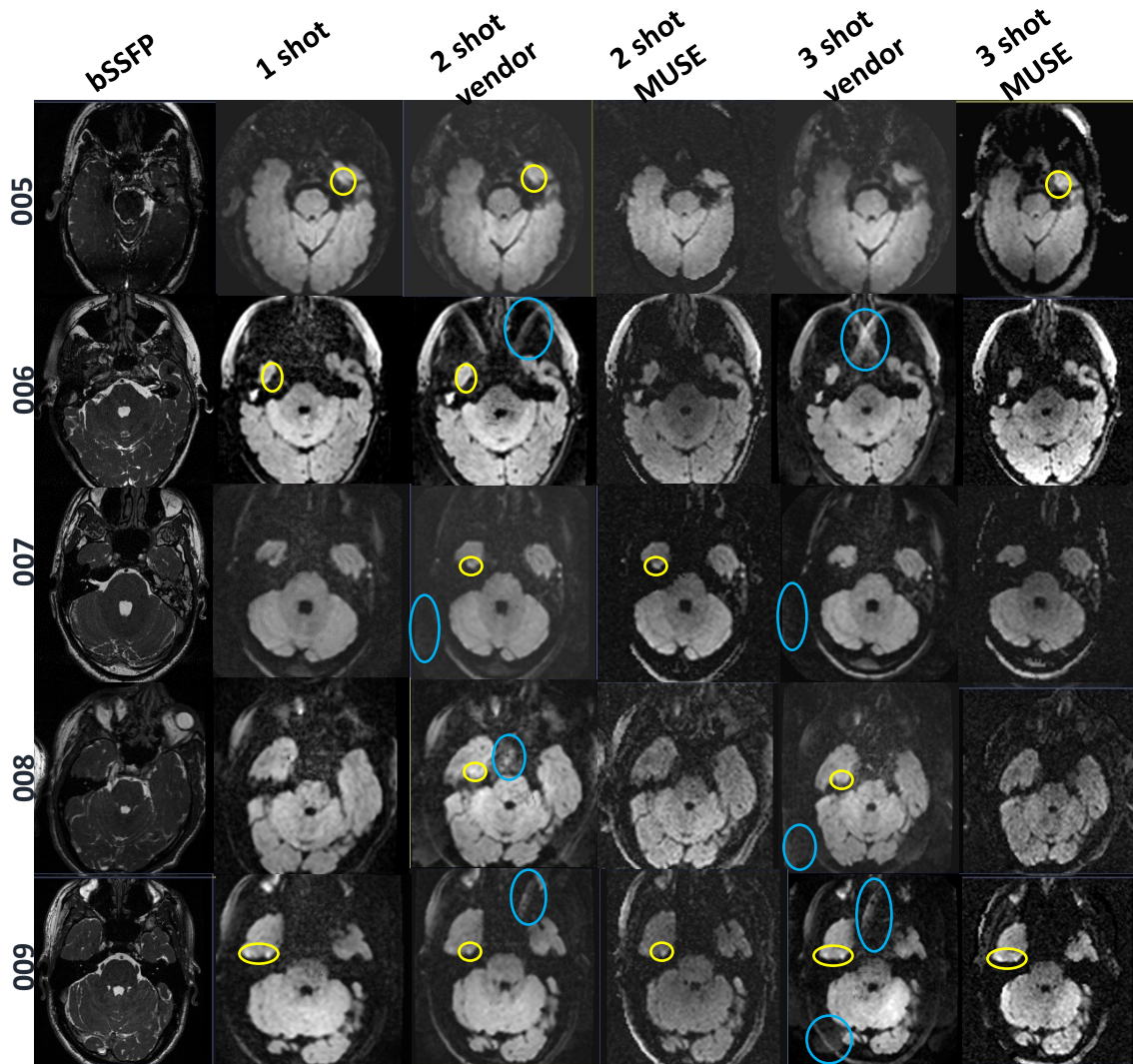
#### 3. Open 'entire\_pipeline\_JR\_new.m' in Matlab

#### 4. Add filepaths



## Appendix II: Additional Images

Ghosting changes across acquisition parameter and volunteers (005-009). Image sets 005-007 are from patients with diagnosed cholesteatoma. Ghosting is circled in blue. Signal pile-up due to distortion is circled in yellow



## Appendix C: MUSE Matlab Code

```
% For DWI 4-diffusion direction 1 shot acquisition with 3 avgs
file_directory =
'/biotic/home/allyk/data/TestData/Breadcrumbs_TD05T_007_3shot_2mm_iso';
%raw_h5 =
'/biotic/home/allyk/data/TestData/May3_Ax_DWI_3shot_8avgs_2mm_iso.h5';
addpath(file_directory);
addpath('/biotic/home/allyk/matlab/SENSE/SENSE_Code');
hybrid_images_dir = dir([file_directory, '/*' 'HybridImages' '*']);

% Eventually should get all these from file header
Nx = 128;%SFoff=176
Ny = 96;%96 or 128
Nz = 28;
Ns = 3;
Nd = 4;
Na = 8;
Nc = 8;
slice = 19;

if ~exist('read_files','var')
    read_files = true;
end
if read_files

file_kspace = zeros(Nx,Ny,Nc);
file_imspace = zeros(Nx,Ny,Nc);
full_image_space = zeros(Nx,Ny,Nz,Ns,Nd,Na,Nc);
full_k_space_master = zeros(Nx,Ny,Nz,Ns,Nd,Na,Nc);

% Read slice number for each hybrid image
for i=1:numel(hybrid_images_dir)
    single_slice = hybrid_images_dir(i).name;
    split_str = strsplit(single_slice,{'_', '.'});
    slice_num = str2double(split_str{5});
    shot_num = str2double(split_str{7});
    diff_dir = str2double(split_str{9});
    avg = str2double(split_str{11});
    slice_location = strcat(file_directory, '/', single_slice);
    for s = 1:Nc
        channel_number = sprintf('%05d',s-1);
        slice_hybrid = h5read(slice_location, (['/' channel_number
'/data']));
        corrected_slice_hybrid = permute(slice_hybrid,[2,1]);
        complex_config =
complex(corrected_slice_hybrid(:,1:2:end),corrected_slice_hybrid(:,2:2:end));
        kspace = fftc(complex_config,1);
        file_kspace(:, :, s) = kspace;
        file_imspace(:, :, s) = fft2c(kspace);
    end
    full_k_space_master(:, :, slice_num, shot_num, diff_dir, avg, :) = file_kspace;
    full_image_space(:, :, slice_num, shot_num, diff_dir, avg, :) = file_imspace;
end
%for a = 1:Na
```

```

%full_k_space = squeeze(sum(full_k_space(:,:, :, :, :, [1:a], :), 6));

% % Read Output Images
% output_image_dir = dir([file_directory, '/*outputImage*']);
% output_image = zeros(256,256,numel(output_image_dir));
% for i=1:numel(output_image_dir)
%     single_slice = output_image_dir(i).name;
%     split_str = strsplit(single_slice,{'_', '.'});
%     child_num = str2double(split_str{5});
%     slice_location = strcat(file_directory, '/', single_slice);
%     pre_zeros_channel_number = '/00000';
%     image_slice = h5read(slice_location, [pre_zeros_channel_number
'/data']);
%     corrected_image_slice = permute(image_slice,[2,1]);
%     complex_data =
complex(corrected_image_slice(:,1:2:end),corrected_image_slice(:,2:2:end));
%     output_image(:,:,child_num) = complex_data; %make complex then
interpolate down using imresize
% end
% coil_coefficient_dir = dir([file_directory, '/'
'ChannelCombinationCoefficients' '*']);
% slice_coil_comb = zeros(Nx,Ny,Nc);
% coil_comb = zeros(Nx,Ny,Nz,Nd,Nc);
% coil_comb_average_count = zeros(Nz,1);
% for i=1:numel(coil_coefficient_dir)
%     single_slice = coil_coefficient_dir(i).name;
%     split_str = strsplit(single_slice,{'_', '.'});
%     slice_num = str2double(split_str{5});
%     slice_location = strcat(file_directory, '/', single_slice);
%     coil_comb_average_count(slice_num) =
coil_comb_average_count(slice_num)+1;
%     for s = 1:Nc
%         channel_number = sprintf('%05d',s-1);
%         channel_comb = h5read(slice_location, (['/' channel_number
'/data']));
%         corrected_channel_comb = permute(channel_comb,[2,1]);
%         complex_data =
complex(corrected_channel_comb(:,1:2:end),corrected_channel_comb(:,2:2:end));
%         slice_coil_comb(:,:,s) = imresize(complex_data,[Nx,Ny]);
%     end
%     coil_comb(:,:,slice_num,coil_comb_average_count(slice_num),:) =
slice_coil_comb; %make complex then interpolate down using imresize
% end
% Noise Handling
% info = h5info(raw_h5);
% seq_params = info.Attributes(1).Value;
% headerSummary = info.Groups(2);
%
% UID_noise = h5read(raw_h5, '/metaData/dataDescriptions/noise/uidList');
% noise_UID = lower(dec2hex(UID_noise));
% base_name = info.Groups(1).Groups.Name;
% UID = sprintf('%016s',noise_UID);
% dataset_name = [base_name '/' UID]; % channel_number = sprintf('%05d',s-1);
% kspace_noise = h5read(raw_h5,dataset_name);
%

```

```

% [Nn,Nc] = size(kspace_noise);
% temp = complex(kspace_noise(:,1:2:end),kspace_noise(:,2:2:end));
% %temp = kspace_noise;
% noise = reshape(temp,numel(temp)/Nc,Nc);
% noise = permute(noise,[2 1]);
% NSamples=size(noise,2);
% psi = (1/(NSamples-1))*(noise*noise');
%
read_files = false;
end
%% SNR at various averages
%for a = 1:Na
%full_k_space = squeeze(sum(full_k_space(:,:,:, :, [1:a],:),6));
full_k_space = squeeze(sum(full_k_space_master,6));
% Derive sensitivities
der_sens_SENSE = zeros(Nx,Ny,Nz,Nc);
nd_der_sens_SENSE = zeros(Nx,Ny,Nz,Nc); %noise decorrelation
for Z = 1:Nz
% 4shot sens
dataset = squeeze(full_k_space(:,:,Z, :, 1,:));
%dataset = squeeze(sum(full_k_space(:,:,Z, :, 1,[1:a],:),6));
dataset = squeeze(sum(dataset,3));
%[Nx,Ny,Nc] = size(dataset);
img = ifft2c(hanning(length(dataset),'symmetric').*dataset);
%img = ifft2c(dataset);
img_combined = sqrt(sum(abs(img).^2,3));
%img_combined = sum(img*,3);

% thresh = 0.02*max(abs(img_combined(:)));
% mask = abs(img_combined) > thresh;

% Original: Estimate Sensitivities
S_0 = img./img_combined;
%S_0 = squeeze(coil_comb(:,:,Z,1,:));
S_1 = zeros(Nx,Ny,Nc);
%S_inv = zeros(Nx,Ny,Nc);
for i = 1:Nc
    %S_x = imgaussfilt3(abs(S_0(:,:,i)),0.8);
    %S_x = imgaussfilt(abs(S_0(:,:,i)),[6 3]);
    S_x = smoothdata(S_0(:,:,i),1,'gaussian',12);% 9
    S_y = smoothdata(S_x,2,'gaussian',12);% 6
    %S_1_norm = S_y.*(1./max(S_y,[],[1 2]));
    S_1(:,:,i) = S_y;
end

% S_1 = smooth3(S_0,'gaussian',[3 3 3]);
thresh = 0.2*max(abs(img_combined(:)));
mask = abs(img_combined) > thresh;
S_1_mask = S_1.*mask;
% S_1_mask(S_1_mask ==0) = max(abs(S_1(:)))/2;
%S_1_norm = S_1_mask.*(1./max(S_1_mask,[],[1 2]));
S_1_mask(S_1_mask ==0) = 0.8;

der_sens_SENSE(:,:,Z,:) = S_1_mask;
%der_sens_SENSE(:,:,Z,:) = S_inv;

```

```

%
% % With noise decorrelation
% csm = reshape(S_1, [Nx*Ny Nc]);
% relative_ccm = conj(csm) * pinv(psi);
% %relative_ccm = conj(csm)*pinv(eye(8));
% scale_correction = abs(sum(relative_ccm.*csm,2));
% corr_img = 1./scale_correction;
% corr_img(corr_img==Inf) = 0;
% corr_img = reshape(corr_img,[Nx Ny]);
% nonzero_ind = scale_correction>0;
% ccm = zeros(size(csm));
% ccm(nonzero_ind, :) = relative_ccm(nonzero_ind,:) ./
repmat(scale_correction(nonzero_ind),[1 Nc]);
% % show_img(abs(relative_ccm));
% ccm = reshape(ccm, [Nx Ny Nc]);
% %im_composite = sum(ccm.*img,3);
% %show_img(abs(im_composite));
% nd_der_sens_SENSE(:, :, Z, :) = ccm;
end
% Initial SENSE for deriving phase maps
%full_k_space_avg = full_k_space;
%% shots_separate_SENSE_recon = zeros(Nx,Ny,Nz,Na,Ns,Nd);
shots_separate_SENSE_recon = zeros(Nx,Ny,Nz,Ns,Nd);
for Z = 1:Nz
S_2 = squeeze(der_sens_SENSE(:, :, Z, :));
for shot=1:Ns
%for avg = 1:Na
for diff= 1:Nd
dataset = squeeze(full_k_space(:, :, Z, shot, diff, :));
%dataset = squeeze(sum(full_k_space_avg(:, :, Z, shot, diff, :, :),6));
%img_R2 = ifft2c(hanning(length(dataset),'symmetric').*dataset);
img_R2 = ifft2c(dataset);
img_R2_SENSE = zeros(Nx,Ny);
for y = 1:Ny/Ns
y_idx = y:Ny/Ns:Ny;
for x = 1:Nx
S_R2 = transpose(reshape(S_2(x,y_idx,:),Ns,[]));
img_R2_SENSE(x,y_idx) = pinv(S_R2,0.3)*reshape(img_R2(x,y,:),[],1);
end
end
end
%shots_separate_SENSE_recon(:, :, Z, avg, shot, diff) = img_R2_SENSE;
shots_separate_SENSE_recon(:, :, Z, shot, diff) = img_R2_SENSE;
end
end
end
%% end
% MUSE Portion
%MUSE_all = zeros(Nx,Ny,Nd,Na,Nz);
MUSE_all = zeros(Nx,Ny,Nd,Nz);
for Z = 1:Nz
channels = squeeze(der_sens_SENSE(:, :, Z, :));

%for avg = 1:Na
for diff = 1:Nd
% %1. Phase variations

```

```

% real_TVshot1 =
TVL1denoise(real(shots_separate_SENSE_recon(:,:,Z,avg,1,diff)),1);
% imag_TVshot1 =
TVL1denoise(imag(shots_separate_SENSE_recon(:,:,Z,avg,1,diff)),1);
real_TVshot1 = TVL1denoise(real(shots_separate_SENSE_recon(:,:,Z,1,diff)),1);
imag_TVshot1 = TVL1denoise(imag(shots_separate_SENSE_recon(:,:,Z,1,diff)),1);
complex_TVshot1 = complex(real_TVshot1,imag_TVshot1);
abs_TVshot1 = abs(complex_TVshot1);
TVshot1 = complex_TVshot1./abs_TVshot1;

% real_TVshot2 =
TVL1denoise(real(shots_separate_SENSE_recon(:,:,Z,avg,2,diff)),1);
% imag_TVshot2 =
TVL1denoise(imag(shots_separate_SENSE_recon(:,:,Z,avg,2,diff)),1);
real_TVshot2 = TVL1denoise(real(shots_separate_SENSE_recon(:,:,Z,2,diff)),1);
imag_TVshot2 = TVL1denoise(imag(shots_separate_SENSE_recon(:,:,Z,2,diff)),1);
complex_TVshot2 = complex(real_TVshot2,imag_TVshot2);
abs_TVshot2 = abs(complex_TVshot2);
TVshot2 = complex_TVshot2./abs_TVshot2;

% real_TVshot3 =
TVL1denoise(real(shots_separate_SENSE_recon(:,:,Z,avg,3,diff)),1);
% imag_TVshot3 =
TVL1denoise(imag(shots_separate_SENSE_recon(:,:,Z,avg,3,diff)),1);
real_TVshot3 = TVL1denoise(real(shots_separate_SENSE_recon(:,:,Z,3,diff)),1);
imag_TVshot3 = TVL1denoise(imag(shots_separate_SENSE_recon(:,:,Z,3,diff)),1);
complex_TVshot3 = complex(real_TVshot3,imag_TVshot3);
abs_TVshot3 = abs(complex_TVshot3);
TVshot3 = complex_TVshot3./abs_TVshot3;

% % TURN OFF MUSE
% TVshot1 = ones(Nx,Ny);
% TVshot2 = ones(Nx,Ny);
% TVshot3 = ones(Nx,Ny);
% TVshot4 = ones(Nx,Ny);
% % Could be MUSE off
% TVshot2(:,(Ny/4+1:Ny/2))=TVshot2(:,(Ny/4+1:Ny/2))*(0-1i);
% TVshot2(:,(Ny/2+1:3*Ny/4))=TVshot2(:,(Ny/2+1:3*Ny/4))*(-1);
% TVshot2(:,(3*Ny/4+1:Ny))=TVshot2(:,(3*Ny/4+1:Ny))*(0+1i);
%
% TVshot3(:,(Ny/4+1:Ny/2))=TVshot3(:,(Ny/4+1:Ny/2))*(-1);
% TVshot3(:,(Ny/2+1:3*Ny/4))=TVshot3(:,(Ny/2+1:3*Ny/4));
% TVshot3(:,(3*Ny/4+1:Ny))=TVshot3(:,(3*Ny/4+1:Ny))*(-1);
%
% TVshot4(:,(Ny/4+1:Ny/2))=TVshot4(:,(Ny/4+1:Ny/2))*(0+1i);
% TVshot4(:,(Ny/2+1:3*Ny/4))=TVshot4(:,(Ny/2+1:3*Ny/4))*(-1);
% TVshot4(:,(3*Ny/4+1:Ny))=TVshot4(:,(3*Ny/4+1:Ny))*(0-1i);

%2. New sensitivities
TVshot1(isnan(TVshot1))=0.8;
TVshot2(isnan(TVshot2))=0.8;
TVshot3(isnan(TVshot3))=0.8;

Sa = (TVshot1).*channels;
Sb = (TVshot2).*channels;

```

```

Sc = (TVshot3).*channels;
S_comp2 = squeeze(cat(3,Sa,Sb,Sc));
% S_comp2 = squeeze(cat(3,Sa,Sb));

%3. Aliased images
shot1 = ifft2c(squeeze(full_k_space(:,:,Z,1,diff,:)));
shot2 = ifft2c(squeeze(full_k_space(:,:,Z,2,diff,:)));
shot3 = ifft2c(squeeze(full_k_space(:,:,Z,3,diff,:)));
% shot4 = ifft2c(squeeze(full_k_space(:,:,Z,4,diff,:)));
% shot1 = ifft2c(squeeze(full_k_space(:,:,Z,1,diff,avg,:)));
% shot2 = ifft2c(squeeze(full_k_space(:,:,Z,2,diff,avg,:)));
% shot3 = ifft2c(squeeze(full_k_space(:,:,Z,3,diff,avg,:)));
img_R2 = cat(3,shot1,shot2,shot3);
% img_R2 = cat(3,shot1,shot2);

img_R2_MUSE = zeros(Nx,Ny);
for y = 1:Ny/Ns
    y_idx = y:Ny/Ns:Ny;
    for x = 1:Nx
        % pick out the sub-problem sensitivities
        S_R2 = transpose(reshape(S_comp2(x,y_idx,:),Ns,[]));
        % solve the sub-problem in the least-squares sense
        %img_R2_MUSE(x,y_idx) =
2*pinv(S_R2,0.01)*reshape(img_R2(x,y,:),[],1);%tolerance: 0.01
        img_R2_MUSE(x,y_idx) =
pinv(S_R2,1.2)*reshape(img_R2(x,y,:),[],1);%tolerance: 1.3 good
        %img_R2_MUSE(x,y_idx) = reshape(img_R2(x,y,:),[],1)./(2*S_R2);
    end
end

MUSE_all(:,:,diff,Z) = img_R2_MUSE;
%MUSE_all(:,:,diff,avg,Z) = img_R2_MUSE;
end
%end
end
%end
%% Calculate ADC
ADC_slices = zeros(Nx,Ny,Nz);
DiffXADC = zeros(Nx,Ny,Nz);
DiffYADC = zeros(Nx,Ny,Nz);
DiffZADC = zeros(Nx,Ny,Nz);

for z = 1:Nz
    b = -1000;
    diff_o = MUSE_all(:,:,1,z);
    diff_x = MUSE_all(:,:,2,z);
    diff_y = MUSE_all(:,:,3,z);
    diff_z = MUSE_all(:,:,4,z);

    % diff_o = MUSE_all(:,:,1,z);
    % diff_x = MUSE_all(:,:,2,z);
    % diff_y = MUSE_all(:,:,3,z);
    % diff_z = MUSE_all(:,:,4,z);

D_x_ADC = log(diff_x./diff_o)/b; DiffXADC(:,:,z) = D_x_ADC;

```



```

D_y_ADC = log(diff_y./diff_o)/b; DiffYADC(:,:,z) = D_y_ADC;
D_z_ADC = log(diff_y./diff_o)/b; DiffZADC(:,:,z) = D_z_ADC;

ADC = D_x_ADC + D_y_ADC + D_z_ADC;
ADC_slices(:,:,z) = ADC;
end
show_img(imrotate(imresize(abs(ADC_slices(:,:,11)),[256,256]),90));

%% Saving Degraded (via MP Recon Pipeline) Dicom Images
% 1. Read
% 1. Image must be cast to a uint16 and normalized to [0,32767]
% 2. Change series description, number, and instance number
% 3. Study/Exam should not change
input_folder_reference_original =
'/biotic/home/allyk/data/DICOMS/Originals/TD05T_MUSE_007 TD05T_MUSE_007
TD05T_MUSE_007/NSHA MUSE CHOLESTEATOMA 8CH/MR 8CH Ax DWi 3sh 8ave 2mm iso/';
output_folder_MUSE = '/biotic/home/allyk/data/DICOMS/MUSE_Reconstructed/';
original_dicom_dir = dir([input_folder_reference_original, 'MR*']);
nslices_reference = numel(original_dicom_dir);
header_reference = dicominfo([original_dicom_dir(1).folder '/'
original_dicom_dir(1).name]);
all_dicom_headers_reference(nslices_reference) = header_reference;

newSeriesNumberMUSERecon = header_reference.SeriesNumber*200;
newSeriesDescDegRecon = [header_reference.SeriesDescription, '_MUSE'];
newWindowWidth = 15302;
newWindowCenter = 8025;
newSeriesUID = dicomuid;
oldStudyUID = all_dicom_headers_reference(end).StudyInstanceUID;
save_path_MUSE = [output_folder_MUSE, 'MUSE_DICOM_',
num2str(newSeriesNumberMUSERecon), '/'];
mkdir(save_path_MUSE);
%double_MUSE = cat(5,MUSE_all,MUSE_all);
%MUSE_a = squeeze(sum(MUSE_all,4));
%MUSE_sl = squeeze(sum(MUSE_a,3));
%double_MUSE = ADC_slices; % cat(3,ADC_slices,MUSE_sl);
double_MUSE = squeeze(sum(MUSE_all(:,:, [2:4],:),3));
for sl= 1:28 %1:nslices_reference
    %MUSE_data = squeeze(sum(double_MUSE(:,:,:,sl),4));
    %MUSE_data = imresize(squeeze(abs(sum(MUSE_data,3))),[256,256]);
    MUSE_data = imresize(squeeze(abs(double_MUSE(:,:,sl))),[256,256]);
    %MUSE_data = medfilt2(MUSE_data,[3 2]);
    %MUSE_data = imresize(squeeze(abs(ADC_slices(:,:,sl))),[256,256]);
    norm_MUSE_data = MUSE_data.*(32768./max(MUSE_data,[],[1 2]));
    int_MUSE = cast(norm_MUSE_data, 'uint16');
    header_reference = dicominfo([original_dicom_dir(1).folder '/'
original_dicom_dir(sl).name]);
    all_dicom_headers_reference(sl) = header_reference;
    all_dicom_headers_reference(sl).WindowWidth = newWindowWidth;
    all_dicom_headers_reference(sl).WindowCenter = newWindowCenter;
    all_dicom_headers_reference(sl).SeriesDescription = newSeriesDescDegRecon;
    all_dicom_headers_reference(sl).SeriesNumber = newSeriesNumberMUSERecon;
    all_dicom_headers_reference(sl).SeriesInstanceUID = newSeriesUID;
    all_dicom_headers_reference(sl).StudyInstanceUID = oldStudyUID;
    all_dicom_headers_reference(sl).InstanceNumber = sl;
end

```



```

        dicomwrite(int_MUSE(:, :), [save_path_MUSE, '/MUSE_dicom_sl',
num2str(s1), '.dcm'], all_dicom_headers_reference(s1));
    end
    %% GNR & SNR
    for z = 1:Nz
    %for num_a = 1:Na
    for num_Nd = 1:Nd
    MUSE_avg = squeeze(MUSE_all(:, :, num_Nd, z));
    %MUSE_avg = squeeze(MUSE_all(:, :, num_Nd, z));
    ghost_roi = abs(MUSE_avg(75:85, 5:15));
    noise_roi = abs(MUSE_avg(118:128, 5:15));
    brain_roi = abs(MUSE_avg(75:85, 68:78));
    % GNR(num_Nd, num_a, z) = mean(ghost_roi(:))./std(noise_roi(:));
    % SNR(num_Nd, num_a, z) = mean(brain_roi(:))./std(noise_roi(:));
    GNR(num_Nd, z) = mean(ghost_roi(:))./std(noise_roi(:));
    SNR(num_Nd, z) = mean(brain_roi(:))./std(noise_roi(:));
    % GNR(avg_keep) = mean(ghost_roi(:))./std(noise_roi(:));
    % SNR(avg_keep) = mean(brain_roi(:))./std(noise_roi(:));

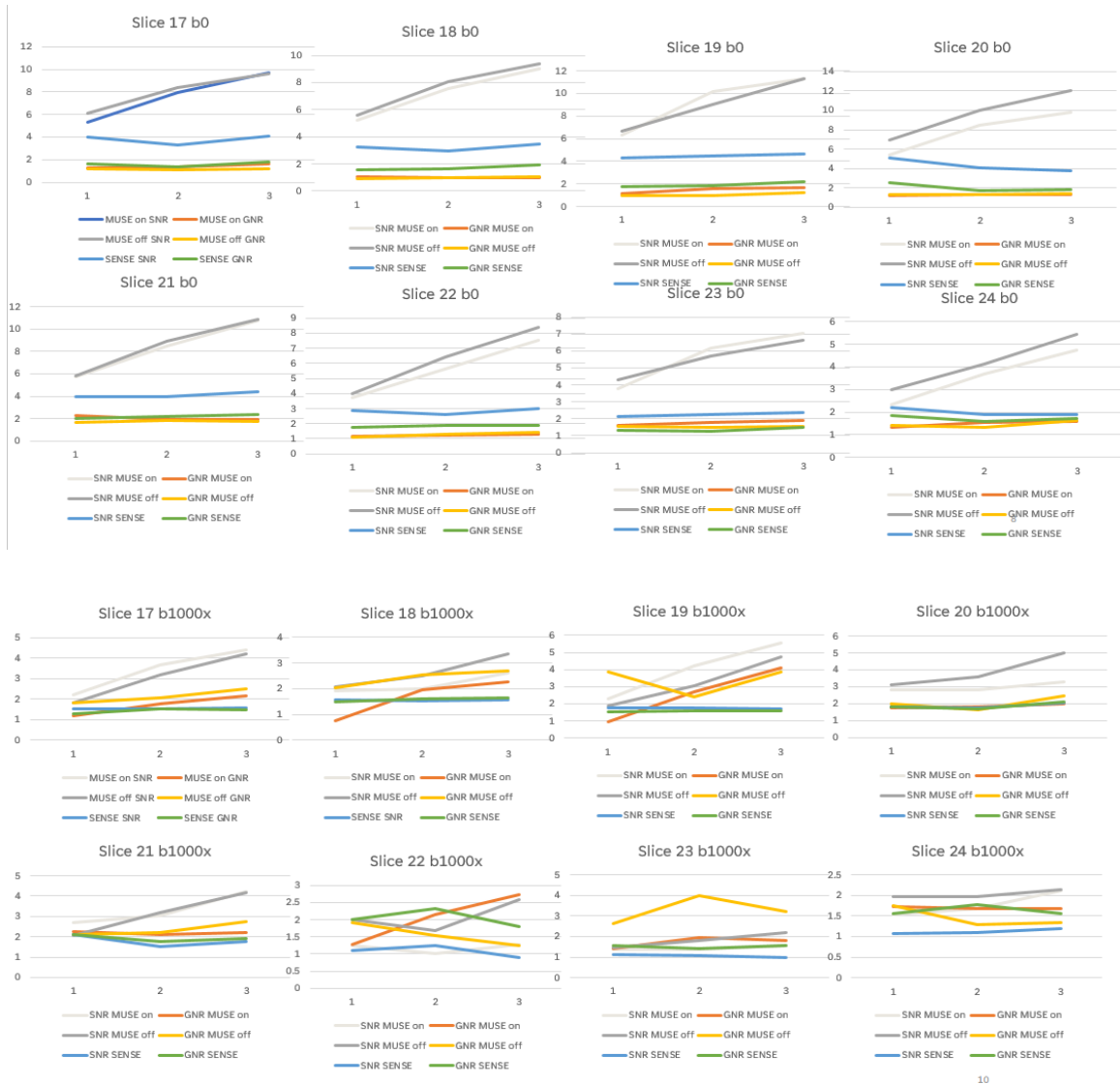
    %figure; imagesc(abs(MUSE_avg(:, :)))
    end
    end
    %end
    %%
    final_MUSE = zeros(Nx, Ny, Nz);
    for Z = 1:Nz
        collapsed_data = squeeze(sum(MUSE_all(:, :, [2 4], Z), 3));
        %   bilinear(:, :, Z) = imresize(collapsed_data, [256 256], 'bilinear');
        %   triangle(:, :, Z) = imresize(collapsed_data, [256 256], 'triangle');
        lpad = 2*size(collapsed_data);
        MUSE_kspace = fft2c(collapsed_data, lpad);
        filter = fft2c(fspecial('gaussian', size(MUSE_kspace)));
        filtered_MUSE = MUSE_kspace.*filter;
        zero_pad_MUSE = padarray(filtered_MUSE, [256 256], 0);
        final_MUSE(:, :, Z) = zero_pad_MUSE;

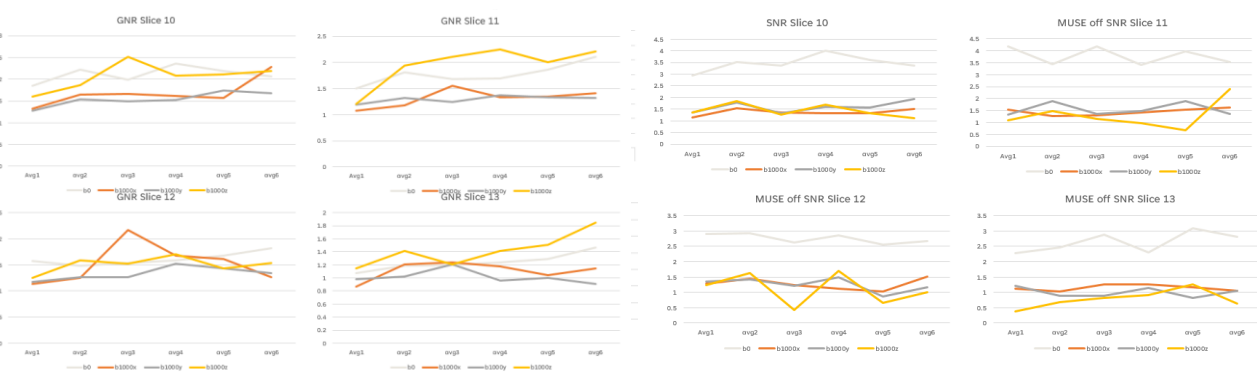
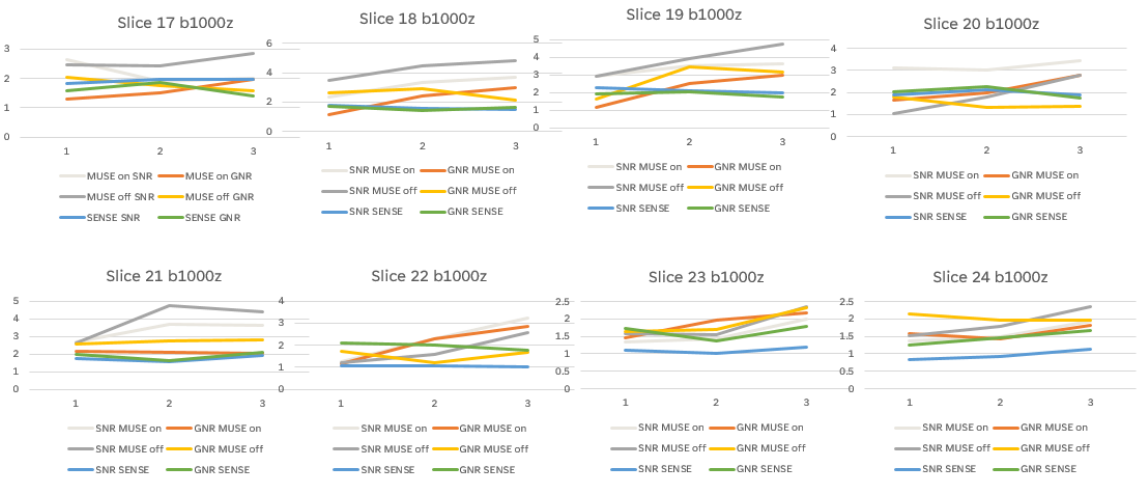
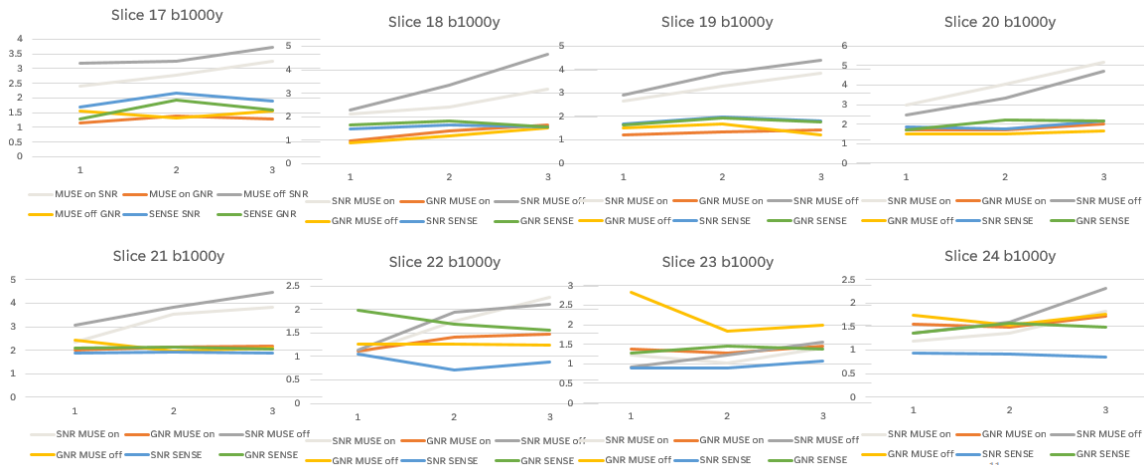
    end
    % show_grid(abs(bilinear(:, :, [18:24])));title('Bilinear');
    % show_grid(abs(triangle(:, :, [18:24])));title('Triangle');

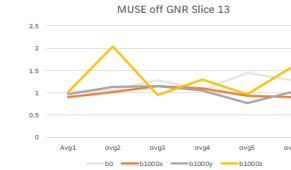
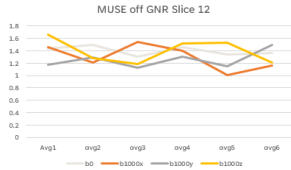
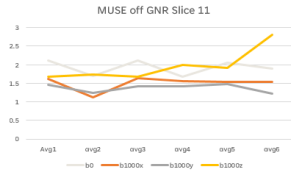
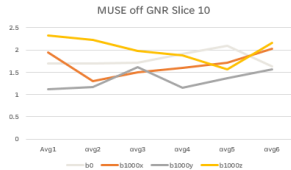
```

## Appendix IV: Trends in combined averages

An investigation into the effects of combining average was run across multiple slices with and without MUSE, as well as across diffusion directions. Each graph shows increasing number of averages. No conclusive trend was found and the differences in averages was determined to be an issue in the partial reconstruction pipeline.

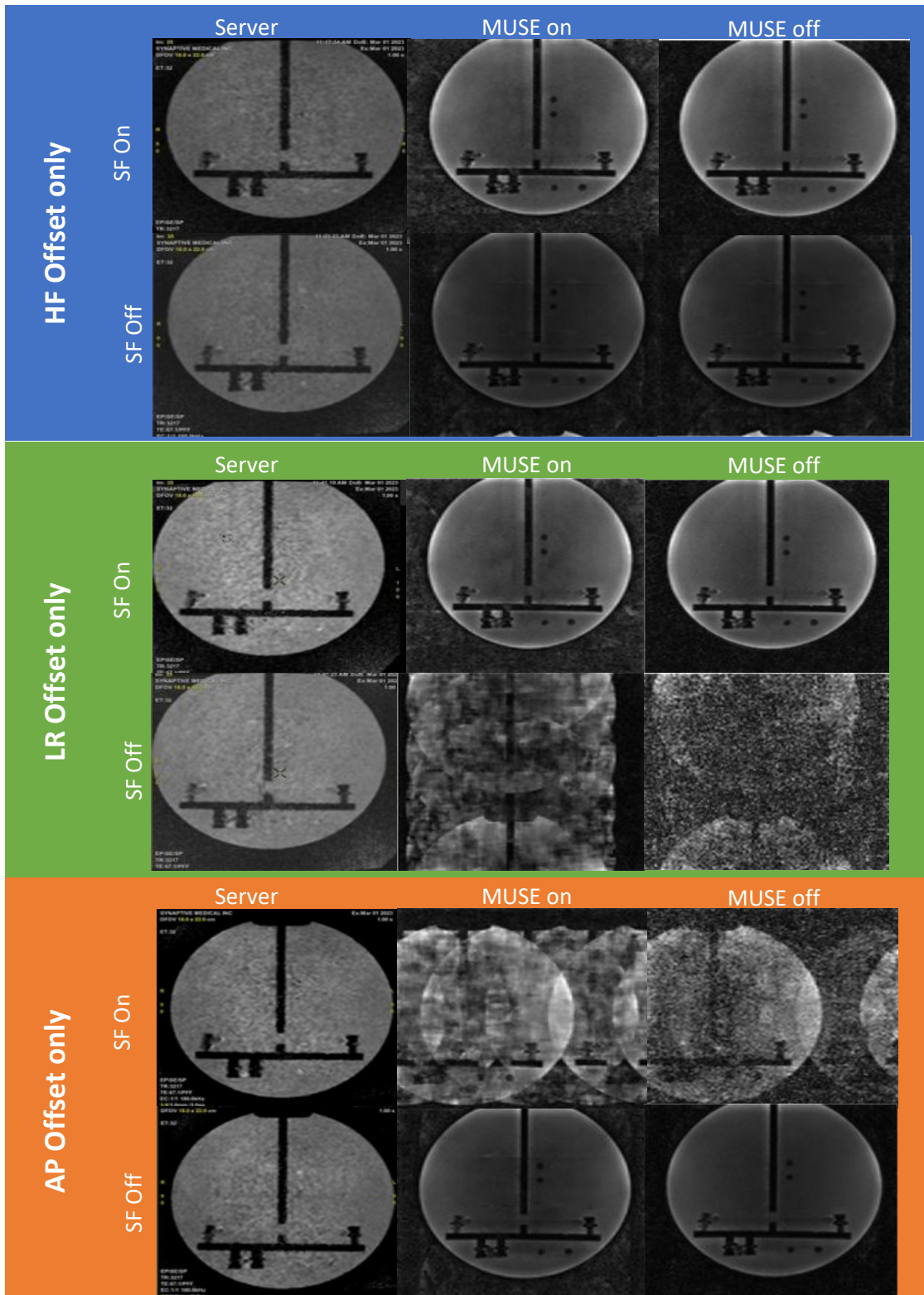






## Appendix V. Switch Frequency Troubleshooting

Manual entry of anatomical position shifts caused a degradation in the breadcrumbs when the frequency encode was switched the anterior-posterior (Figure V). The issue was only present when a shift was added in the frequency encode direction. This had not been issue previously, since shifts were typically only needed in the HF and AP directions, and not in the LR direction. The first consideration was whether this was a multi-shot issue, or whether it was present in single shot EPI as well. To address this, a 1 shot/slice/avg was obtained on the diffusion phantom with SFon and AP shift of 15 mm. This resulted in N/2 ghost, despite it being a 1-shot acquisition. With SFon and no AP shift, there was no ghosting. Increasing number of averages with AP shift resulted in some sort of striation artifact as well as N/2 ghost. Increasing number of shots to 4 made it difficult to differentiate between N/4 ghosting and AP shift ghost. SOff with AP shift was identical to SFon with 0 AP shift. All of this supported the issue being related to how the offline reconstruction pipeline was handling shifts in the frequency encode direction, regardless of number of shots or averages.



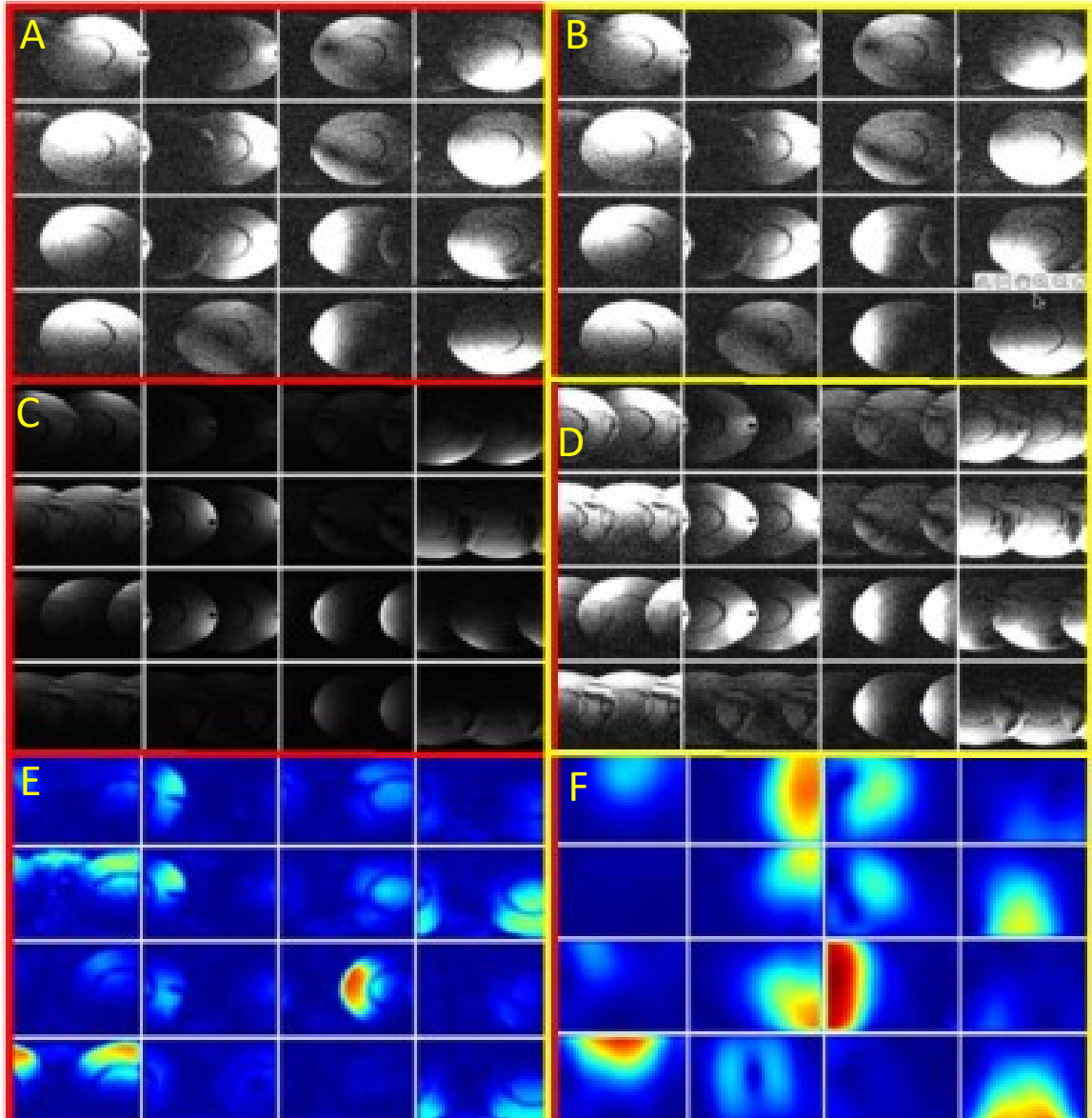
**Figure V.** Investigating the relationship between frequency encode direction switching and offsets. For each trial, an offset was applied in a single direction. Server images are standard diffusion and MUSE on/off are  $b=0$ , since some diffusion images had insufficient signal. Top: Head-foot (HF) offset applied. Images are relatively consistent across reconstruction method. Middle: Left-right (LR) offset. Offline reconed images with SFoff were blurred and excessively ghosted. Bottom: Anterior-posterior (AP) offset. Offline reconed images with SFon were blurred and excessively ghosted. SFoff: switch frequency off. SFon: switch frequency on. Server = data analysis server used by physicians.

## Appendix VI. FOV Shift Troubleshooting

The first version of the offline reconstruction pipeline produced breadcrumbs at an advanced position along the reconstruction process where the shots, averages, and diffusion directions were already combined. Since it was necessary to have the shots separated to perform MUSE, a Version 2 was developed that produced individual hybrid images for each shot. Version 3 produced a reconstruction log that explicitly identified the parameters being used during the recon. This was in an attempt to address whether the modifier files were being read and incorporated into the reconstruction process. At this point, a noticeable FOV shift between what was coming into Matlab compared to what was reconstructing online with the vendor reconstruction was observed (Figure 3.5). This stage of development was using the third version of the reconstruction pipeline in the docker. Investigating the source of the error began with comparing images in Matlab reconstructed with the data-derived sensitivities and the offline reconstruction pipeline coil coefficients. First looking at images directly after SENSE reconstruction, there were no visible differences regardless of sensitivities used (Figure 3.6 A & B).

Next was to look at whether SENSE could properly estimate full-FOV images from under-sampled data using the sensitivities. To do this, the data was retrospectively under-sampled by skipping every second datapoint in the x-dimension. When reconstructed with SENSE, both the derived sensitivities and coil coefficients left aliasing, suggesting sensitivity estimates were not accurate (Figure 3.6 C & D). Next, the magnitude of the sensitivities were compared (Figure 3.6 E & F). There was a clear shift

in the derived sensitivities compared to the coil coefficients, suggesting that there was specifically a shift happening in the hybrid images, since the same shift was not present in the coil coefficients. This inconsistency was brought to the Synaptive engineers, and was discovered to be an issue with the navigator, specifically that old code was running with a new reconstruction pipeline. Over-riding this with a text file addressed the issue.



**Figure VI.1.** Investigating Matlab pipeline as the source of FOV shift. Left column: Images reconstructed with derived sensitivities. Right column: Images reconstructed with coil combination coefficients. A & B: Fully sampled data directly after SENSE recon. There is no visible difference regardless of sensitivities used. C & D: Artificially under-sampled data by skipping every second datapoint in the x-dimension in a 1-shot dataset reconstructed with SENSE. Both the derived sensitivities and coil coefficients left aliasing after SENSE, suggesting sensitivity estimates were not accurate. E & F: Comparison of sensitivity magnitudes. Derived sensitivities are clearly shifted compared to coil coefficients.



## Appendix VII. Acquisition Parameters

Acquisition parameters were varied across the first four healthy volunteers (Table VII.1).

The final, consistent protocol was used to scan the three patients and two healthy control volunteers (Table VII.2).

**Table VII.1.** Acquisition parameters for the first four healthy volunteers scanned with ms-DW-EPI at 0.5 T. The number of shots, averages, special features such as switch frequency (SF) off or on or intentional movement, TE, TR, matrix size, FOV, and slice spacing and thickness are reported. Unless otherwise stated, DW gradients are applied.

#shots	#avgs	Features	TE (msec)	TR (msec)	Matrix	FOV (cm <sup>2</sup> )	SI th/sp (mm)
<b>TD05T_MUSE_001</b>							
1	1	SFoff	140	6444	128x128	24	5.5/6.5
1	6	SFoff	140	6444	128x128	24	5.5/6.5
1	1	SFon	88.5	4191	128x128	24	5.5/6.5
1	6	SFon	88.5	4191	128x128	24	5.5/6.5
2	1	SFoff	88.7	4195	128x128	24	5.5/6.5
2	6	SFoff	88.7	4196	128x128	24	5.5/6.5
1	1	SFoff ,No DWI	67.1	2731	128x128	24	5/10
<b>TD05T_MUSE_002</b>							
1	6	SFoff	140	6444	128x128	24	5.5/6.5
1	6	SFon	88.5	4191	128x128	24	5.5/6.5
2	6	SFoff	88.7	4195	128x128	24	5.5/6.5
4	3	SFoff	65.2	3140	128x128	24	5.5/6.5
2	6	SFoff ,MOVE	88.7	4195	128x128	24	5.5/6.5

TD05T_MUSE_003							
4	6	SFoff	65.4	3144	128x128	24	5.5/6.5
4	6	SFoff	67.1	3218	128x128	18	3/3
4	6	SFon	67.1	3218	128x128	18	3/3
TD05T_MUSE_004							
4	6	SFoff	65.4	3144	128x128	24	5.5/6.5
4	1	SFoff	65.5	3000	128x128	24	5.5/5.5
4	6	SFon	66.3	3194	128x128	18	5.5/5.5
4	6	SFon	66	3177	128x128	20	5/5
4	6	SFon	65.8	3163	128x128	22	4.5/4.5

*Table VII.2. Acquisition parameters for three patients and two healthy volunteers recruited for scanning with ms-DW-EPI at 0.5 T. MUSE\_005 differs from MUSE\_006-009.*

	TE (msec)	TR (msec)	Matrix	FOV (cm <sup>2</sup> )	BW (kHz)	SI th/sp
TD05T_MUSE_005						
<b>1shotPI2</b>	71.2	3396	96x96	18	180	3/3
<b>2shot</b>	71.2	3396	96x96	18	180	3/3
<b>3shot</b>	62.3	2985	96x96	18	180	3/3
TD05T_MUSE_006						
<b>1shotPI2</b>	64.5	3035	88x88	17.6	180	2/2
<b>2shot</b>	64.5	3044	88x88	17.6	180	2/2
<b>3shot</b>	59.5	2813	96x96	19.2	180	2/2


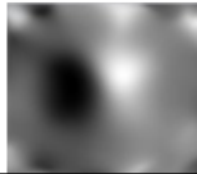

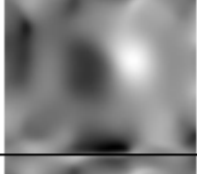


<b>TD05T_MUSE_007</b>						
<b>1shotPI2</b>	64.5	3035	88x88	17.6	180	2/2
<b>2shot</b>	64.5	3044	88x88	17.6	180	2/2
<b>3shot</b>	59.4	2809	96x96	19.2	180	2/2
<b>3shotTE90</b>	90	3666	96x96	19.2	180	2/2
<b>TD05T_MUSE_008</b>						
<b>1shotPI2</b>	64.5	3035	88x88	17.6	180	2/2
<b>2shot</b>	64.5	3044	88x88	17.6	180	2/2
<b>3shot</b>	59.4	2809	96x96	19.2	180	2/2
<b>TD05T_MUSE_009</b>						
<b>1shotPI2</b>	64.7	3040	88x88	17.6	180	2/2
<b>2shot</b>	64.5	3044	88x88	17.6	180	2/2
<b>3shot</b>	59.4	2809	96x96	19.2	180	2/2

## Appendix VIII: Characterizing Coil Coefficients

Coil coefficients were characterized by varying the acquisition parameters one at a time

(Table VIII.1)

Table VIII.1. Characterizing coil coefficient behaviour after parameter adjustments. Parameters were adjusted one after another. The parameter that was adjusted between each scan is bolded. SF = Switch frequency, AP = Anterior-posterior.

Protocol order	# shots	SF on/off	AP shift	FOV	Move/no move	Channel Coefficients
1	1	On	20	24	No move	
2	1	<b>Off</b>	20	24	No move	
3	1	Off	<b>0</b>	24	No move	
4	1	Off	0	<b>30</b>	No move	
5	<b>2</b>	Off	0	30	No move	
6	2	Off	0	30	<b>Move</b>	
7	2	Off	0	30	<b>Move</b>	